

Advances in Civil Engineering

Advancements in the Analysis and Design of Protective Structures against Extreme Loadings 2021

Lead Guest Editor: Li Chen

Guest Editors: Xihong Zhang, Yanchao Shi, Chiara Bedon, Piotr Sielicki, and Weifang Xiao





**Advancements in the Analysis and Design of
Protective Structures against Extreme Loadings
2021**

Advances in Civil Engineering

**Advancements in the Analysis and
Design of Protective Structures against
Extreme Loadings 2021**

Lead Guest Editor: Li Chen

Guest Editors: Xihong Zhang, Yanchao Shi, Chiara
Bedon, Piotr Sielicki, and Weifang Xiao



Copyright © 2022 Hindawi Limited. All rights reserved.

This is a special issue published in "Advances in Civil Engineering." All articles are open access articles distributed under the Creative Commons Attribution License, which permits unrestricted use, distribution, and reproduction in any medium, provided the original work is properly cited.






Chief Editor

Cumaraswamy Vipulanandan, USA













Associate Editors

Chiara Bedon , Italy
Constantin Chalioris , Greece
Ghassan Chehab , Lebanon
Ottavia Corbi, Italy
Mohamed ElGawady , USA
Husnain Haider , Saudi Arabia
Jian Ji , China
Jiang Jin , China
Shazim A. Memon , Kazakhstan
Hossein Moayedi , Vietnam
Sanjay Nimbalkar, Australia
Giuseppe Oliveto , Italy
Alessandro Palmeri , United Kingdom
Arnaud Perrot , France
Hugo Rodrigues , Portugal
Victor Yepes , Spain
Xianbo Zhao , Australia

Academic Editors

José A.F.O. Correia, Portugal
Glenda Abate, Italy
Khalid Abdel-Rahman , Germany
Ali Mardani Aghabaglou, Turkey
José Aguiar , Portugal
Afaq Ahmad , Pakistan
Muhammad Riaz Ahmad , Hong Kong
Hashim M.N. Al-Madani , Bahrain
Luigi Aldieri , Italy
Angelo Aloisio , Italy
Maria Cruz Alonso, Spain
Filipe Amarante dos Santos , Portugal
Serji N. Amirkhania, USA
Eleftherios K. Anastasiou , Greece
Panagiotis Ch. Anastasopoulos , USA
Mohamed Moafak Arbili , Iraq
Farhad Aslani , Australia
Siva Avudaiappan , Chile
Ozgur BASKAN , Turkey
Adewumi Babafemi, Nigeria
Morteza Bagherpour, Turkey
Qingsheng Bai , Germany
Nicola Baldo , Italy
Daniele Baraldi , Italy

Eva Barreira , Portugal
Emilio Bastidas-Arteaga , France
Rita Bento, Portugal
Rafael Bergillos , Spain
Han-bing Bian , China
Xia Bian , China
Huseyin Bilgin , Albania
Giovanni Biondi , Italy
Hugo C. Biscaia , Portugal
Rahul Biswas , India
Edén Bojórquez , Mexico
Giosuè Boscato , Italy
Melina Bosco , Italy
Jorge Branco , Portugal
Bruno Briseghella , China
Brian M. Broderick, Ireland
Emanuele Brunesi , Italy
Quoc-Bao Bui , Vietnam
Tan-Trung Bui , France
Nicola Buratti, Italy
Gaochuang Cai, France
Gladis Camarini , Brazil
Alberto Campisano , Italy
Qi Cao, China
Qixin Cao, China
Iacopo Carnacina , Italy
Alessio Cascardi, Italy
Paolo Castaldo , Italy
Nicola Cavalagli , Italy
Liborio Cavaleri , Italy
Anush Chandrappa , United Kingdom
Wen-Shao Chang , United Kingdom
Muhammad Tariq Amin Chaudhary, Kuwait
Po-Han Chen , Taiwan
Qian Chen , China
Wei Tong Chen , Taiwan
Qixiu Cheng, Hong Kong
Zhanbo Cheng, United Kingdom
Nicholas Chileshe, Australia
Prinya Chindaprasirt , Thailand
Corrado Chisari , United Kingdom
Se Jin Choi , Republic of Korea
Heap-Yih Chong , Australia
S.H. Chu , USA
Ting-Xiang Chu , China


Zhaofei Chu , China
Wonseok Chung , Republic of Korea
Donato Ciampa , Italy
Gian Paolo Cimellaro, Italy
Francesco Colangelo, Italy
Romulus Costache , Romania
Liviu-Adrian Cotfas , Romania
Antonio Maria D'Altri, Italy
Bruno Dal Lago , Italy
Amos Darko , Hong Kong
Arka Jyoti Das , India
Dario De Domenico , Italy
Gianmarco De Felice , Italy
Stefano De Miranda , Italy
Maria T. De Risi , Italy
Tayfun Dede, Turkey
Sadik O. Degertekin , Turkey
Camelia Delcea , Romania
Cristoforo Demartino, China
Giuseppe Di Filippo , Italy
Luigi Di Sarno, Italy
Fabio Di Trapani , Italy
Aboelkasim Diab , Egypt
Thi My Dung Do, Vietnam
Giulio Dondi , Italy
Jiangfeng Dong , China
Chao Dou , China
Mario D'Aniello , Italy
Jingtao Du , China
Ahmed Elghazouli, United Kingdom
Francesco Fabbrocino , Italy
Flora Faleschini , Italy
Dingqiang Fan, Hong Kong
Xueping Fan, China
Qian Fang , China
Salar Farahmand-Tabar , Iran
Ilenia Farina, Italy
Roberto Fedele, Italy
Guang-Liang Feng , China
Luigi Fenu , Italy
Tiago Ferreira , Portugal
Marco Filippo Ferrotto, Italy
Antonio Formisano , Italy
Guoyang Fu, Australia
Stefano Galassi , Italy

Junfeng Gao , China
Meng Gao , China
Giovanni Garcea , Italy
Enrique García-Macías, Spain
Emilio García-Taengua , United Kingdom
DongDong Ge , USA
Khaled Ghaedi, Malaysia
Khaled Ghaedi , Malaysia
Gian Felice Giaccu, Italy
Agathoklis Giaralis , United Kingdom
Ravindran Gobinath, India
Rodrigo Gonçalves, Portugal
Peilin Gong , China
Belén González-Fonteboa , Spain
Salvatore Grasso , Italy
Fan Gu, USA
Erhan Güneyisi , Turkey
Esra Mete Güneyisi, Turkey
Pingye Guo , China
Ankit Gupta , India
Federico Gusella , Italy
Kemal Hacıfendioglu, Turkey
Jianyong Han , China
Song Han , China
Asad Hanif , Macau
Hadi Hasanzadehshooiili , Canada
Mostafa Fahmi Hassanein, Egypt
Amir Ahmad Hedayat , Iran
Khandaker Hossain , Canada
Zahid Hossain , USA
Chao Hou, China
Biao Hu, China
Jiang Hu , China
Xiaodong Hu, China
Lei Huang , China
Cun Hui , China
Bon-Gang Hwang, Singapore
Jijo James , India
Abbas Fadhil Jasim , Iraq
Ahad Javanmardi , China
Krishnan Prabhakan Jaya, India
Dong-Sheng Jeng , Australia
Han-Yong Jeon, Republic of Korea
Pengjiao Jia, China
Shaohua Jiang , China

MOUSTAFA KASSEM , Malaysia
Mosbeh Kaloop , Egypt
Shankar Karuppannan , Ethiopia
John Kechagias , Greece
Mohammad Khajehzadeh , Iran
Afzal Husain Khan , Saudi Arabia
Mehran Khan , Hong Kong
Manoj Khandelwal, Australia
Jin Kook Kim , Republic of Korea
Woosuk Kim , Republic of Korea
Vaclav Koci , Czech Republic
Loke Kok Foong, Vietnam
Hailing Kong , China
Leonidas Alexandros Kouris , Greece
Kyriakos Kourousis , Ireland
Moacir Kripka , Brazil
Anupam Kumar, The Netherlands
Emma La Malfa Ribolla, Czech Republic
Ali Lakirouhani , Iran
Angus C. C. Lam, China
Thanh Quang Khai Lam , Vietnam
Luciano Lamberti, Italy
Andreas Lampropoulos , United Kingdom
Raffaele Landolfo, Italy
Massimo Latour , Italy
Bang Yeon Lee , Republic of Korea
Eul-Bum Lee , Republic of Korea
Zhen Lei , Canada
Leonardo Leonetti , Italy
Chun-Qing Li , Australia
Dongsheng Li , China
Gen Li, China
Jiale Li , China
Minghui Li, China
Qingchao Li , China
Shuang Yang Li , China
Sunwei Li , Hong Kong
Yajun Li , China
Shun Liang , China
Francesco Liguori , Italy
Jae-Han Lim , Republic of Korea
Jia-Rui Lin , China
Kun Lin , China
Shibin Lin, China

Tzu-Kang Lin , Taiwan
Yu-Cheng Lin , Taiwan
Hexu Liu, USA
Jian Lin Liu , China
Xiaoli Liu , China
Xuemei Liu , Australia
Zaobao Liu , China
Zhuang-Zhuang Liu, China
Diego Lopez-Garcia , Chile
Cristiano Loss , Canada
Lyan-Ywan Lu , Taiwan
Jin Luo , USA
Yanbin Luo , China
Jianjun Ma , China
Junwei Ma , China
Tian-Shou Ma, China
Zhongguo John Ma , USA
Maria Macchiaroli, Italy
Domenico Magisano, Italy
Reza Mahinroosta, Australia
Yann Malecot , France
Prabhat Kumar Mandal , India
John Mander, USA
Iman Mansouri, Iran
André Dias Martins, Portugal
Domagoj Matesan , Croatia
Jose Matos, Portugal
Vasant Matsagar , India
Claudio Mazzotti , Italy
Ahmed Mebarki , France
Gang Mei , China
Kasim Mermerdas, Turkey
Giovanni Minafò , Italy
Masoomah Mirrashid , Iran
Abbas Mohajerani , Australia
Fadzli Mohamed Nazri , Malaysia
Fabrizio Mollaioli , Italy
Rosario Montuori , Italy
H. Naderpour , Iran
Hassan Nasir , Pakistan
Hossein Nassiraei , Iran
Satheeskumar Navaratnam , Australia
Ignacio J. Navarro , Spain
Ashish Kumar Nayak , India
Behzad Nematollahi , Australia

Chayut Ngamkhanong , Thailand
Trung Ngo, Australia
Tengfei Nian, China
Mehdi Nikoo , Canada
Youjun Ning , China
Olugbenga Timo Oladinrin , United Kingdom
Oladimeji Benedict Olalusi, South Africa
Timothy O. Olawumi , Hong Kong
Alejandro Orfila , Spain
Maurizio Orlando , Italy
Siti Aminah Osman, Malaysia
Walid Oueslati , Tunisia
SUVASH PAUL , Bangladesh
John-Paris Pantouvakis , Greece
Fabrizio Paolacci , Italy
Giuseppina Pappalardo , Italy
Fulvio Parisi , Italy
Dimitrios G. Pavlou , Norway
Daniele Pellegrini , Italy
Gatheeshgar Perampalam , United Kingdom
Daniele Perrone , Italy
Giuseppe Piccardo , Italy
Vagelis Plevris , Qatar
Andrea Pranno , Italy
Adolfo Preciado , Mexico
Chongchong Qi , China
Yu Qian, USA
Ying Qin , China
Giuseppe Quaranta , Italy
Krishanu ROY , New Zealand
Vlastimir Radonjanin, Serbia
Carlo Rainieri , Italy
Rahul V. Ralegaonkar, India
Raizal Saifulnaz Muhammad Rashid, Malaysia
Alessandro Rasulo , Italy
Chonghong Ren , China
Qing-Xin Ren, China
Dimitris Rizos , USA
Geoffrey W. Rodgers , New Zealand
Pier Paolo Rossi, Italy
Nicola Ruggieri , Italy
JUNLONG SHANG, Singapore


Nikhil Saboo, India
Anna Saetta, Italy
Juan Sagaseta , United Kingdom
Timo Saksala, Finland
Mostafa Salari, Canada
Ginevra Salerno , Italy
Evangelos J. Sapountzakis , Greece
Vassilis Sarhosis , United Kingdom
Navaratnarajah Sathiparan , Sri Lanka
Fabrizio Scozzese , Italy
Halil Sezen , USA
Payam Shafigh , Malaysia
M. Shahria Alam, Canada
Yi Shan, China
Hussein Sharaf, Iraq
Mostafa Sharifzadeh, Australia
Sanjay Kumar Shukla, Australia
Amir Si Larbi , France
Okan Sirin , Qatar
Piotr Smarzewski , Poland
Francesca Sollecito , Italy
Rui Song , China
Tian-Yi Song, Australia
Flavio Stochino , Italy
Mayank Sukhija , USA
Piti Sukontasukkul , Thailand
Jianping Sun, Singapore
Xiao Sun , China
T. Tafsirojjaman , Australia
Fujiao Tang , China
Patrick W.C. Tang , Australia
Zhi Cheng Tang , China
Weerachart Tangchirapat , Thailand
Xiixin Tao, China
Piergiorgio Tataranni , Italy
Elisabete Teixeira , Portugal
Jorge Iván Tobón , Colombia
Jing-Zhong Tong, China
Francesco Trentadue , Italy
Antonello Troncone, Italy
Majbah Uddin , USA
Tariq Umar , United Kingdom
Muahmmad Usman, United Kingdom
Muhammad Usman , Pakistan
Mucteba Uysal , Turkey

Ilaria Venanzi , Italy
Castorina S. Vieira , Portugal
Valeria Vignali , Italy
Claudia Vitone , Italy
Liwei WEN , China
Chunfeng Wan , China
Hua-Ping Wan, China
Roman Wan-Wendner , Austria
Chaohui Wang , China
Hao Wang , USA
Shiming Wang , China
Wayne Yu Wang , United Kingdom
Wen-Da Wang, China
Xing Wang , China
Xiuling Wang , China
Zhenjun Wang , China
Xin-Jiang Wei , China
Tao Wen , China
Weiping Wen , China
Lei Weng , China
Chao Wu , United Kingdom
Jiangyu Wu, China
Wangjie Wu , China
Wenbing Wu , China
Zhixing Xiao, China
Gang Xu, China
Jian Xu , China
Panpan , China
Rongchao Xu , China
HE YONGLIANG, China
Michael Yam, Hong Kong
Hailu Yang , China
Xu-Xu Yang , China
Hui Yao , China
Xinyu Ye , China
Zhoujing Ye, China
Gürol Yildirim , Turkey
Dawei Yin , China
Doo-Yeol Yoo , Republic of Korea
Zhanping You , USA
Afshar A. Yousefi , Iran
Xinbao Yu , USA
Dongdong Yuan , China
Geun Y. Yun , Republic of Korea

Hyun-Do Yun , Republic of Korea
Cemal YİĞİT , Turkey
Paolo Zampieri, Italy
Giulio Zani , Italy
Mariano Angelo Zanini , Italy
Zhixiong Zeng , Hong Kong
Mustafa Zeybek, Turkey
Henglong Zhang , China
Jiupeng Zhang, China
Tingting Zhang , China
Zengping Zhang, China
Zetian Zhang , China
Zhigang Zhang , China
Zhipeng Zhao , Japan
Jun Zhao , China
Annan Zhou , Australia
Jia-wen Zhou , China
Hai-Tao Zhu , China
Peng Zhu , China
QuanJie Zhu , China
Wenjun Zhu , China
Marco Zucca, Italy
Haoran Zuo, Australia
Junqing Zuo , China
Robert Černý , Czech Republic
Süleyman İpek , Turkey







Contents

Performance Assessment of Reinforced Concrete Frame under Close-In Blast Loading

Solomon Abebe and Tesfaye Alemu Mohammed 




Research Article (24 pages), Article ID 3979195, Volume 2022 (2022)

Bending Performance of Precast Lightweight Aggregate Concrete Exterior Wallboard with a Concealed Rib Sandwich Structure

Congqi Li , Xinwei Ma , Ying Yang , Ahmed Ahmad Omar , Hao Wu , and Lei Qian 



Research Article (14 pages), Article ID 1328583, Volume 2022 (2022)

Field Tests' Study of Deviation Correction of Building near Excavation

Xi Peng , Ningxin Yang , and Mi Zhou 

Research Article (10 pages), Article ID 6287388, Volume 2021 (2021)

Numerical Study on the Behavior of Square Stiffened Caissons Penetrating into Normally Consolidated Clay

Wei Liu , Zhihuai Huang , and Mi Zhou 

Research Article (10 pages), Article ID 1607854, Volume 2021 (2021)

Optimized Design for Large Geotextile Mats over Soft Soil

Zhihuai Huang , Shuaidong Yang , Ningxin Yang, Mi Zhou , and Ang Li

Research Article (13 pages), Article ID 4084961, Volume 2021 (2021)

Research Article

Performance Assessment of Reinforced Concrete Frame under Close-In Blast Loading

Solomon Abebe¹ and Tesfaye Alemu Mohammed ²

¹Civil Engineering Department, Debre Markos University, Debre Markos, Ethiopia

²Civil Engineering Department, Addis Ababa Science and Technology University, Addis Ababa, Ethiopia

Correspondence should be addressed to Tesfaye Alemu Mohammed; tes.alemu@gmail.com

Received 22 October 2021; Revised 25 January 2022; Accepted 9 March 2022; Published 27 March 2022

Academic Editor: Weifang Xiao

Copyright © 2022 Solomon Abebe and Tesfaye Alemu Mohammed. This is an open access article distributed under the Creative Commons Attribution License, which permits unrestricted use, distribution, and reproduction in any medium, provided the original work is properly cited.

The need for assessing and retrofitting structures increased with time as terrorism-induced explosion trends rose with time. This paper presents a numerical investigation on performance assessment of a two-story, one-bay seismic resistant reinforced concrete framed building under close-in blast loading. ANSYS AUTODYN, an explicit nonlinear finite element software program, was used for 3D model development and analysis. The experimental results reported in the literature were used to validate proposed FE models. Furthermore, parametric studies on close-in explosive story-to-story locations and charge masses were performed on both conventional and seismically detailed RC framed structures. FEA results showed that a decrease in scaled distance raised effective plastic strain and damage index values. Furthermore, simultaneous use of close-spaced transverse steel reinforcement spacing in mid-height and ends of reinforced concrete columns is found to be effective in reducing both effective plastic strains and damage index values.

1. Introduction

Field blast explosion tests have been performed in a very controlled manner with the help of military supervision. In part, this testing arrangement high cost and associated risk of conducting field tests limited access for blast-related extreme loading studies. However, terrorism-related or accidental explosions have increased with time. Recently, the Beirut port explosion alone resulted in 15 billion USD in civil engineering infrastructure and property damages, with reported 7000 injuries and at least 220 deaths, according to Balsamos et al. [1].

Structures designed for conventional gravity and seismic loading are vulnerable to extensive damage when subjected to extreme blast loading. This is partly because conventional structures are designed and detailed for reduced seismic demands and have limited capacity to resist abnormally high impulsive extreme loads such as impact and blast loading [2, 3]. Previous studies focused on the investigation of individual reinforced structural members such as beams [4–6], columns [3, 7–9], and slabs [10–12] subjected to blast loading.

A few studies investigated the overall global response of reinforced concrete frames consisting of all slab, beam, and column structural members. Jayasooriya [2] performed vulnerability assessment and damage analysis of reinforced concrete-framed buildings subjected to near-field blast loading. The author implied the use of multisteel reinforcement cages and composite columns to resist blast loading. With the help of a commercially available software SAP2000, the authors in [13–15] conducted a numerical study on the behavior and response of multistory reinforced concrete buildings. Tewari and Sharma [16] studied the effect of blast load on the dynamic response of a high-story 3D RC frame by using STAAD Pro.

On the other hand, the authors in [17, 18] deployed ANSYS AUTODYN FE packaged software to evaluate the behavior and response of a plane frame structure under blast load. Williams et al. [17] determined the numerical response of a one-story, one-bay steel frame. The researchers modeled the steel plane frame by using a single degree of freedom, design to resist a given seismic load, and different blast load scenarios were deployed on the frame system by using a TNT

explosive. From the study results, the authors insisted that, during the blast loading event, the seismically designed plane frame was robust enough to enter plastic zones.

Moreover, Murali and Sujisha [18] studied the response of three-story, three-bay reinforced concrete bare frames, frames with and without brick infill walls, and brick infill walled frames with and without openings prone to blast loading. The frames were designed and detailed as ordinary moment-resisting frames, and then the 3D FEA modelling was employed by using the nonlinear computational program ANSYS AUTODYN. The authors generated the TNT explosive simulations from the AUTODYN module, and two blast-induced shock waves, namely, blast load with and without negative phase profiles, were considered. From the numerical study results, frames subjected to both positive and negative phases revealed maximum displacement values. In addition to this, infill walled frames with openings were found to be susceptible to large displacements.

On the other hand, Toy and Sevim [19] numerically investigated the structural response of a two-story, two-bay reinforced concrete building prone to blast load. The authors designed and detailed only one building model, especially an existing real building that bombed in August 2015 in Istanbul, and only one analysis was performed. Explicit analysis was employed by using the nonlinear FEA computational software ANSYS AUTODYN. Based on the FEA postprocessed results, the authors insisted on the complete collapse of nonstructural components. However, the structural elements of the frame suffered enormous damage including crushing of concrete and yielding of reinforcement bars.

Despite the efforts made by other researchers, it is obvious that the use of commercially available general FE software such as SAP2000 and STAAD Pro may not adequately represent different material models specifically generated for abnormal loads, such as blast load, and those software also hinder researchers and engineers to use and provide explicitly different reinforcement detailing schemes, which are in contrary easy on other research FEA software such as ANSYS AUTODYN. Consequently, some researchers have also made efforts by only considering the dynamic response of a plane frame system under blast loads. But this type of analysis method mismatches and does not capture the real dynamic behavior of spatial 3D models.

Thus, there is a void in the literature to study the global overall response of a reinforced concrete frame consisting of various interconnected structural members under extreme blast loading. Moreover, due to the complicated nature of explosions and the propagation of blast-induced shock waves, it is worthy to capture load transfer mechanisms among structural members and the global response of an RC frame under blast loading by 3D modelling and analyzing of the RC frame. Also, the boundary conditions deployed for individual RC slabs, beams, and columns are all simplified and prescribed support conditions. However, 3D modelling of frames consisting of individual structural members as an interconnected framework offers options to evaluate structural joint performance in FE analysis. Currently, advances in finite element analysis and the availability of high-

speed computing have enabled spatial 3D model development of reinforced concrete frames subjected to blast loading simulation analysis.

Therefore, this study fills a perceived void in the literature by studying the structural response of two-story, one-bay, reinforced concrete frames with and without seismic detail provisions, under extreme close-in blast loading. Variable axial loads induced by dynamic reactions of beams and slabs caused by the effects of indoor explosions on supported masses are all captured. Field test data reported in literature [20] were used for validation finite element analysis, and further parametric studies on story-to-story close-in explosive locations, charge masses, and various reinforcement detailing schemes were performed on both conventional and seismically detailed RC framed structures.

2. Description of Numerical Model

ANSYS AUTODYN [21] software program was used for 3D model development, blast loading, and finite element simulation analysis. Next, details of employed material models, boundary conditions, blast loading application, and FE procedures are presented.

2.1. Material Models. The RHT material model which was originally developed by Riedel–Heirmaier–Thoma was implemented in the nonlinear computational program ANSYS AUTODYN [21] and is extensively used in finite element analysis of reinforced concrete structures under blast loading. Experimental and field blast tests were used by various authors to verify and validate their accuracy [22–25]. The authors insisted that the RHT material model united strain rate effect, equation of state (EOS), plasticity, and three failure surface caps, namely, inelastic yield, postfailure, and residual surface features to simulate concrete dynamic strength behavior for extreme loading, such as impact and blast loads. The model uses about 30 input parameters including hydrostatic compression, uniaxial tension, and uniaxial and triaxial compression parameters.

EOS describes the hydrodynamic response of a concrete material when subjected to accidental loads such as blast loading, which is assumed as hydrodynamic, with pressure varying as a function of density and internal energy [25].

In the present study, the RHT concrete material model was used to characterize concrete. Input parameters for the RHT concrete material model are presented in Tables 1–4 in terms of P-alpha, polynomial equation of states, concrete strength, and damage (failure) values.

According to [22–25], material damage is initiated, if further plastic damage occurs after the initial failure surface is reached. The model evaluates damage parameter D using equation (1). The logic behind the damage formulae is the accumulation of increments of effective plastic strain.

$$0 \leq D = \sum \frac{\Delta \varepsilon_{pl}}{\varepsilon_f(p)} \leq 1, \quad (1)$$

where $\varepsilon_f(p)$ is the failure strain and can be calculated as listed in

TABLE 1: P-alpha EOS input parameters for C-35 concrete.

Variable	Meaning	Value/remark
$\rho_{\text{solid},o}$	Reference density (kg/m ³)	2750
ρ_{porous}	Porous density (kg/m ³)	2314
c_e	Porous sound-speed (m/s)	2.92E + 3
p_{el}	Initial compaction pressure (kPa)	2.33E + 4
p_S	Solid compaction pressure (kPa)	6.00E + 6
n	Compaction exponent	3.0
T_{ref}	Reference temperature (°C)	26.85

TABLE 2: Polynomial EOS input parameters for C-35 concrete.

Variable	Meaning	Value/remark
A_1	Bulk modulus matrix (kPa)	3.53E + 7
A_2	Parameter A_2 (kPa)	3.96E + 7
A_3	Parameter A_3 (kPa)	9.04E + 6
B_0	Parameter B_0	1.22
B_1	Parameter B_1	1.22
T_1	Parameter T_1 (kPa)	3.53E + 7
T_2	Parameter T_2 (kPa)	0.00

TABLE 3: RHT concrete strength model parameters for C-35 concrete.

Variable	Meaning	Value/remark
G	Shear modulus (GPa)	16.7
f_c	Compressive strength (MPa)	35.0
CAP	Use CAP on elastic surface?	Yes
f_t/f_c	Tensile strength	0.10
f_s/f_c	Shear strength	0.18
A_{fail}	Intact failure surface constant	1.60
n_{fail}	Intact failure surface constant	0.60
$Q_{2,0}$	Tension/compression meridian ratio	0.6805
BQ	Brittle to ductile transition	0.0105
S	Hardening slope	2.00
Tensrat	Elastic strength/ f_t	0.7
Comprat	Elastic strength/ f_c	0.53
B_{frac}	Fracture strength constant	1.6
n_{frac}	Fracture strength exponent	0.61
α	Compressive strain rate exponent	0.032
δ	Tensile strain rate exponent	0.036

TABLE 4: RHT failure model input parameters for C-35 concrete.

Variable	Meaning	Value/remark
SFMAX	Maximum fracture strength ratio	1E + 20
D_1	Damage constant	0.04
D_2	Damage constant	1.00
$\varepsilon_{f,\text{min}}$	Minimum strain failure	0.01
G_{res}	Residual shear modulus fraction	0.13
EROSION	Use EROSION	Yes

$$\varepsilon_f(p) = D_1(p^f - p_t^*)^{D_2} \geq \varepsilon_{\text{min}}, \quad (2)$$

where D_1 , D_2 , p_t^* , and $\varepsilon_{f,\text{min}}$ are input parameters [22–25] and also see Table 4 for RHT material model failure input parameters.

Activating the EROSION option enables the computational engine of AUTODYN to cross check strain limits of elements and eliminate an element in a finite element model if predefined strain limits were exceeded.

Ekstrom [26] investigated concrete structure dynamic response damage and fracture energy characteristics due to blast-induced shock waves. The author showed tensile fracture energy influenced the accuracy of FEA results than strain rate material properties. Table 5 presents input parameters for the Johnson–Cook strength model, which was used for steel rebar material characterization. Similarly, Table 6 exhibits the JWL input parameters for equivalent

TNT explosives. The JWL EOS input parameters were validated using different field test cases, computational programs, and explosion field events using entropy-based thermodynamic equations [27–30].

Blast-induced shock waves cannot propagate through vacuum. Atmospheric air was modeled to characterize blast-induced shock wave propagation through the air medium. Table 7 presents the required parameter inputs for modelling atmospheric air parameters in current numerical models.

Tables 1–7 detail input parameters listing and also provide an illustrative example for fellow researchers using RHT, Johnson–Cook, and JWL material models to characterize concrete, steel rebar, ANFO, and TNT explosive materials, and air for atmospheric pressure, respectively.

2.2. Element Types. A Lagrangian solid element was used to model the concrete column and substructure. Substructure or base material was modeled for purpose of reflecting blast-induced shock waves. The strength along the compressive meridian is expressed as a triaxial compression normalized to the unconfined compression strength f_c in the AUTODYN solver in the following equation by Brannon and Leelavanichkul [22]:

$$Y_{TXC}^* = \frac{Y_{TXC}}{f_c} = a_1 \left[\frac{P}{f_c} - \frac{P_{spall}}{f_c} r_f \right]^{a_2}, \quad (3)$$

where $r_f = \begin{cases} (\epsilon'/\epsilon'_0)^\alpha: p > f_c \text{ with } \epsilon'_0 = 30 \times 10^{-6} \text{ s}^{-1} \\ (\epsilon'/\epsilon'_0)^\beta: p < f_c \text{ with } \epsilon'_0 = 3 \times 10^{-6} \text{ s}^{-1} \end{cases}$. a_1 = initial slope of failure surface, a_2 = pressure dependency of failure surface, P_{spall} = spall strength, and α and β = material constants.

The solid element supports material and geometric nonlinearity and has 8 nodes with three displacement, velocity, and acceleration DOFs per node in X , Y , and Z directions. Steel reinforcements are modeled using a two—node element resisting only tensile and compressive forces. The element is compatible with concrete solid element and has three displacement, velocity, and acceleration DOFs per node in X , Y , and Z directions.

2.3. Modelling of TNT Explosive. Pressure-volume-energy behavior of TNT explosion with different charge masses in ANSYS AUTODYN input parameters can be determined using equation (4) of Jones–Wilkins–Lee (JWL) EOS [27, 30].

$$P = A \left(1 - \frac{\omega}{R_1 V} \right) e^{-R_1 V} + B \left(1 - \frac{\omega}{R_1 V} \right) e^{-R_2 V} + \frac{\omega E}{V}, \quad (4)$$

where P is pressure and v is volume relative to undetonated state (v/v_0). The parameters A , B , R_1 , and R_2 are constants, and parameter ω is an assumed-constant material property.

While having 1 m height and different a diameter of a cylindrical TNT explosive container, the volume of the container is mapped after specifying the diameter of the cylindrical container. In other words, different charge masses of TNT are deployed by fixing the height and varying the diameter values. After establishing the required volume

of TNT explosive, the locations for detonation points are defined by specifying X , Y , and Z coordinates.

2.4. Boundary and Loading Conditions. Column bottom translation and rotational degrees of freedom are constrained. Similarly, a concrete-based substructure is also restrained from translation and rotation on each side and bottom faces. The gravitational acceleration of 9.81 m/s^2 is applied to account for self-weight of the frame elements.

2.5. Nonlinear Finite Element Analysis Computation. ANSYS AUTODYN [21] nonlinear finite element software program is used to analyze and simulate reinforced concrete frames subjected to blast loading. Automatic explicit time steps and damping controls of 0.2 and 1 value are used for linear and quadratic artificial viscosity. An AUTODYN standard is also employed to control the hourglass damping.

3. Numerical Model Validation

3.1. Description of Validated Field Test (Specimen CONV_20). The field test results reported by Siba [20] are used for validation finite element analysis. The specimen designated as CONV_20 has $300 \text{ mm} \times 300 \text{ mm}$ cross-sectional dimensions, 3200 mm height, and 41 MPa concrete compressive strength. The column is reinforced with $4\text{--}25 \text{ M}$ and has 300 mm tie spacing (Figures 1 and 2).

Siba [20] performed the blast test at 2.6 m standoff distance with 150 kg ANFO explosive material yielding a $052 \text{ m/kg}^{1/3}$ scaled distance. The experimental test column displacement values were traced by deploying displacement gauge control points. Figure 3(a) shows the field test set up of the CONV_20 RC column, whereas Figure 3(b) exhibits its corresponding FE developed model using the ANSYS AUTODYN [21] software program.

3.2. Mesh Technique and Convergence. The mesh techniques were used for the simulation of solid materials, and a well-known so-called Lagrangian mesh technique with less computational cost was used. The mesh in the Lagrange tracks the material as it deforms, and the material stays inside the original element grid. In order to control the solution accuracy, especially in case of highly distorted meshes, controlling mechanisms including hourglass control, rezoning, and remapping options were activated in the ANSYS AUTODYN computational program.

Consequently, the mesh sensitivity study is a critical step to optimize computational demands and the accuracy of finite element results. In this research, preliminary analyses were performed using different mesh sizes of 20 mm , 25 mm , 30 mm , and 40 mm (see also Figure 4) and for final analysis, a fine mesh of 20 mm with same aspect ratio is selected for all subsequent FEA.

Nodal displacement values are traced by employing a displacement control point (gauge) located at lower one-third of the column (1 m). Figure 5 exhibits the nodal displacement values for different mesh sizes (see also Table 8).

TABLE 5: Johnson–Cook strength model input parameters for S400 rebar.

Variable	Meaning	Value/remark
ρ_{ref}	Reference density (kg/m^3)	7850
E	Young's modulus (GPa)	200
ν	Poisson's ratio	0.3
K	Bulk modulus (GPa)	166
C_v	Specific heat (J/kgC)	434
SRCR	Strain rate correction	1 st order
f_y	Initial yield stress (MPa)	400
HC	Hardening constant	510
f_y	Principal tensile failure stress (MPa)	600
STCN	Strain rate constant (MPa)	0.01
TSE	Thermal softening exponent (MPa)	1.03
MT	Melting temperature ($^{\circ}\text{C}$)	1793
RSTR	Reference strain rate (sec^{-1})	1.00
Erosion	Erosion strain (%)	None
EOS	Equation of state	Linear

TABLE 6: JWL model input parameters for TNT explosive.

Variable	Meaning	Value/remark
ρ	Density (kg/m^3)	1630
A	Parameter A (GPa)	374
B	Parameter B (MPa)	375
R_1	Parameter R_1	4.15
R_2	Parameter R_2	0.90
W	Parameter W	0.35
C–J DV	C–J detonation velocity (m/s)	6930
C–J E	C–J energy/unit mass (J/kg)	$3.68E + 6$
C–J P	C–J pressure (GPa)	0.2

TABLE 7: Atmosphere air input parameters for air medium.

Variable	Meaning	Value/remark
ρ	Density (kg/m^3)	1.225
C_v	Specific heat (J/kgC)	717.6
γ	Adiabatic exponent	1.40
T_{ref}	Reference temperature ($^{\circ}\text{C}$)	26.85

3.3. *Field Test and Numerical Model Comparison.* Figures 6(a) and 6(b) present the blast wave propagation of field tests and FEA simulations during the blasting event. After the detonation of the ANFO explosive, which was contained in a cylindrical shape, the fireball engulfed the reinforced concrete column. The video recording during the experimental test carried out by Siba [20] did not show the response of the column; however, the evolution of the blast pressure and fireball was captured and a similar blast wave simulation was made by AUTODYN.

During the experimental test, Siba [20] embedded a string potentiometer at the front face of a column, and a displacement value of 11.2 mm was measured from the lower one-third region of the study column. Figure 7 elucidates a comparison of displacement-time history plots for experimentally reported data (CONV_20 RC column) and an FEA model with different mesh sizes extracted from a 1 m displacement control (gauge) point.

Moreover, posttest results for CONV_20 revealed that an extensive cracking and spalling of concrete in the lower one-

third region of the column was obtained. After activating concrete EROSION option for the damage simulation, from the postprocessed results of damage scalar values, FEA model experienced the same extent of concrete crushing at the same location, i.e. the lower part of the column (see Figure 8).

Thus, FE validation analysis results including displacement threshold values and postblast damages from ANSYS AUTODYN are in good agreement with field test data reported by Siba [20]. This affirms use of the RHT concrete constitutive model, Johnson–Cook material model for reinforcement bars, and the JWL model for simulating explosions yields acceptable values for simulation of RC structural members under blast loading. Next, a detailed finite element simulation of a full-scale two-story one-bay reinforced concrete framed structure is presented.

4. Finite Element Simulation

4.1. *RC Frame Models Reinforcement Detailing.* In this section, responses of two-story, one-bay reinforced concrete

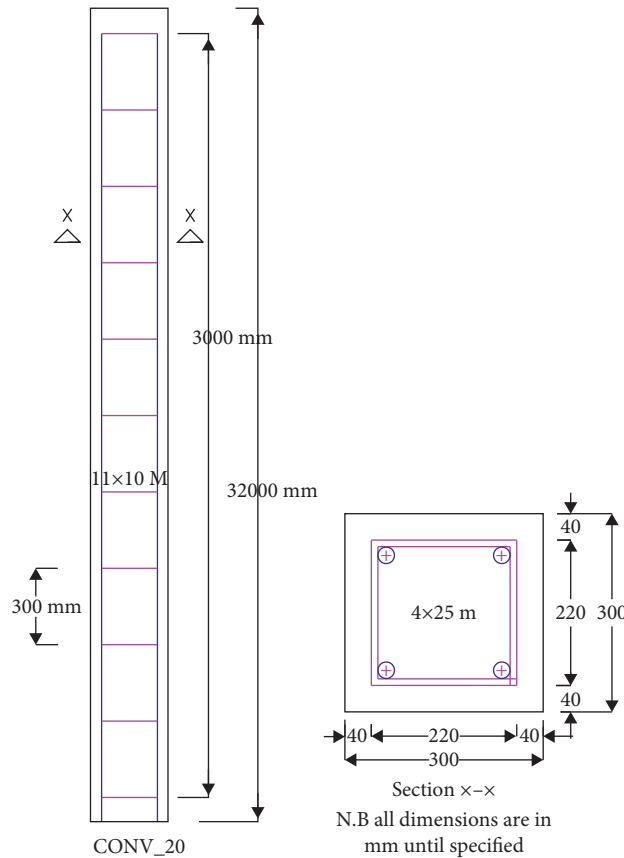


FIGURE 1: Sketch for CONV_20 RC column.

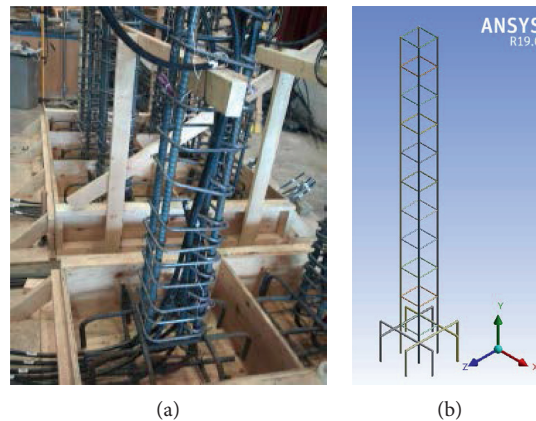


FIGURE 2: Reinforcement bar arrangement for CONV_20 RC column: (a) experiment carried out by Siba [20]; (b) AUTODYN FEA simulation.

frames, conventional (seismic deficient), and seismically detailed schemes subjected to various close-in blast loading are presented. Figures 9–15 present reinforcement details of conventional seismic deficient and seismically detailed RC columns. Conventional and seismic resistant RC columns are detailed as per EN 1992-1 EuroCode2 [31] and EN 1998-1:2003 EuroCode8 [32], respectively. All columns and beams had 300 mm × 300 mm cross-sections reinforced with 8 ϕ 12 mm and 6 ϕ 12 mm longitudinal bars, respectively. The spacing of transverse bars with ϕ 8 mm ties is detailed to have different spacing along with the height of beam and column.

FRM_REI_DET_#1 represents conventional frame for only gravity loading only, whereas FRM_REI_DET_#2 and FRM_REI_DET_#3 are seismic resistant frames.

5. Parametric Study Results and Discussions

In this section, a numerical study using the nonlinear computational FEA program, ANSYS AUTODYN, on effect of different reinforcement detailing provisions on a two-story one-bay RC framed structure under a blast-induced shock wave is presented. Figure 16 elucidates the indoor

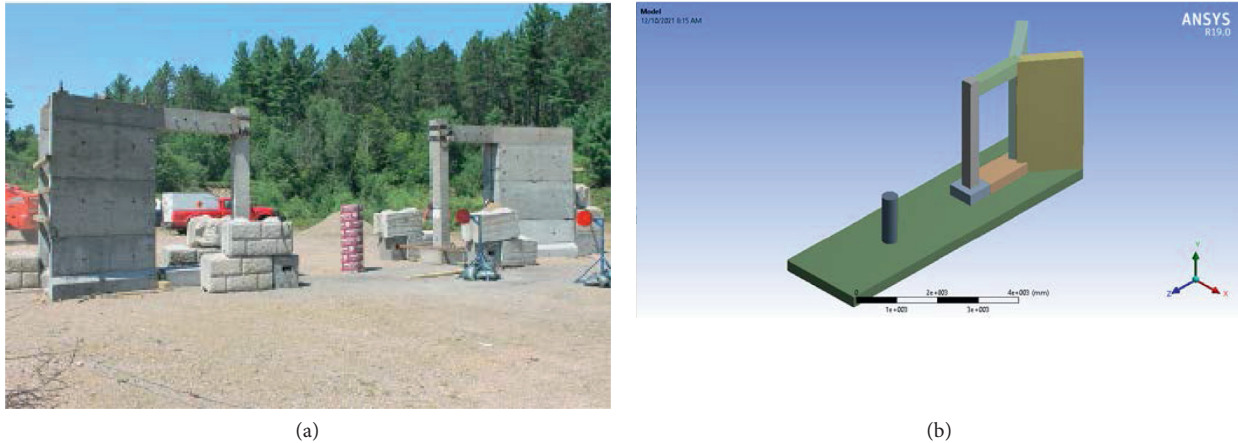


FIGURE 3: CONV_20 test column and location of 150 kg ANFO explosive: (a) experiment carried out by Siba [20]; (b) AUTODYN FEA simulation.

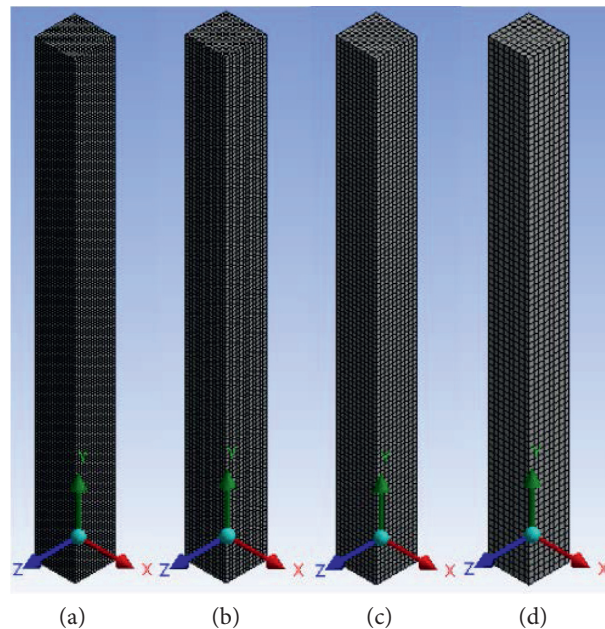


FIGURE 4: AUTODYN FEA model for CONV_20 RC column with different mesh sizes: (a) 20 mm; (b) 25 mm; (c) 30 mm; (d) 40 mm.

location of equivalent TNT explosives, simulating various blast loading scenarios used in the present parametric study.

The parametric study consisted of three blast scenarios with reference to two blast points specifically located at the middle of the 1st and 2nd story levels. The first blast scenario had 46 kg TNT explosive charge mass and a $0.50 \text{ m/kg}^{1/3}$ scaled distance, whereas in the second blast load case, a 91 kg TNT explosive charge mass was applied yielding a $0.40 \text{ m/kg}^{1/3}$ scaled distance. The third blast scenario had a 215 kg TNT explosive charge mass with $0.30 \text{ m/kg}^{1/3}$ scaled distance.

The 3D frame had a $5 \text{ m} \times 5 \text{ m}$ planar area and a 3 m floor height. In addition to the self-weight of each structural member (column, beam, and slab), 10 kN/m^2 live load characterized by the functional use of the floor system is imposed on 1st and 2nd story floor slabs.

Among the structural elements of a building, the column is a critical structural element subjected mainly to

compression with/without bending, and is highly susceptible to early failure due to blast loading. Consequently, damage on columns trigger a whole frame system into progressive collapse. Thus, average damage index and effective plastic strain values were extracted from AUTODYN's postprocessed data files for the first and second story columns. Figure 17 elucidates ANUTODYN FEA models with indoor locations of TNT explosive, 3D model with and without meshes.

Sample detonation phases of TNT explosive on the 1st and 2nd floors with respective pressure values on the 3D FEA model are presented in Figure 18. Blast modelling is made by using ANSYS AUTODYN software and explicit analysis of those frames with and without seismic detailing provisions is performed for close-in extreme blast load cases. For a TNT explosive charge mass located on the first floor, ground floor columns suffered greater pressure than 2nd floor columns and on the contrary,

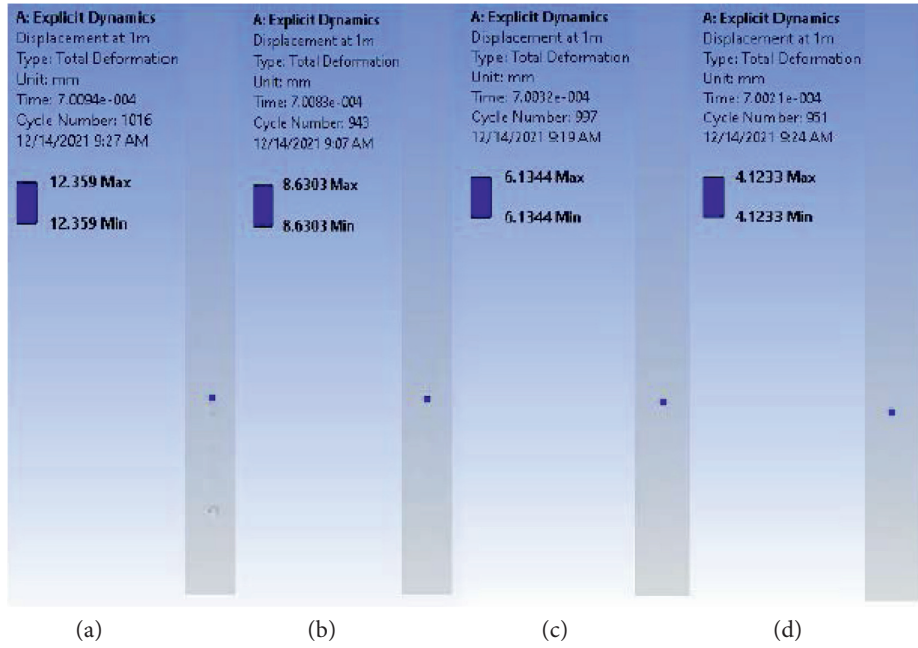


FIGURE 5: Nodal displacement value for CONV_20 RC column located at 1 m control point: (a) 20 mm; (b) 25 mm; (c) 30 mm; (d) 40 mm.

TABLE 8: Mesh sensitivity analysis.

Mesh size (mm)	No. of nodes	No. of elements	Time elapsed (s)	Maximum displacement at lower one-third (mm)
20	43779	38250	1500	12.35
25	23153	19584	1080	8.63
30	13915	11400	960	6.14
40	6966	5440	900	4.12

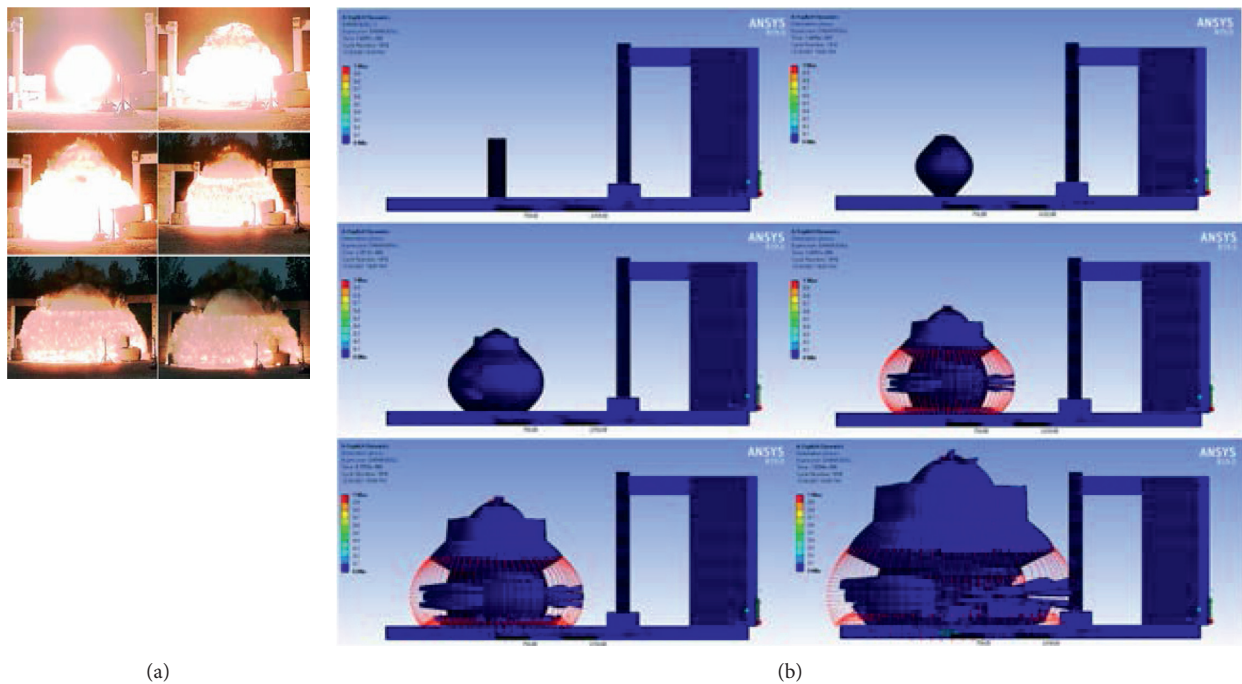


FIGURE 6: Blast wave propagation: (a) field test carried out by Siba [20]; (b) FEA simulation.

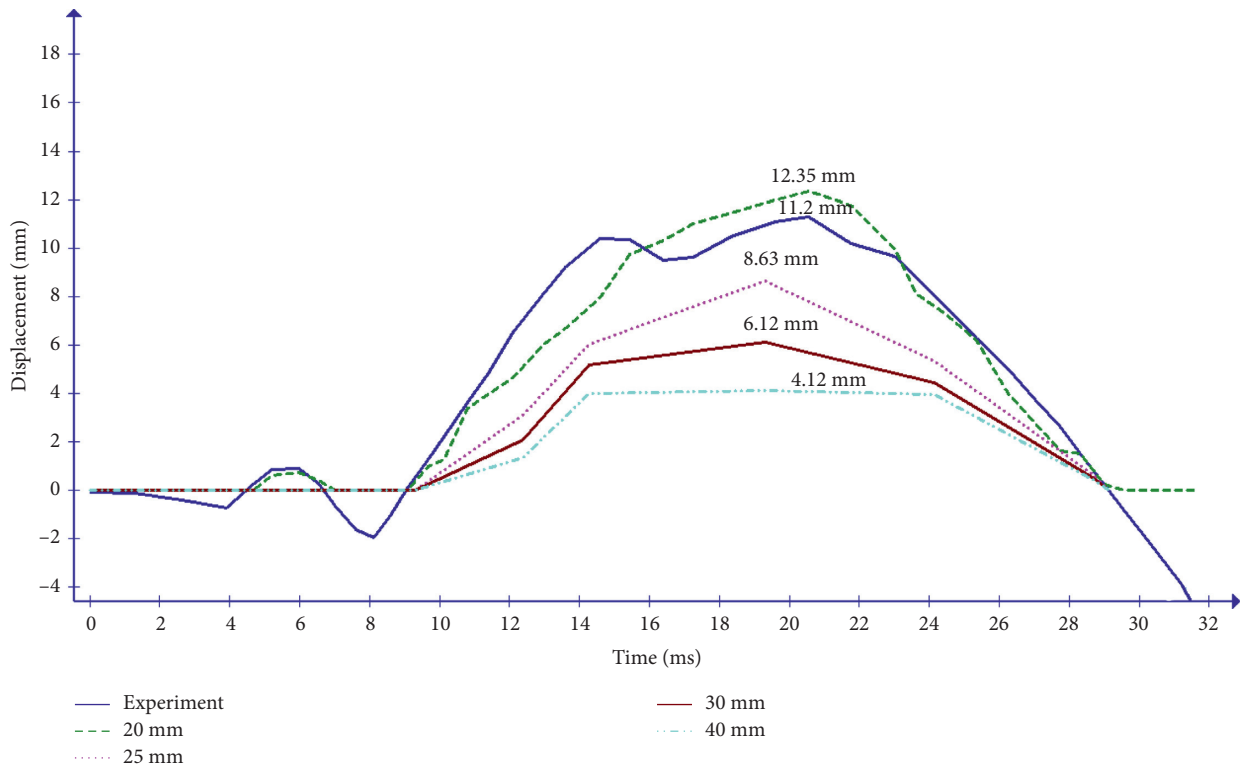


FIGURE 7: Displacement-time history curves for CONV_20 RC column with different mesh sizes.

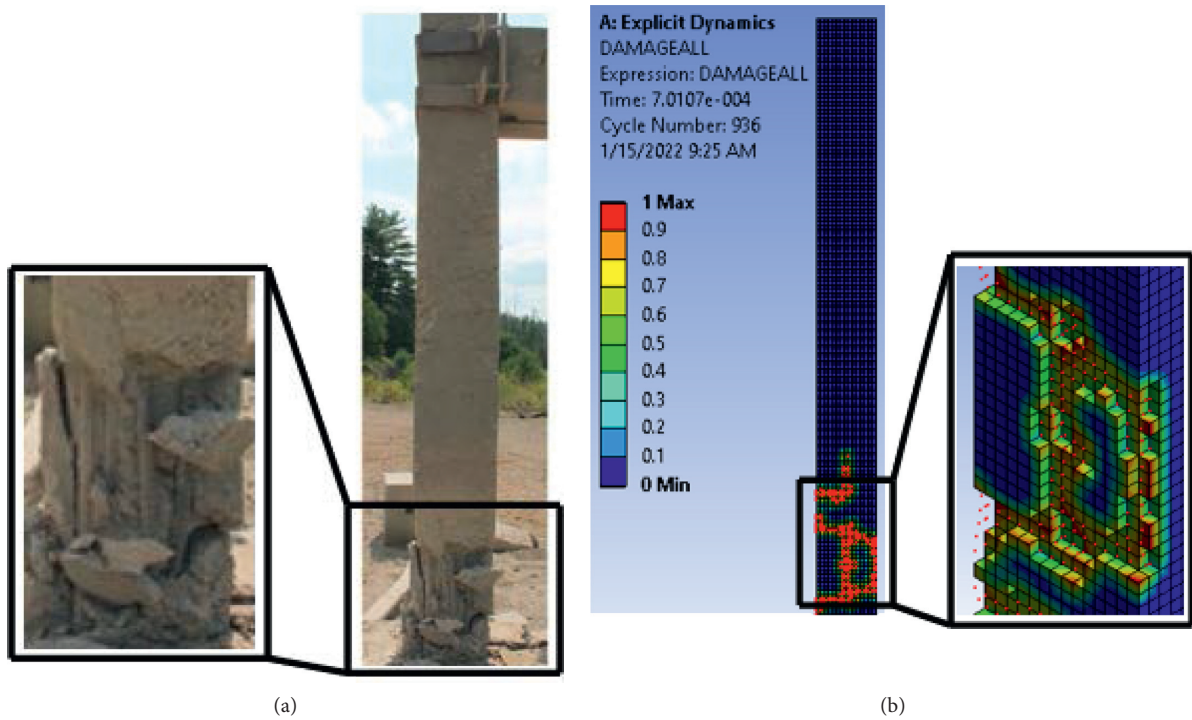


FIGURE 8: Posttest photograph of column: (a) field test carried out by Siba [20] and (b) FE validation result.

when the TNT explosive is allowed to detonate in the 2nd floor, columns located on the respective floor are exposed to maximum blast-induced shock waves (Figure 18).

5.1. Blast Loading Response of Seismically Detailed Two-Story One-Bay RC Building Frame. This section presents a performance assessment of the seismically detailed RC frame

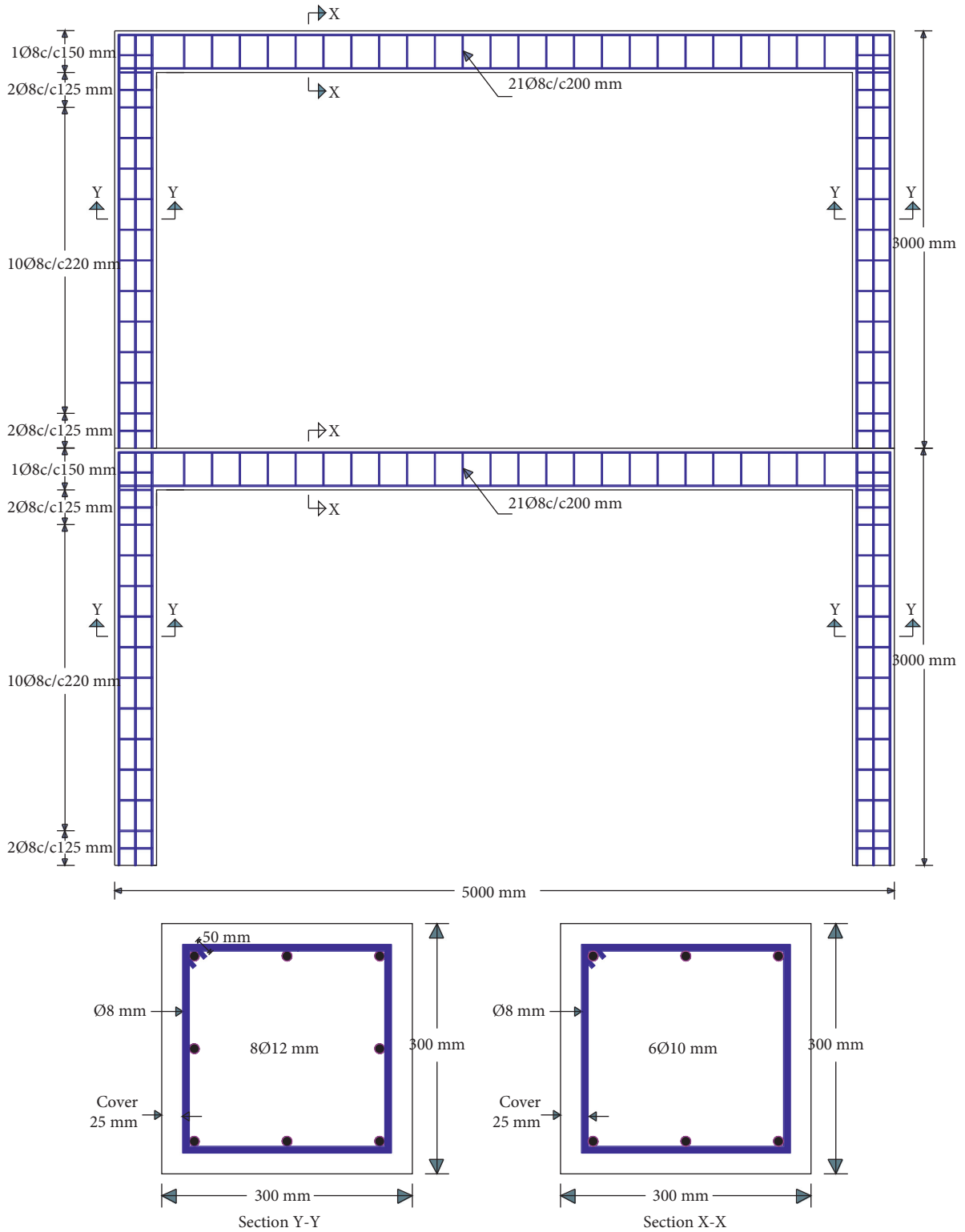


FIGURE 9: Reinforcement detailing for FRM_REI_DET_#1.

under blast loading. One conventional RC frame, FRM_REI_DET_#1, and two seismically detailed RC frames, FRM_REI_DET_#2 and FRM_REI_DET_#3, are studied with two probable indoor explosion locations (1st and 2nd

story floor levels) and three different equivalent TNT explosive material charge masses (46 kg, 91 kg, and 215 kg).

FE numerical analysis results showed as charge mass increases, damage and effective plastic strain values also

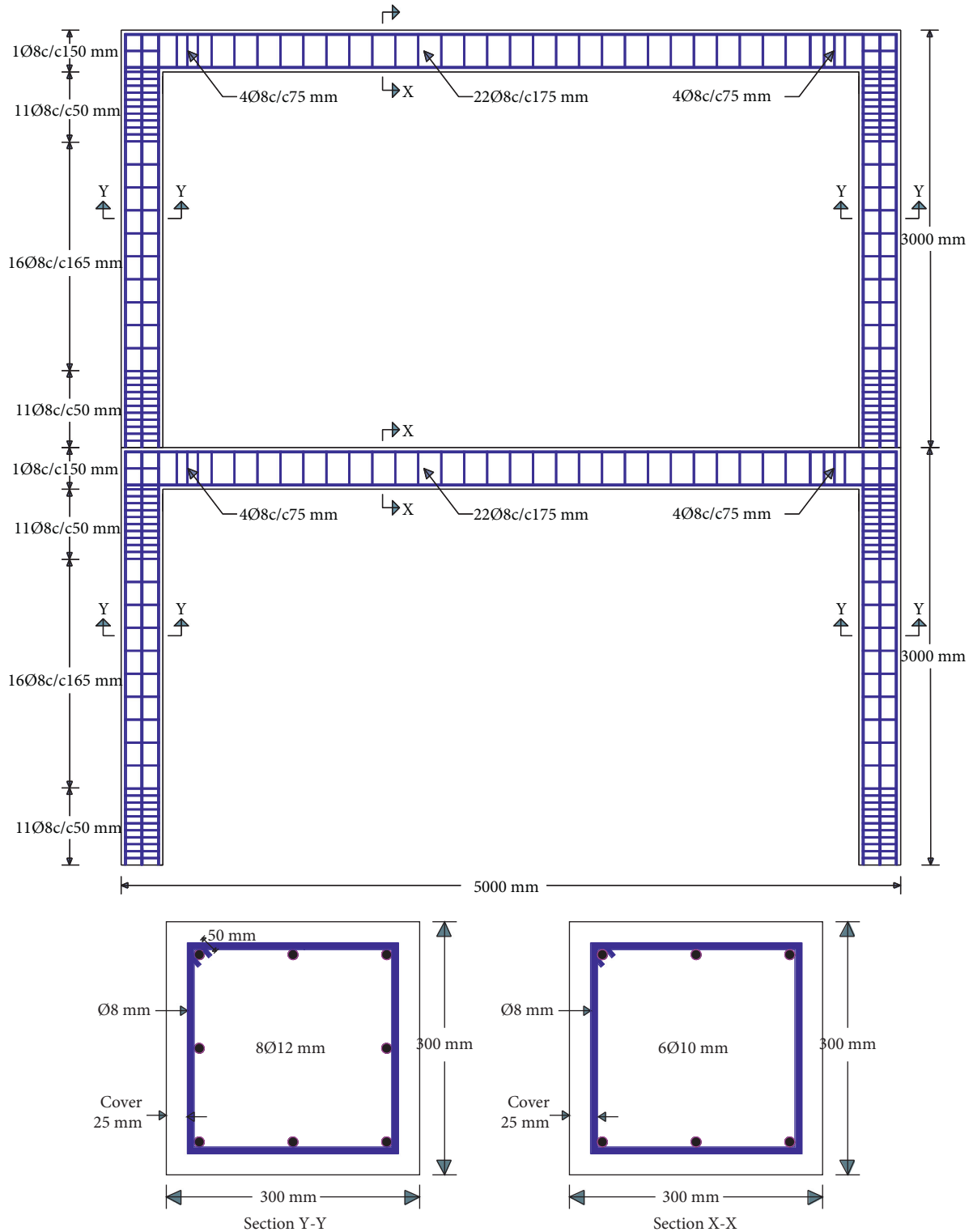


FIGURE 10: Reinforcement detailing for FRM_REI_DET_#2.

peaked. Moreover, as compared to conventionally detailed RC frames (FRM_REI_DET_#1), seismically detailed RC frames (FRM_REI_DET_#2 and FRM_REI_DET_#3) performed well under blast loading. For $0.50 \text{ m/kg}^{1/3}$ scaled distance, where TNT explosive is kept at 1st floor, and damages are reduced by 14.3% and 62% for RC frames FRM_REI_DET_#2

and FRM_REI_DET_#3, respectively (Figure 19). On the other hand, when TNT explosive is placed at 2nd story, the values are 16.7% and 62.5% (see Figure 20).

Similarly, for a $0.40 \text{ m/kg}^{1/3}$ scaled distance where TNT explosive is located at the 1st story floor level, 11.8% and 47.1% drop in damage values are observed (Figure 21). On the other

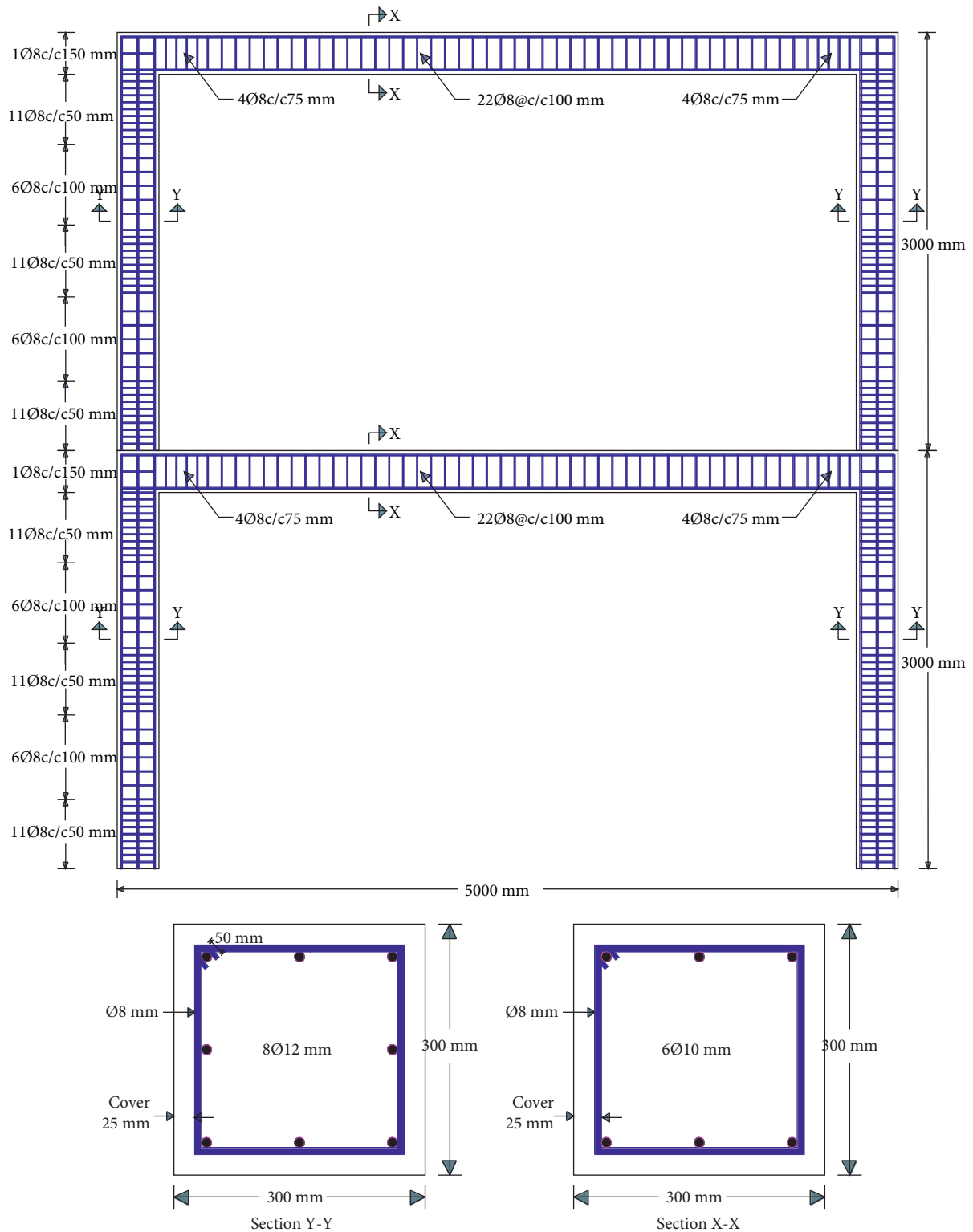


FIGURE 11: Reinforcement detailing for FRM_REI_DET_#3.

hand, for TNT explosive with the same $0.40 \text{ m/kg}^{1/3}$ scaled distance kept at 2nd story, decrease in damage value up to 10% and 47.5%, respectively, was observed (see Figure 22).

Figures 23 and 24 show performance gain of applying explosives with $0.30 \text{ m/kg}^{1/3}$ scaled distance at 1st and 2nd

story floor levels, and damages lessened by 10%, 56.4% and 9.5%, 56.4%, respectively were recorded for FRM_REI_DET_#2 and FRM_REI_DET_#3 RC frames, respectively.

Figures 25 and 26 present a summary of the performance of seismic deficient and seismically detailed columns. From the

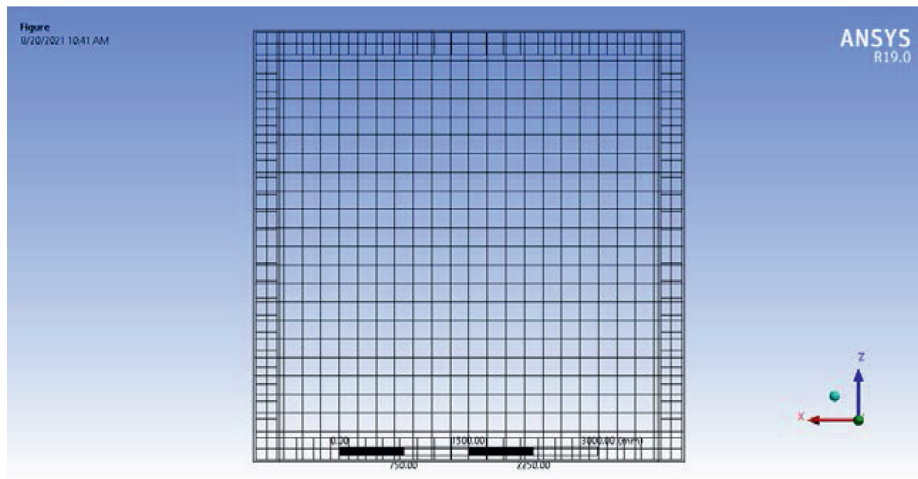
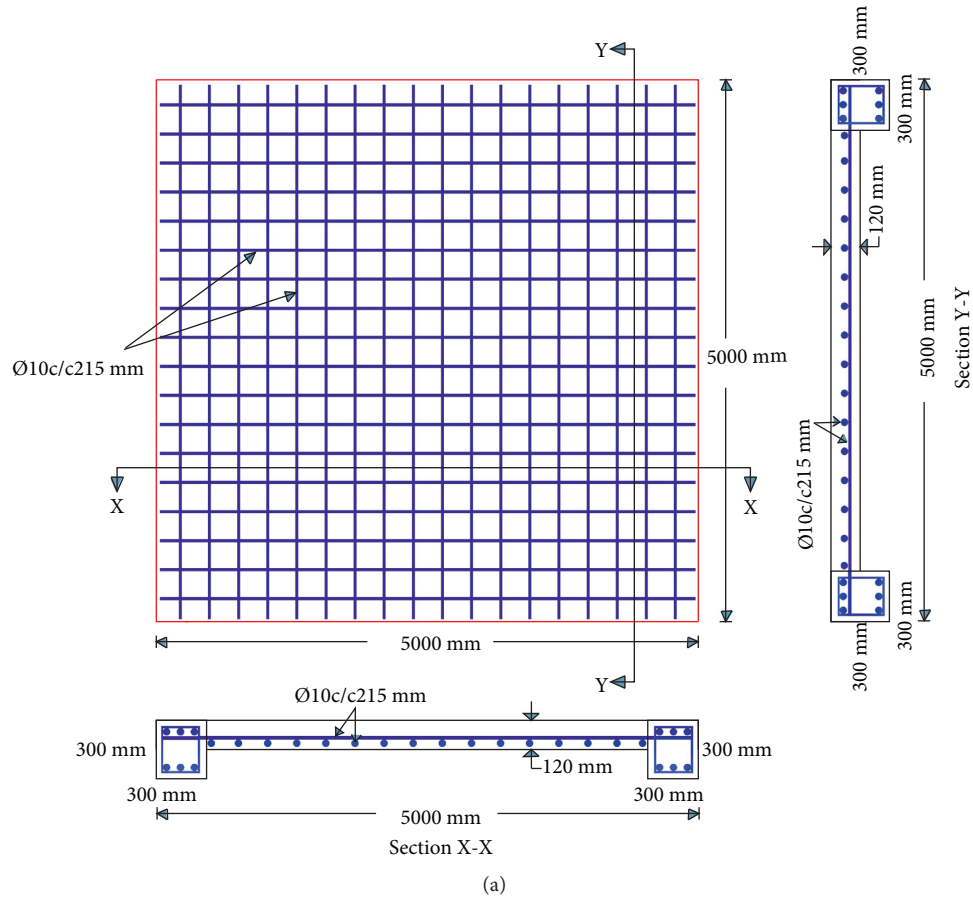


FIGURE 12: Solid slab reinforcement detailing for FRM_REI_DET_#1, FRM_REI_DET_#2, and FRM_REI_DET_#3 models: (a) sketch; (b) FEA model.

plot, it is evident that a decrease in scaled distances from $0.50 \text{ m/kg}^{1/3}$ to $0.30 \text{ m/kg}^{1/3}$ induced severe damages to the columns especially FRM_REI_DET_#1 and FRM_REI_DET_

#2. On the contrary, FRM_REI_DET_#3 showed an incredible performance and robust resistance against close-in explosion scenarios.

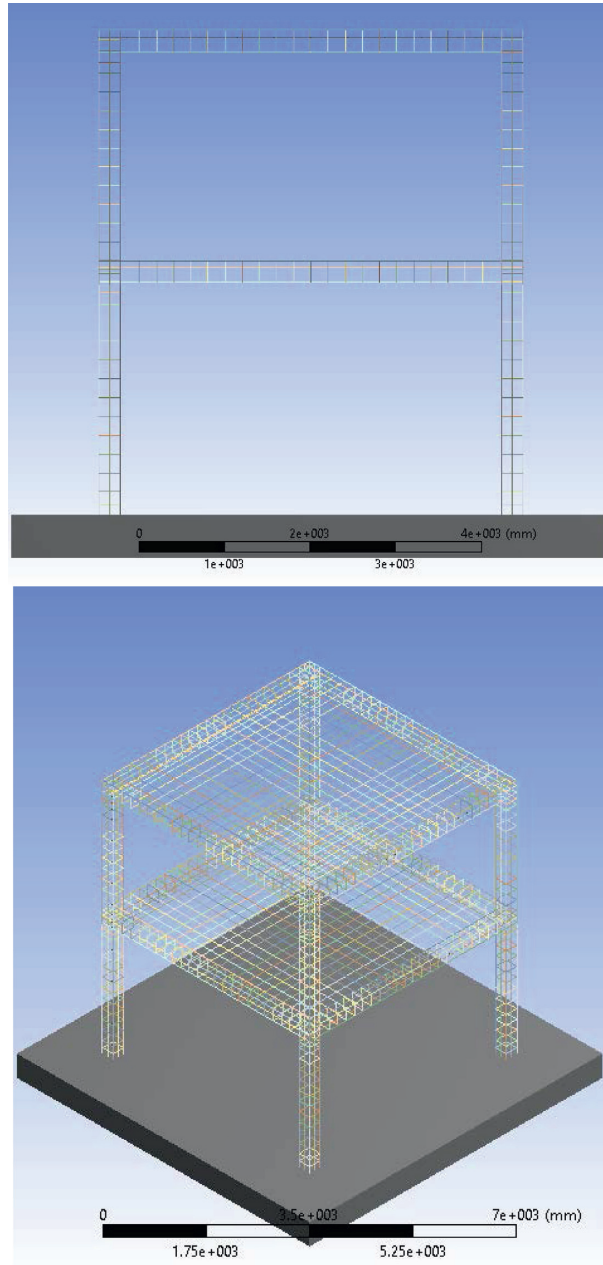


FIGURE 13: Reinforcement detailing for FRM_REI_DET_#1 on AUTODYN.

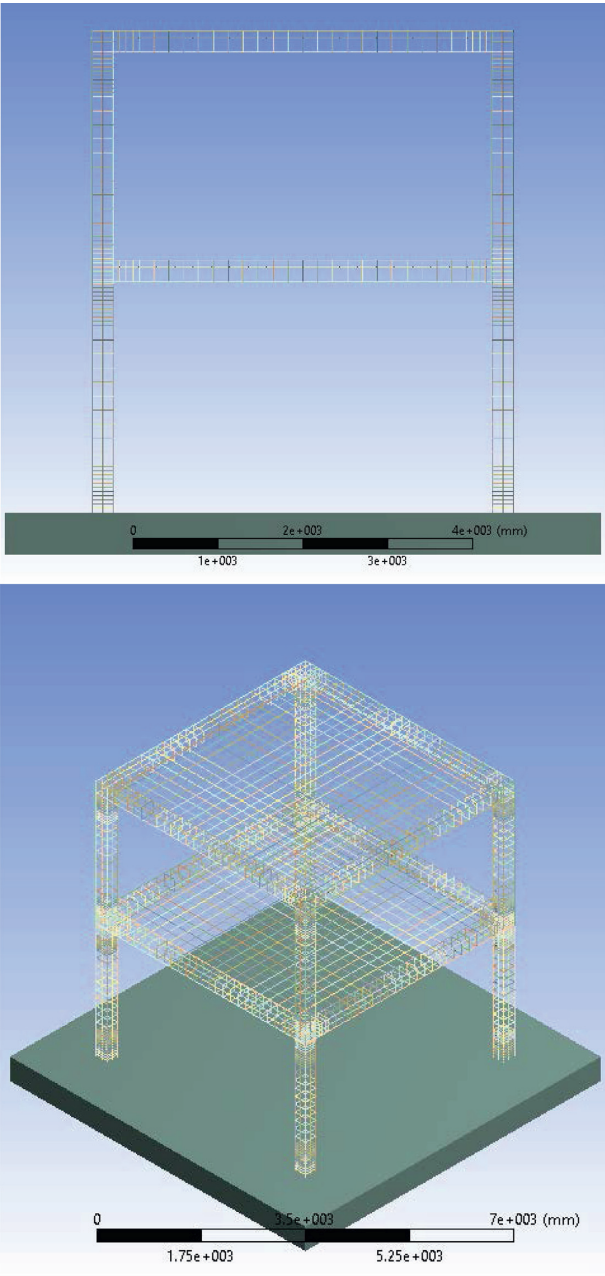


FIGURE 14: Reinforcement detailing for FRM_REI_DET_#2 on AUTODYN.

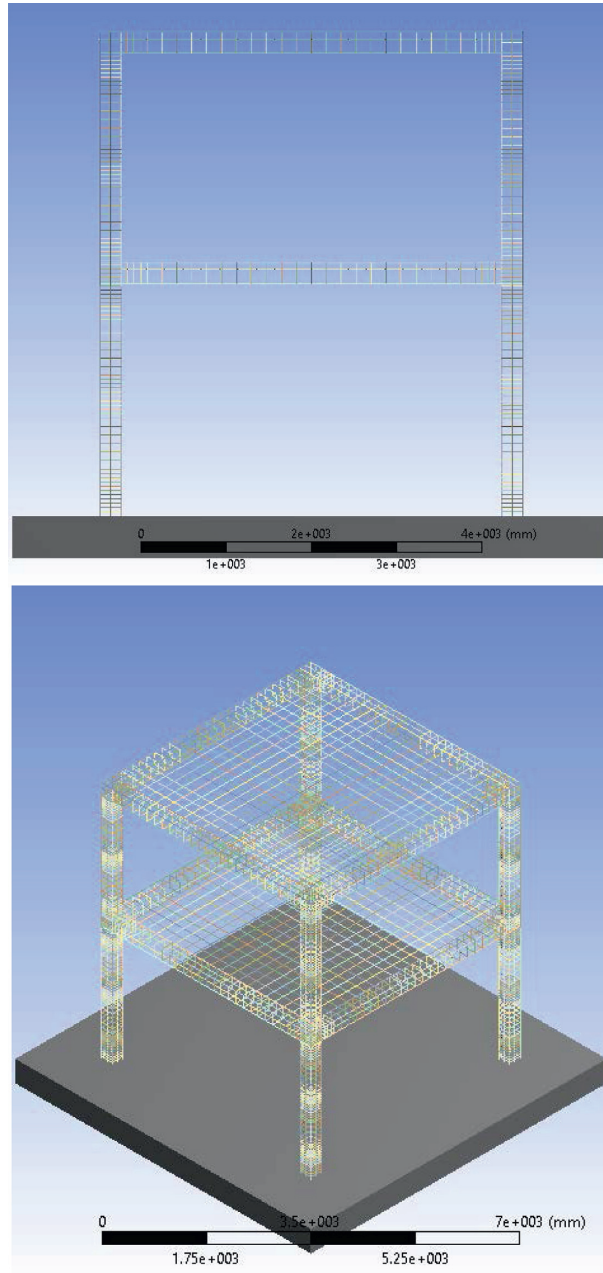


FIGURE 15: Reinforcement detailing for FRM_REI_DET_#3 on AUTODYN.

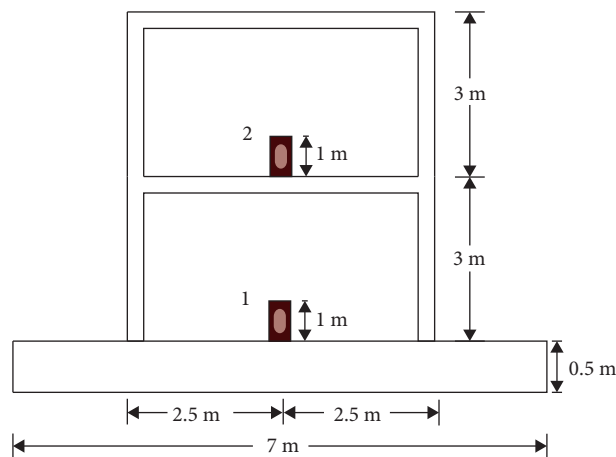


FIGURE 16: Locations of TNT explosives.

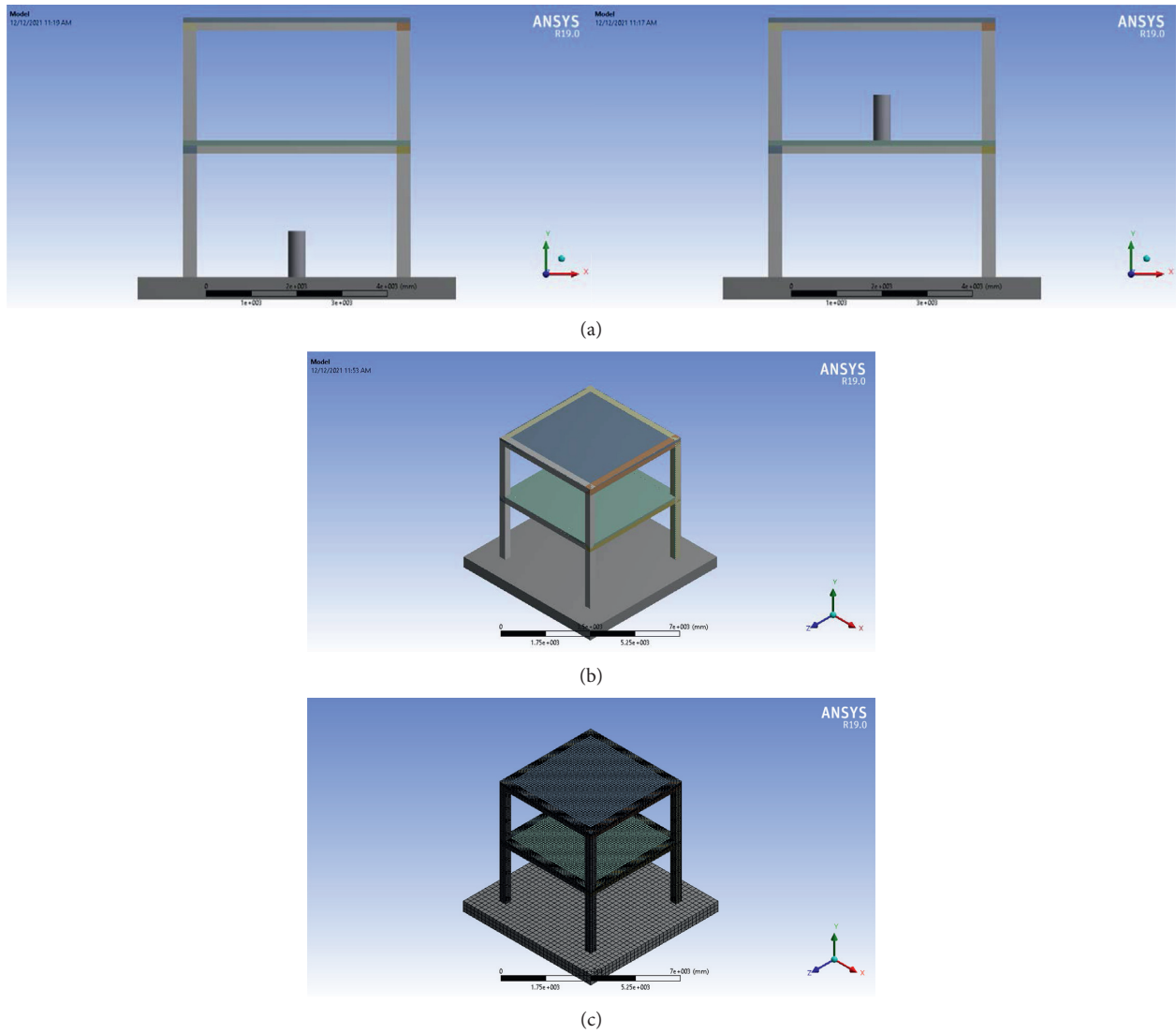


FIGURE 17: ANUTODYN FEA model with (a) location of TNT explosive, (b) 3D plot, and (c) meshes.

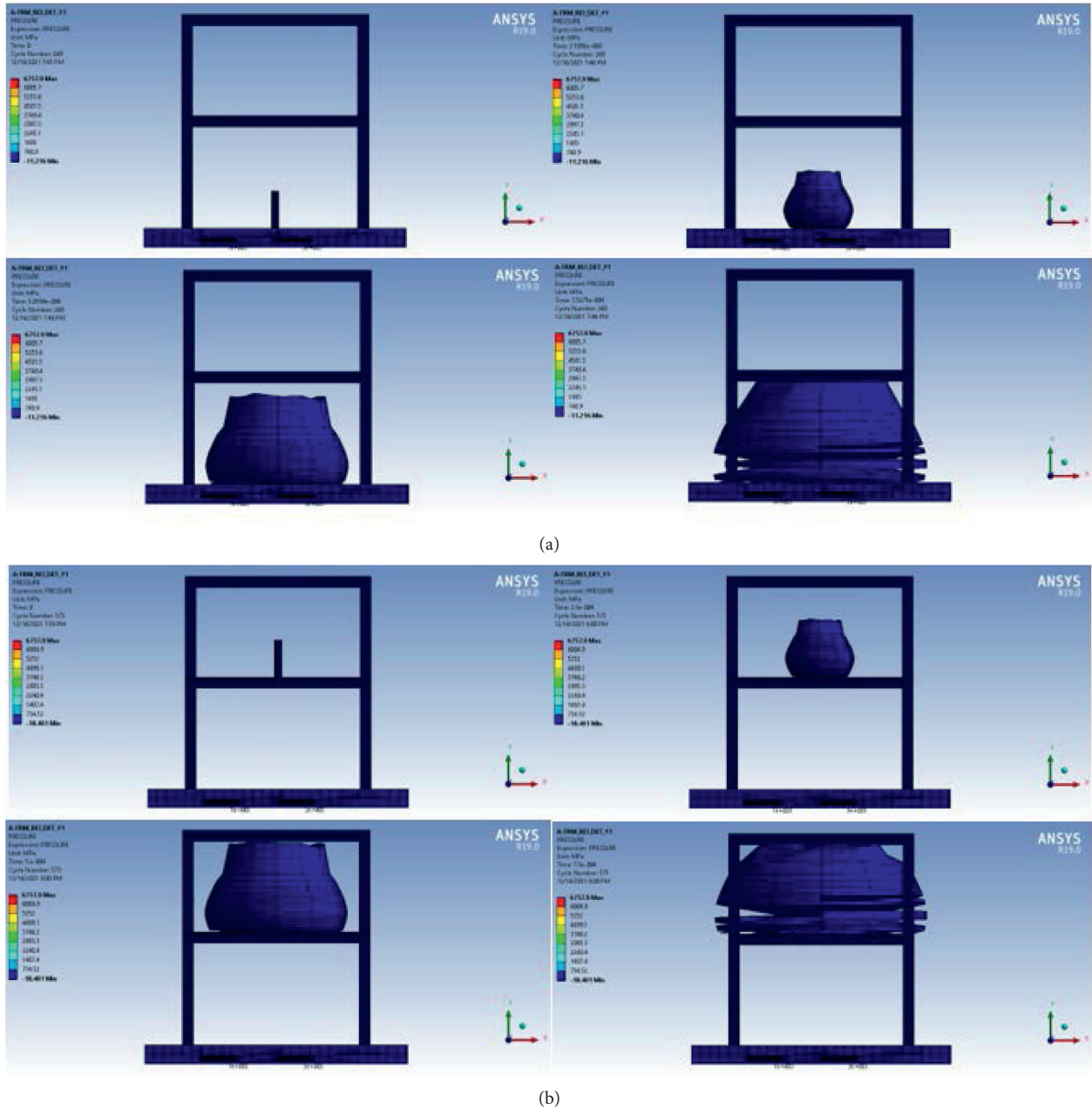


FIGURE 18: Blast pressure wave propagation time for two blast scenarios.

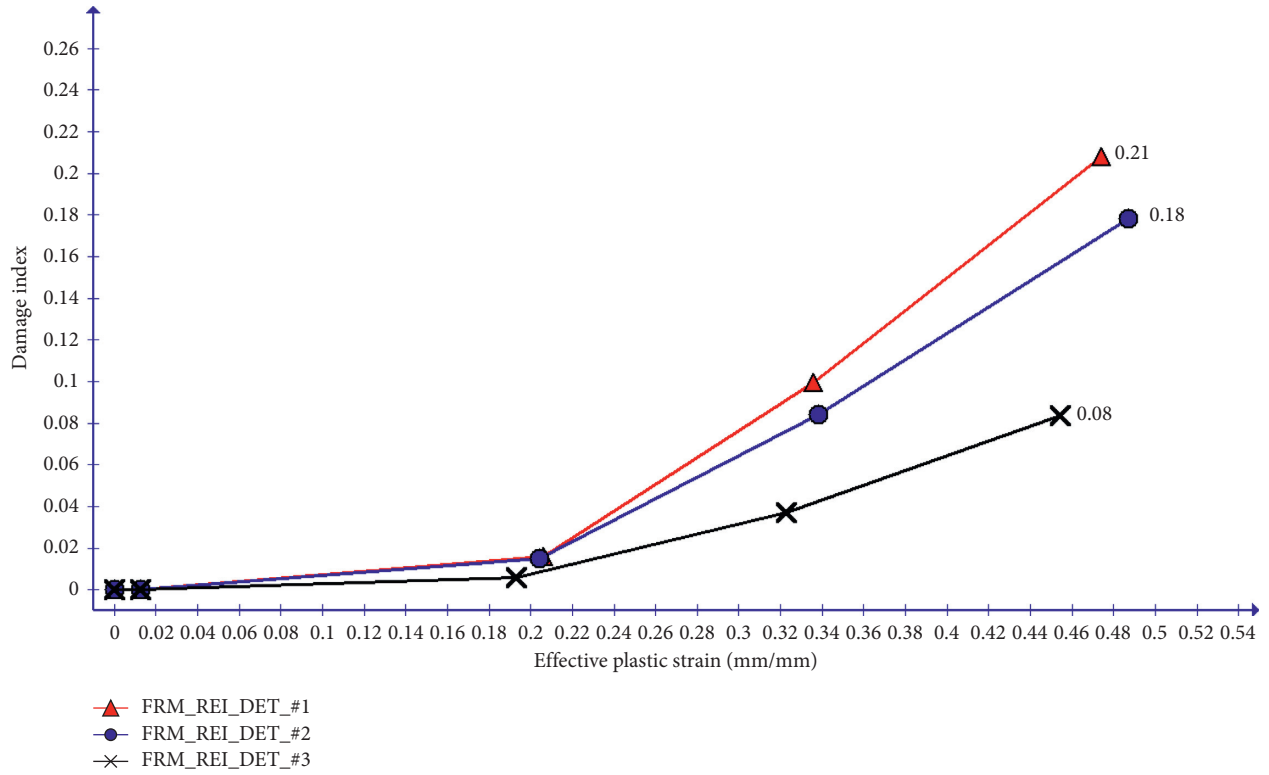


FIGURE 19: Column damage index vs. effective plastic strain plot for 46 kg TNT explosive located at 1st story ground floor slab.

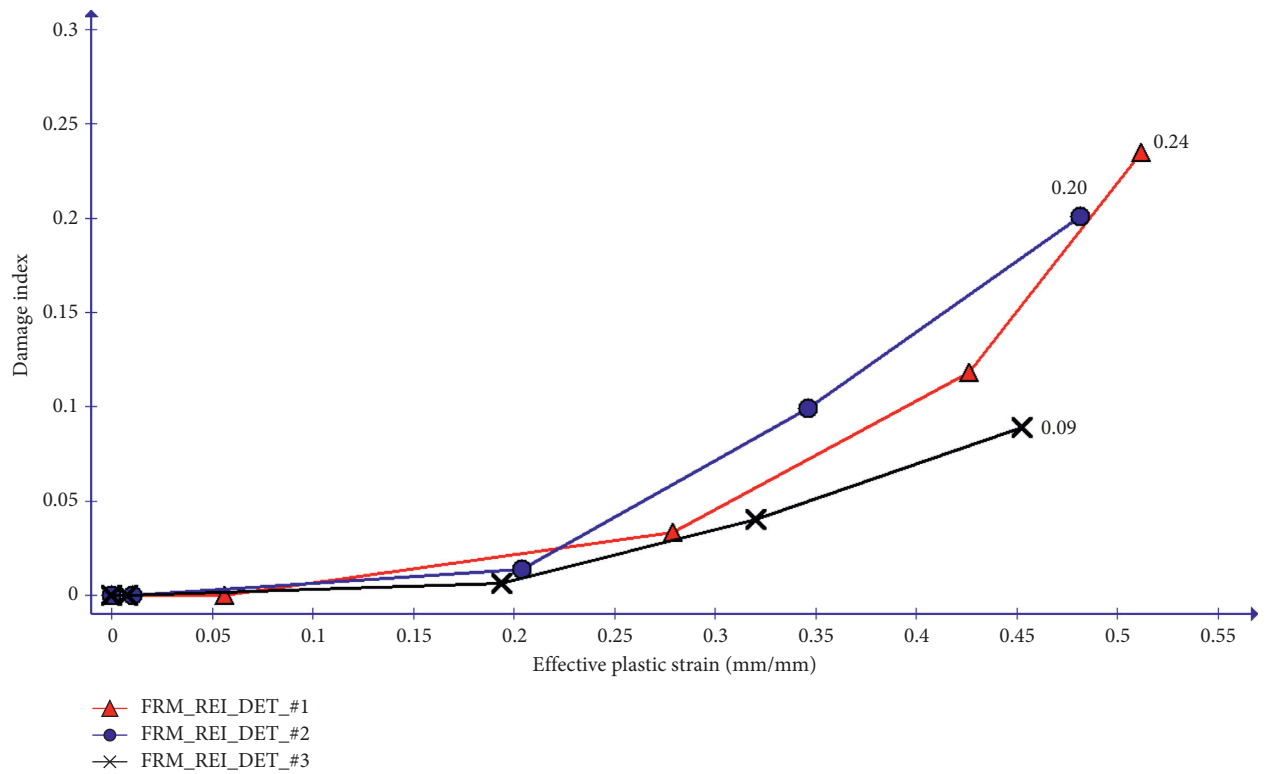


FIGURE 20: Column damage index vs. effective plastic strain plot for 46 kg TNT explosive located at 2nd story floor slab.

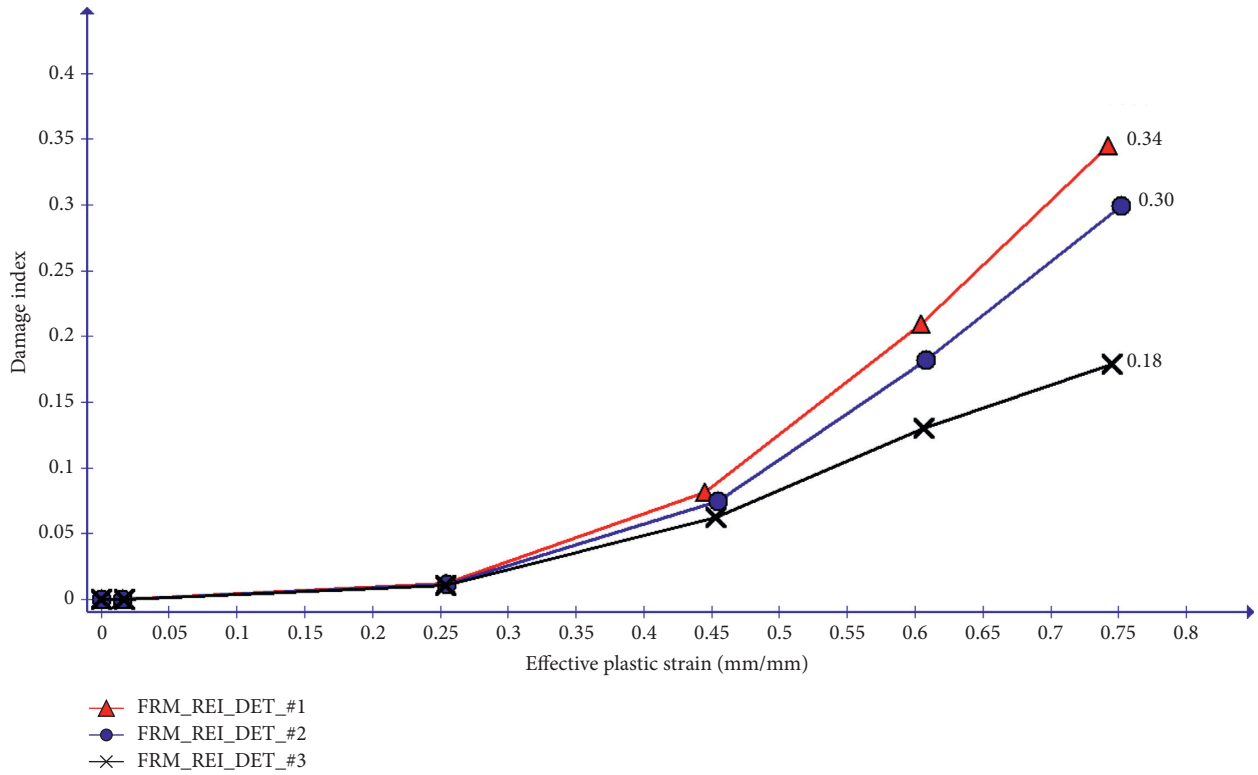


FIGURE 21: Column damage index vs. effective plastic strain plot for 91 kg TNT explosive located at 1st story ground floor slab.

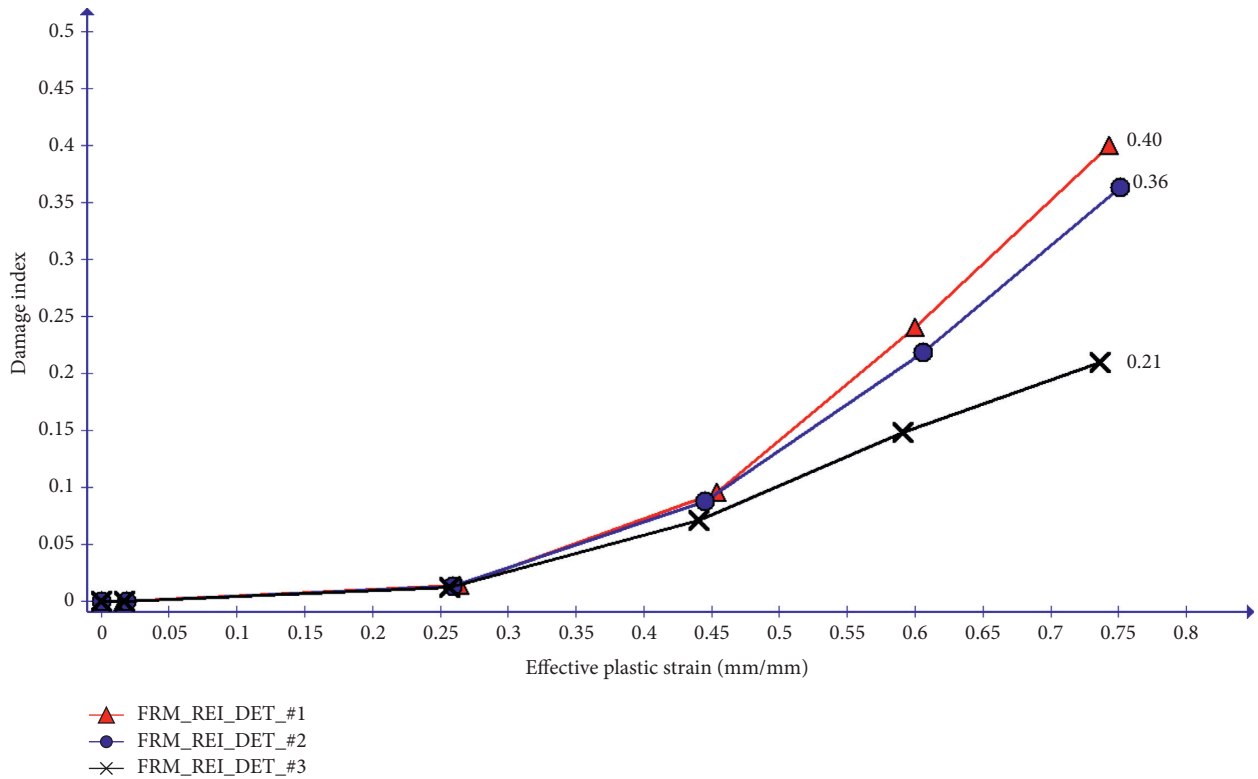


FIGURE 22: Column damage index vs. effective plastic strain plot 91 kg TNT explosive located at the 2nd story floor slab.

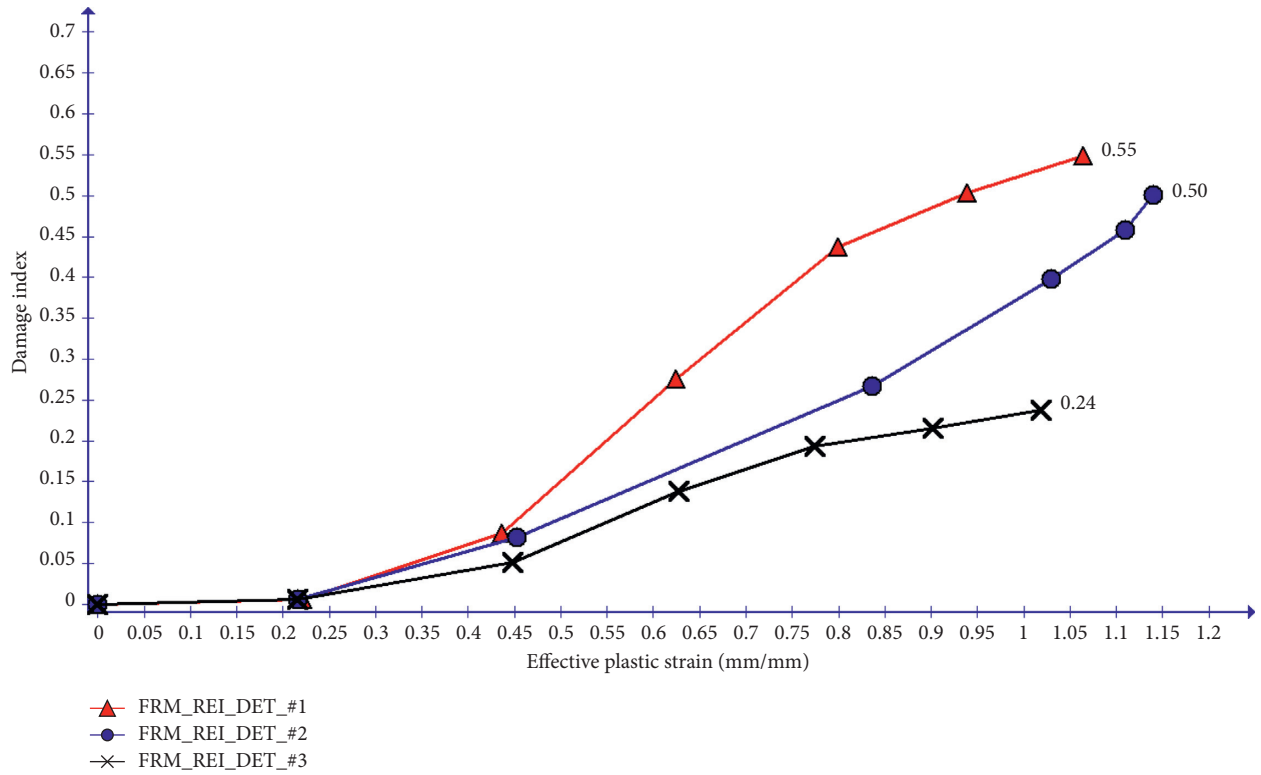


FIGURE 23: Column damage index vs. effective plastic strain plot for 215 kg TNT explosive located at 1st story ground floor slab.

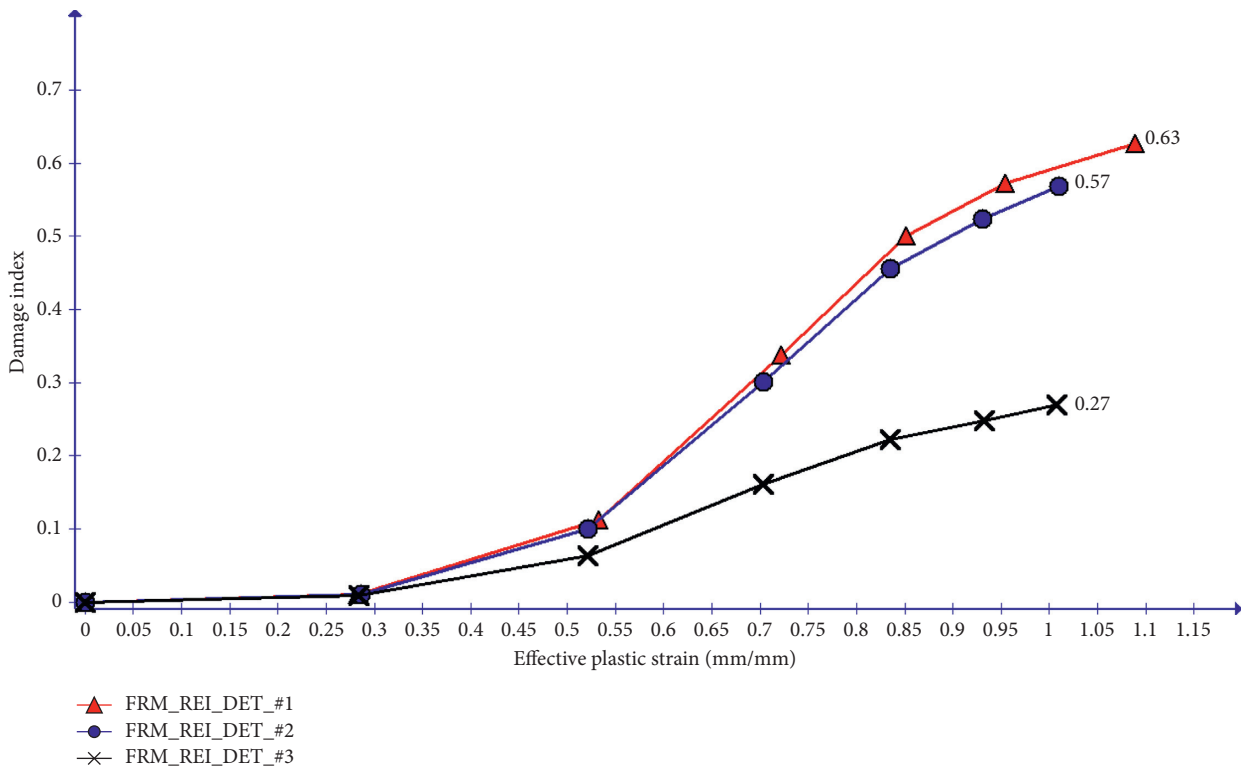


FIGURE 24: Column damage index vs. effective plastic strain plot for 215 kg TNT explosive located at 2nd story floor slab.

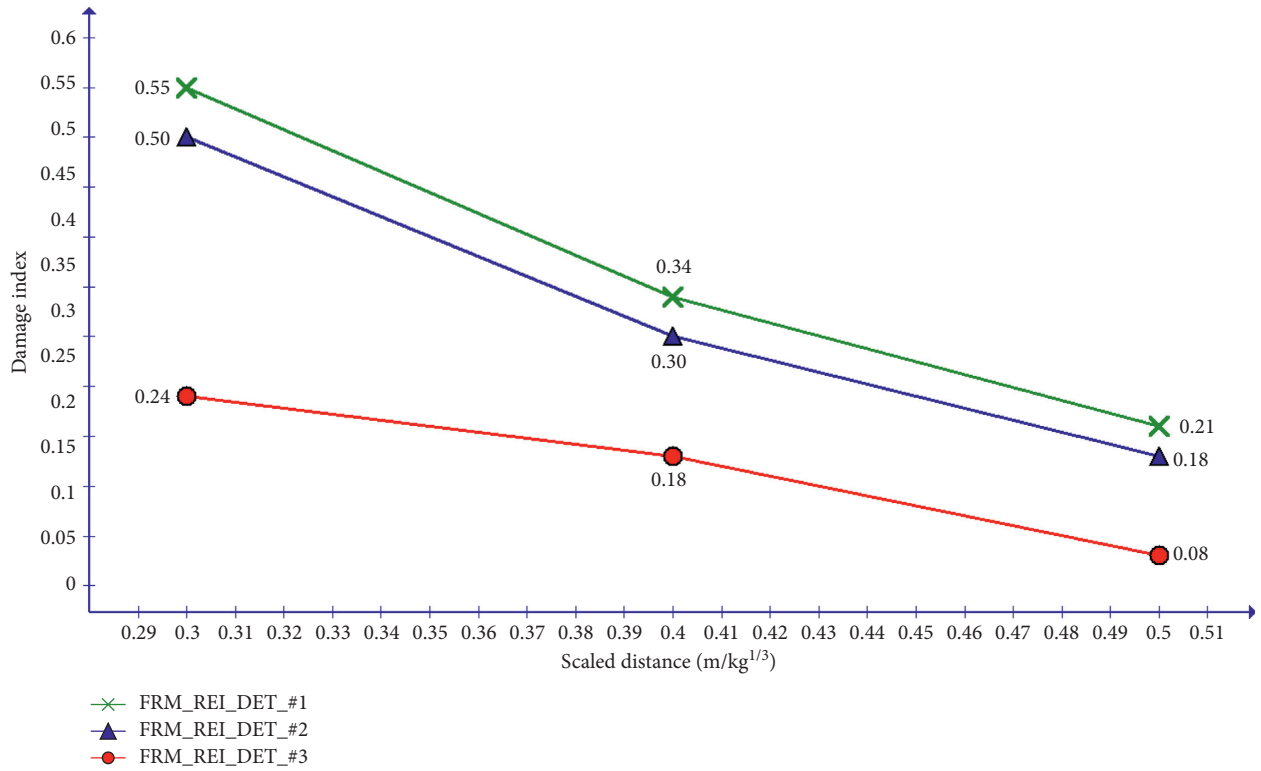


FIGURE 25: 1st story column damage index values for different reinforcement detailing provisions under various scaled distances.

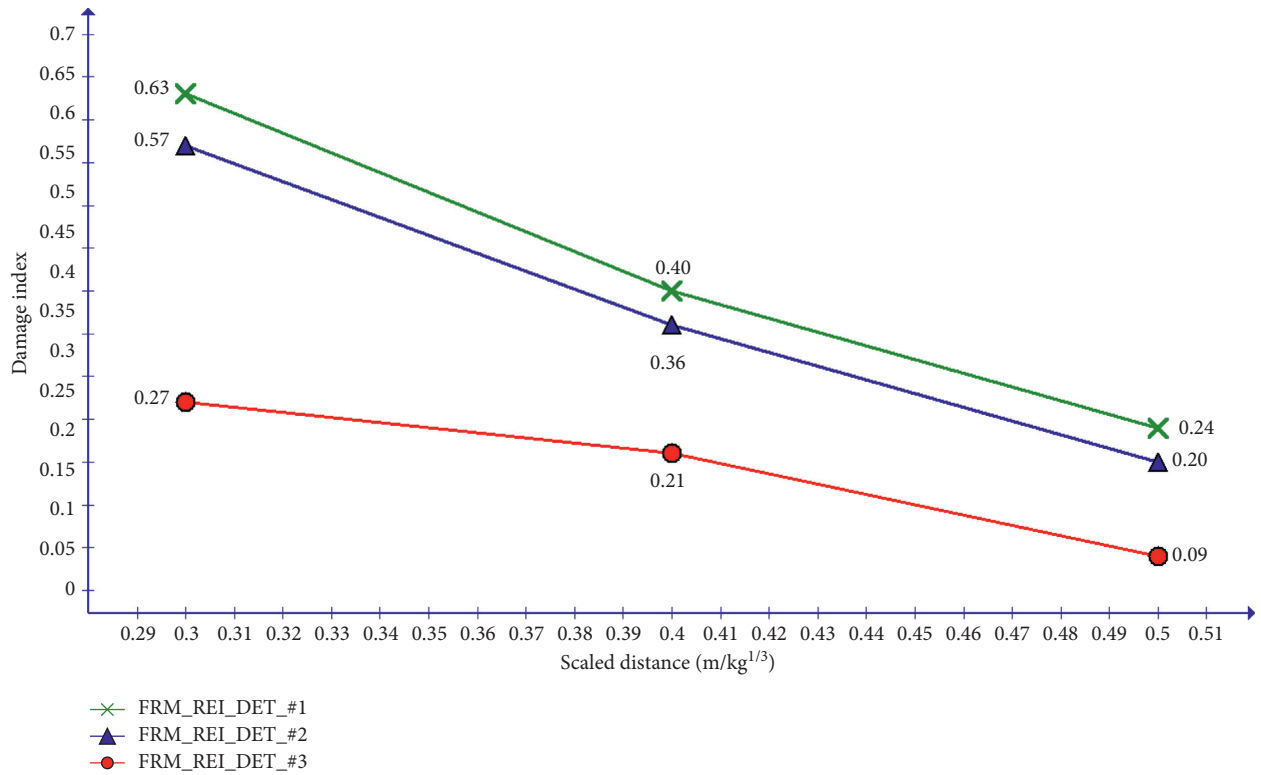


FIGURE 26: 2nd story column damage index values for different reinforcement detailing provisions under various scaled distances.

6. Conclusion

The present research investigated the structural performance assessment of two-story, one-bay conventional, and seismic resistant reinforced concrete framed buildings under close-in blast loading. Influential variables such as charge mass, explosive scaled distances, and various reinforcement detail provisions are studied to get insight into the blast load resistance of a reinforced concrete frame structure. Next, the major findings of the study are summarized.

- (i) For a given close-in blast event, the decrease in scaled distance parameter increased, which results in effective plastic strain and damage indices
- (ii) Minimizing transverse steel reinforcement spacing in a column significantly caused a drop in damage indices
- (iii) Comparing seismic deficient columns with seismically detailed RC columns and having various blast scenarios with different scaled distances, the simultaneous use of closed spaced transverse steel reinforcement spacings in ends and midheight of reinforced concrete columns is found to be highly effective in reducing both effective plastic strains and damage index values

Data Availability

All data are included in the manuscript.

Conflicts of Interest

The authors declare that they have no conflicts of interest.

References

- [1] G. Valsamos, M. Larcher, and F. Casadei, "Beirut explosion 2020: a case study for a large-scale urban blast Simulation," *Journal of Safety Science*, vol. 137, 2021.
- [2] J. Jayasooriya, *Vulnerability and Damage Analysis of Reinforced Concrete Framed Buildings Subjected to Near-Field Blast Events*, Queensland University of Technology, Australia, 2010.
- [3] S.-E. Kim and D.-K. Thai, "Numerical investigation of the damage of RC members subjected to blast loading," *Engineering Failure Analysis*, vol. 92, pp. 350–367, 2018.
- [4] Y. Temsah, J. Ali, J. Khatib, and M. Sonebi, "Numerical analysis of a reinforced concrete beam under blast loading," *MATEC Web of Conferences*, vol. 149, pp. 1–5, 2018.
- [5] Li Chen, B. Rao, F. Qin, J. Hong, Z.-xian Liu, and H. b. Xiang, "Dynamic response of reinforced concrete beams under double-end-initiated close-in explosion," *Defence Technology*, vol. 14, pp. 527–539, 2018.
- [6] S. Andersson and H. Karlsson, *Structural Response of Reinforced concrete Beams Subjected to Explosions*, Göteborg, Sweden, 2012.
- [7] D. Rajkumar, R. Senthil, B. M. Kumar, and K. A. Gomathi, "Numerical study on parametric analysis of reinforced concrete column under blast loading," *Journal of Performance of Constructed Facilities*, vol. 1, p. 12, 2020.
- [8] S. Astarlioglu, T. Krauthammer, D. Morency, and T. P. Tran, "Behavior of reinforced concrete columns under combined effects of axial and blast-induced transverse loads," *Engineering Structures*, vol. 55, pp. 26–34, 2013.
- [9] B. Li, A. Nair, and K. Qian, "Residual axial capacity of reinforced concrete columns with simulated blast loading," *Journal of Performance of Constructed Facilities*, vol. 287, p. 299, 2012.
- [10] Z. Wenjiao, X. Kong, Y. Qu, and Q. Zhao, "Numerical simulation of cracked reinforced concrete slabs subjected to blast loading," *Civil Engineering Journal*, vol. 4, no. 2, pp. 320–333, 2018.
- [11] N. K. Vijitha, A. B. Pau, and R. Ahani, "Prediction of blast loading and its effects on waffle slab," *International Journal for Research in Applied Science and Engineering Technology*, vol. 5, pp. 864–871, 2017.
- [12] J. K. R. Nalagotla, *Pressure-impulse Diagrams Using Finite Element Analysis for Reinforced concrete Slabs Subjected to Blast Loading*, University of Missouri-Kansas, Kansas, MO, USA, 2013.
- [13] P. Vinothini and S. Elavenil, "Analytical investigation of high rise building under blast loading," *Indian Journal of Science and Technology*, vol. 9, no. 18, pp. 1–9, 2016.
- [14] H. Draganic and V. Sigmund, "Blast loading on structures," *Tehnički Vjesnik*, vol. 19, pp. 643–652, 2012.
- [15] Q. Kashif and M. B. Varma, "Effect of blast on G+4 RCC frame structure," *International Journal of Emerging Technology and Advanced Engineering*, vol. 4, no. 11, Article ID 145149, 2014.
- [16] P. Tewari and A. Sharma, "Effects of blast loading on building frames," *International Research Journal of Engineering and Technology (IRJET)*, vol. 05, no. 5, pp. 4063–4069, 2018.
- [17] R. G. Williams, W. A. Wilson, and R. Dookeeram, "Analysis of the response of a one-storey one-bay steel frame to blast," *Journal of Structures*, vol. 2016, Article ID 8571542, 11 pages, 2016.
- [18] M. Murali and V. Sujisha, "Study on the response of RC frames subjected to blast loading," *International Journal of Engineering Research and Technology*, vol. 5, no. 08, pp. 602–607, 2016.
- [19] A. T. Toy and B. Sevim, "Structural response of two-storey reinforced concrete building under blasting effects," *CBU J. of Sci*, vol. 12, no. 3, pp. 419–426, 2016.
- [20] F. Siba, *Near-Field Explosion Effects on Reinforced Concrete Columns: An Experimental Investigation*, Carleton University, Ottawa, Canada, 2014.
- [21] ANSYS AUTODYN R19.0, ANSYS, Inc., Canonsburg, PA, USA.
- [22] R. M. Brannon and S. Leelavanichkul, *Survey of Four Damage Models for Concrete*, Sandia National Laboratories, California, 2009.
- [23] W. Riedel and T. Borrvall, "The RHT concrete model in LS-DYNA," in *Proceedings of the 8th European LS-DYNA User Conference*, pp. 1–14, Strasbourg, France, January 2011.
- [24] T. Borrvall, "The RHT concrete model in LS-DYNA," *8th European LS-DYNA User Conference*, vol. 1–15, 2011.
- [25] C. Heckotter and J. Sievers, "Comparison of the RHT concrete material model in LS-DYNA and ansys autodyn," in *Proceedings of the 11th European LS-DYNA Conference*, pp. 1–16, Salzburg, Austria, 2017.
- [26] J. Ekstrom, *Concrete Structures Subjected to Blast Loading*, Goteborg, 2015.
- [27] E. Lee, M. Finger, and W. Collins, *JWL Equation of State Coefficients for High Explosives*, Lawrence Livermore Laboratory, California, 1973.

- [28] H. Hamashima, Y. Kato, N. You, and S. Iloh, "Determination of JWL parameters from underwater explosion test for ideal and non-ideal explosives," *Science and Technology of Energetic Materials*, vol. 64, no. 6, pp. 248–253, 2003.
- [29] L. E. Schwer, "Jones-wilken-lee (JWL) equation of state with afterburning," in *Proceedings of the 14th International LS-DYNA User Conference*, vol. 1–38, Windsor, CA, USA, July 2016.
- [30] S. B. Segletes, *An Examination of the JWL Equation of State*, United States of America: US Army Research Laboratory, Aberdeen, Scotland, 2018.
- [31] EN, *Eurocode 2: Design of Concrete Structures - Part 1: General Rules and Rules for Buildings pr EN1992*, Brussels, Belgium, 2002.
- [32] EN, *Eurocode 8: Design of Structures for Earthquake Resistance, Part 1: General Rules, Seismic Actions, and Rules for Buildings EN1998-1-1*, Brussels, Belgium, 2003.

Research Article

Bending Performance of Precast Lightweight Aggregate Concrete Exterior Wallboard with a Concealed Rib Sandwich Structure

Congqi Li , Xinwei Ma , Ying Yang , Ahmed Ahmad Omar , Hao Wu ,
and Lei Qian 

College of Civil Science and Engineering, Yangzhou University, Yangzhou 225127, China

Correspondence should be addressed to Congqi Li; licq@yzu.edu.cn

Received 19 November 2021; Revised 23 January 2022; Accepted 1 March 2022; Published 22 March 2022

Academic Editor: Li Chen

Copyright © 2022 Congqi Li et al. This is an open access article distributed under the Creative Commons Attribution License, which permits unrestricted use, distribution, and reproduction in any medium, provided the original work is properly cited.

A new type of precast lightweight aggregate concrete exterior wallboard is proposed in this study. It is composed of inner and outer panels, an insulation layer, and concealed ribs. After adjusting the mixing ratio of lightweight aggregate concrete, light weight, bearing capacity, and good workability were guaranteed. The flexural performance of the composite exterior wallboard was studied by testing and numerical modeling of four wallboards, and the results of deflection, crack morphology, failure mode, and ultimate flexural capacity were then obtained. Additionally, the cracking and bending properties of the composite exterior wallboard were observed, and the calculation method of bending capacity and the cracking moment was studied. The calculated results coincided with the experimental data; therefore, this study provides a reference to the design and application of pre-fabricated exterior wallboards.

1. Introduction

Compared to traditional wallboard structures, the pre-fabricated exterior wallboard is characterized by excellent component quality, high construction efficiency, and green environmental protection [1], which is one of the important ways to change the wall and improve the level of building industrialization. As the building's peripheral protective components, the exterior wallboards should not only meet the mechanical properties but also the requirements of heat insulation, sound insulation, and waterproof of the protective structure.

Conventional types of exterior wallboards can be categorized as single material exterior wallboards, internal thermal insulation composite wallboards, exterior thermal insulation composite wallboards, and Sandwich thermal insulation composite wallboards. Among these, the Sandwich thermal insulation composite wallboard is composed of a concrete inner panel, insulation layer, and a concrete outer panel, where the inner and outer panels are often connected by rigid connectors. Compared with other forms of outer wallboard, the Sandwich thermal insulation composite

wallboard has the advantages of thermal insulation and durability [2]. During transportation, storage, and service, precast wallboards are normally affected by the piled weight and out-of-plane loads of wind. Since the insulation layer of the Sandwich panels has low strength and large deformation [3], the out-of-plane load of the wallboard is mainly sustained by the inner and outer panels [4, 5]. The wallboard is casted layer by layer, but its cowork performance is poor, and the overall load-carrying capacity is relatively weak. Therefore, a concealed rib Sandwich structure is proposed in this study.

Arubaye et al. [6] conducted double-shear tests on four different types of fiber-reinforced polymer (FRP) connectors and six-point bending tests on eight full-size concrete Sandwich plates and established an elastic analysis method for calculating the connectors, providing a method for predicting the cracking and deformation of Sandwich plates. Daniel Ronald Joseph et al. [7] conducted four-point bending tests on four concrete Sandwich plates, which were connected by steel strand mesh connectors. The test results showed that mesh connectors made a high contribution to the composition of the Sandwich plate, and the flexural

bearing capacity of the Sandwich plate was greatly related to the thickness of the plate. The bending capacity of the Sandwich plate was improved. Cox et al. [8] developed a star connector using needle glass fiber composite material (GFRP) and carried out pull-out, double-shear, and whole-plate bending tests on the composite plate. The test results indicated that the combination degree of the Sandwich plate was less than 6.5% only when the star connector was set at the end of the Sandwich plate, and the combination degree was improved by setting additional connectors. Scholars have performed a lot of research on precast concrete Sandwich plate connectors, and most of these works focus on rod or plate discrete connectors or continuous connectors made of FRP grids. Although the purpose of improving the bearing capacity has been achieved in these works, the complex constructions of the plates are not conducive to large-scale promotion.

For the innovative wallboard proposed in this study, the inner and outer panels are made of fiber-reinforced lightweight aggregate concrete, and the insulation layer is made of polystyrene particle concrete. Using the same cementitious material is convenient for the preparation of wallboards. At the same time, steel trusses are set up between the inner and outer panels to form concealed ribs as shown in Figure 1. The rib structure is beneficial to improve both the mechanical performance of precast composite wallboards and the cooperative performance of inner and outer panels.

This study is organized as follows: in section preparation of lightweight aggregate concrete, bearing capacity and good workability are based on the main control index of density, compressive strength, and slump. Taking density, softening coefficient, and strength as the main control indexes, the polystyrene granule concrete of lightweight, waterproof, compact, and nondeformable is prepared. Subsequently, the out-of-plane static loading test [9] and numerical simulation of the mechanical properties of the concealed ribbed Sandwich outer wallboard are carried out in section establishment of the finite element model. The cracking condition, deformation performance, and bearing capacity of the wallboard are studied to observe the cooperative working condition and two-failure mode of the inner and outer panels under the loads outside of the plane that are included in section theoretical analysis to provide an extent of reference for the engineering application of the concealed ribbed Sandwich outer wallboard.

2. Materials and Methods

2.1. Mix Design. Optimum mix for lightweight aggregate concrete, five variables, gelled material, water-binder ratio, absolute volume sand ratio, mineral admixture content, and fiber content were used as design parameters. Through the single factor analysis method, the influence of five design parameters on compressive strength, dry density of the lightweight aggregate concrete was studied. All design parameters affect the slump of the mixture. In this study, the slump of the mixture was controlled in a reasonable range (80–100 mm) by adjusting the dosage of the water-reducing agent.

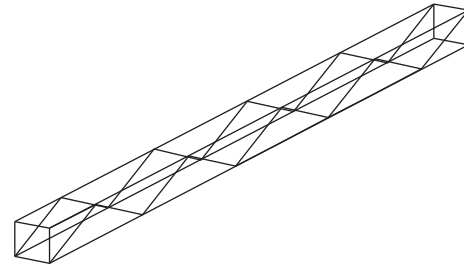


FIGURE 1: Schematic diagram of a concealed rib.

According to “The Technical Specification for Lightweight Aggregate Concrete (JGJ51-2002)” [10], the density grade of lightweight aggregate concrete prepared is $1,800 \text{ kg/m}^3$, the strength grade is LC30, and the slump is 80–100 mm.

Table 1 shows the optimal mixture ratio of lightweight aggregate concrete, with total cementitious material 460 kg, water-binder ratio 0.27, sand ratio 34%, fly ash 10%, slag 10%, and polypropylene fiber (PP fiber) content 0.05%.

Optimal mixture ratio of polystyrene granule concrete, the three variables of dispersible latex powder, hydroxypropyl methyl cellulose (HPMC), the gelled material, and the amount of lubricant are taken as the design parameters. The effects of three-design parameters on the viscosity, dry density, compressive strength, and softening coefficient of polystyrene granular concrete are studied by the single factor analysis. The optimal mixture ratio of polystyrene granular concrete is shown in Table 2 with water-binder ratio 0.5, PP fiber particle 30, gelled material 5.1 kg, fly ash 20%, zinc stearate 0.051 kg, redispersible latex powder 0.153 kg, and HPMC 3%.

2.2. Bendability Test of Precast Outer Wallboard. An out-of-plane static load test was carried out on the concealed rib Sandwich exterior wallboard [6] to study the influence of the thickness of the inner and outer panels, the setting of concealed ribs, the arrangement of concealed ribs on cracking and crack development, deformation performance, and bearing capacity of wallboard. The cooperative working condition and failure mode of the inner and outer panels under the exterior panel load were investigated. The results provide a reference for the engineering application of concealed ribbed Sandwich exterior wallboard.

2.3. Specimen Design and Manufacture. Considering the influence factors such as the thickness of inner and outer panels, whether the concealed rib is set or not and the way of arrangement, four groups of specimens were designed to carry out the static load test of the Sandwich wallboard under out-of-plane load.

The test simulation object is the prefabricated whole plate, that is, the height of the board is the height of the floor and the width of the plate is the size of the building space. Restricted by the test loading conditions, the specimen adopted the 1/2 scale, the size of the four test plates was $1600 \text{ mm} \times 1400 \text{ mm}$, and the total thickness of the wall plate was 130 mm. The inner and outer plates had an equal

TABLE 1: The optimal mixture ratio of lightweight aggregate concrete.

Cement (kg)	Slag: fly ash (%:%)	Slag (kg)	Fly ash (kg)	Sand (kg)	Ceramsite (kg)	Water (kg)	PP fiber (%)	Water reducing agent (%)	Sand ratio (%)	Binder (kg)	Water-binder ratio (%)	Slump (mm)
368	10:10	46	46	640	365	124	0.05	1.60	34	460	0.27	90

TABLE 2: Mixture ratio of polystyrene granule concrete.

Water-binder ratio	PP particle /L	Fly ash (kg/m ³)	Water (kg/m ³)	Cement (kg/m ³)	Zinc stearate (kg/m ³)	Redispersible latex powder (kg/m ³)	Gelled material (kg/m ³)	PP fiber (%)	HPMC (%)	Water-binder ratio (%)	Retarder (%)
0.5	30	1.02	2.55	4.08	0.051	0.153	5.1	0.05	3	1.5	0.05

thickness of 40, 50 mm, and the insulation layer had a thickness of 30, 50 mm.

The inner and outer panels of the wallboards were made of fiber-reinforced lightweight aggregate concrete, and the proportion is shown in Table 1. The insulation Sandwich layer was made of polystyrene granule concrete, and the mixture ratio of polystyrene granule concrete is shown in Table 2. The basic parameters of Slab 1~Slab 4 are shown in Table 3. The inner and outer panels were reinforced with steel mesh. In Slab 3 and Slab 4, the concealed ribs were welded with the steel mesh in the vertical and both in vertical and horizontal directions. The horizontal section of the test wallboard is shown in Figure 2.

The wallboards were placed in layers in the order of inner panels, insulation layers, and outer panels. The time interval of each layer was less than the initial setting time of concrete. The inner and outer panels of lightweight aggregate concrete and polystyrene particle insulation layer were made of the same cementitious material, and the bonding force between each layer of wallboards was better.

2.4. Test Loading Device and Scheme. The four sides of the prefabricated wallboard are flexibly connected with the frame beam and frame column. Under the load outside the surface, the frame beam and frame column can only be regarded as the support of the wallboard. To facilitate loading, the test pieces were laid flat, simply supported on four sides, and vertically loaded. Most of the outside panel loads, such as stacking load of prefabricated parts generated during transportation and installation and wind load during service, are uniform loads. In the test, the concentrated loading force was evenly distributed to the four loading points using a two-layer distribution beam, and the steel pads were also laid under the four loading points to simulate the plate loading [11]. The load testing device is shown in Figures 3 and 4.

The vertical displacement at the corresponding place of the top and bottom of the wallboards, the strain of reinforcement and concrete, and the occurrence and development of cracks were measured during the test. TAT3828E (signal test and analysis system) was used to collect electrical signals. The layout of the displacement meter, concrete strain

gauge, and reinforcement strain gauge are shown in Figures 5, 6 and 7.

A load-controlled monotonic loading protocol is used according to the "Standard for Test Methods of Concrete Structures" [12]. The load is loaded at 5 kN per level, and the load lasts for 5 minutes. When the load reaches about 70% of the ultimate load, the load level of each level is adjusted to 10 kN/level until the load reaches the ultimate bearing capacity of wall panel members. When one of the following three conditions occur (i.e., the steel bar at the bottom of the wallboard specimen yielding or breaking, the upper concrete of the wallboard specimen crushing in the compression zone, and the crack width of wallboard or deflection exceeding an allowable value), the wallboard is considered to reach the bearing capacity limit state and the loading test ends.

3. Results and Discussion

3.1. Experimental Phenomena and Failure Modes. Under the action of monotone loading, the stress process of the specimen can be divided into three stages: cracking stage, yield stage, and limit stage. Figure 8 shows the crack distribution at the bottom and top of the Slab 1-Slab 4 wallboard.

3.1.1. Cracking Stage. At the beginning of loading, the first crack appeared in the bottom span, but the overall stiffness was good. The increase in inner and outer panel thickness and the setting of concealed ribs were beneficial to increase the cracking load of wallboards. The deformation characteristics of specimens before cracking were similar.

3.1.2. Yield Stage. With the increase in load, transverse cracks appear along the edge of the wallboard. The bonding interface between the inner and outer panels and the middle insulation layer was torn, the insulation layer began to compress, the integrity of the test plate became poor, and the stiffness rapidly decreased. The top of the wallboard gradually developed into annular cracks, the cracks at the bottom of the plate began to extend, and the reinforcement under the loading point at the bottom of the plate gradually yielded. There was no significant difference in fracture

TABLE 3: Test board basic parameters.

Number	Thickness of each layer of wallboard Outer panel: insulation layer: inner panel/mm	Concealed rib arrangement	Reinforcement ratio of inner and outer panels (horizontal/vertical)
Slab 1	40 : 50 : 40	0	0.559%/0.534%
Slab 2	50 : 30 : 50	0	0.559%/0.534%
Slab 3	50 : 30 : 50	Vertical	0.559%/0.577%
Slab 4	50 : 30 : 50	Horizontal/vertical	0.559%/0.577%

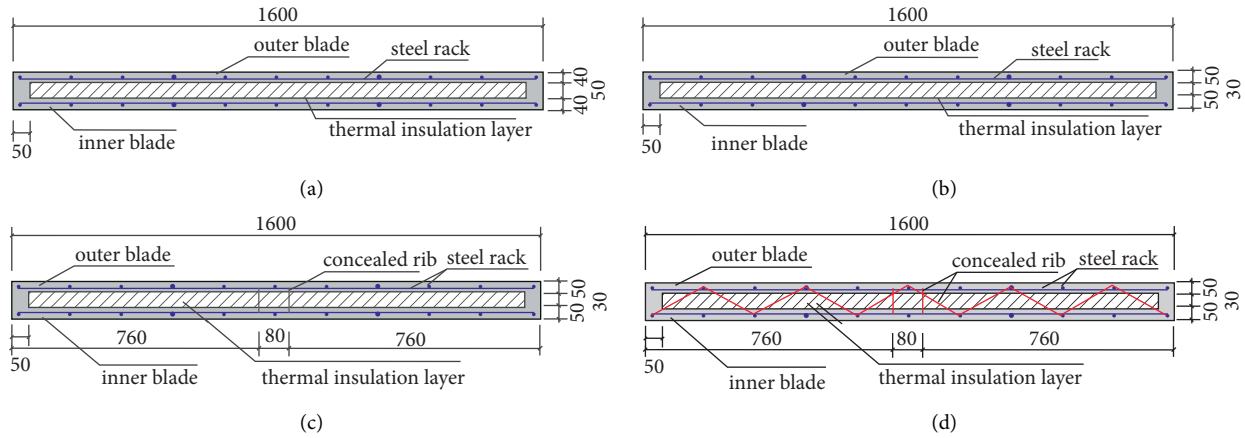


FIGURE 2: Horizontal section of wallboard: (a) Slab 1; (b) Slab 2; (c) Slab 3; (d) Slab 4.

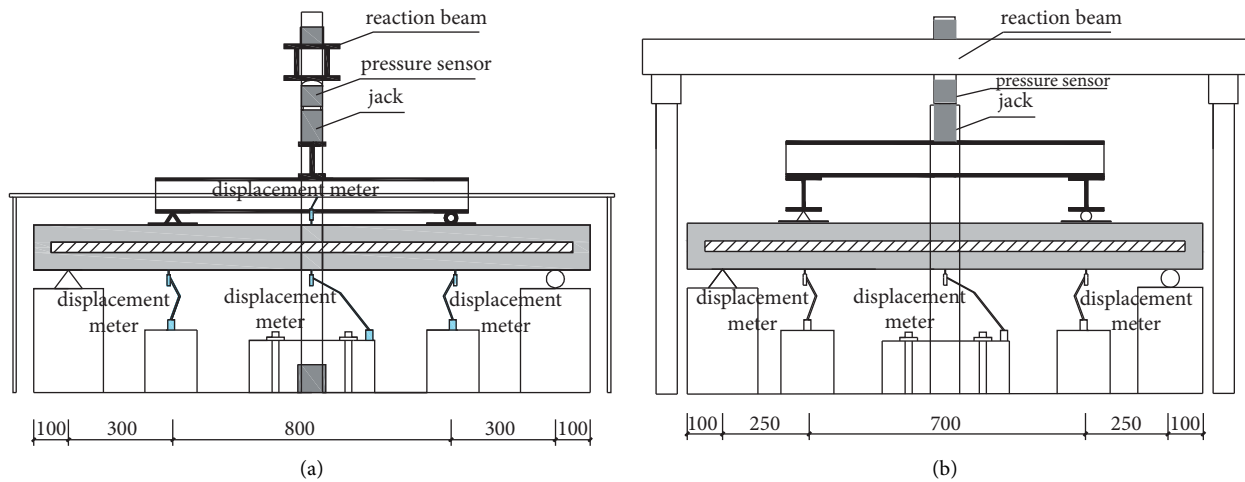


FIGURE 3: Schematic diagram of the test device: (a) the front view; (b) the side view.



FIGURE 4: Field diagram of test loading.

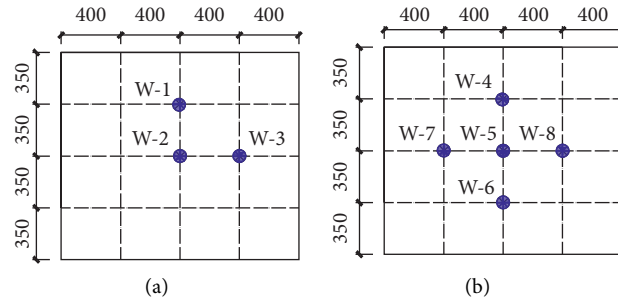


FIGURE 5: Layout of displacement meter: (a) top of the slab; (b) bottom of the slab.

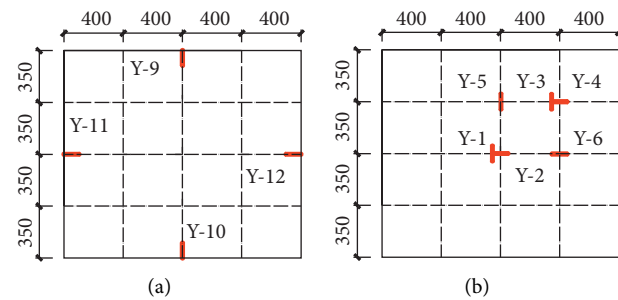


FIGURE 6: Layout of concrete strain gauge: (a) top of the slab; (b) bottom of the slab.

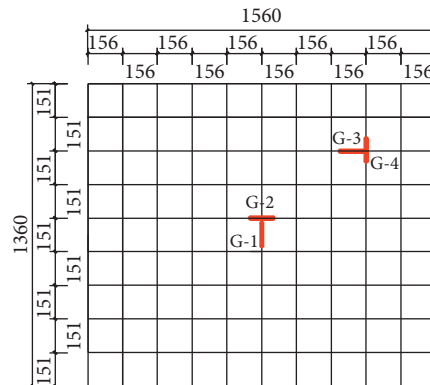


FIGURE 7: Layout of reinforcement strain gauge.

development between Slab 1 and Slab 2. In Slab 3, cracks along the concealed ribs appeared in the layout area of the wallboard top. The steel bar near the loading point at the bottom of the Slab 4 plate yield and the cracks at the bottom extended to the sides of the plate. The experimental phenomenon showed that the rib divided the wallboard into several continuous panels and improved the overall stiffness of the wallboard.

3.1.3. Limit Stage. As the load increased, the insulation layer was crushed, and the bottom cracks were fully developed. This formed radial cracks along with the four loading points, and oval circular cracks formed at the top of the wallboard. The four loading points on the top of Slab 1 finally lost their bearing capacity and cracked due to insufficient local pressure. Cracks of Slab 2 were fully developed, and the loss of bearing capacity was due to the yield of steel bars in the

bottom span. The ultimate load of Slab 3 increased, the cracks at the bottom of the wallboard fully vertically developed along with the specimen, and the cracks at the top of the plate appeared in a circular closed direction parallel to the concealed rib. The concealed rib divided the specimen into two one-way plates, but it was deformed by the vertical load and could only be used as weak support. In Slab 4, the vertical and horizontal concealed ribs transferred part of the load to the edge of the test plate. Cracks at the bottom of the plate were few, but the development form was similar to that of other plates. The loss of bearing capacity was due to the yield of steel bars at the bottom of the plate.

3.2. Load-Deflection Curve. The deflection characteristic values of the test plate are shown in Table 4. The mid-span load-deflection curve of the plate bottom span is shown in

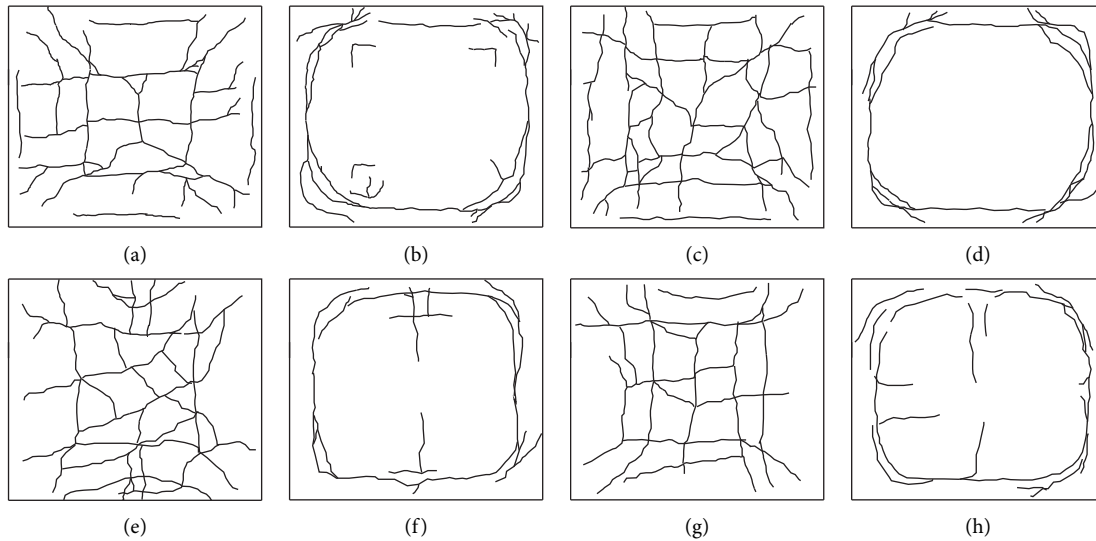


FIGURE 8: Cracks development diagram in the top of and at bottom of Slab 1–Slab 4: (a) bottom of Slab 1; (b) top of Slab 1; (c) bottom of Slab 2; (d) top of Slab 2; (e) bottom of Slab 3; (f) top of Slab 3; (g) bottom of Slab 4; (h) top of Slab 4.

TABLE 4: Eigenvalue of deflection of the specimen.

Number	Δcr (mm)	Δy (mm)	Δu (mm)
Slab 1	0.84	3.54	13.43
Slab 2	0.89	3.56	13.45
Slab 3	0.60	2.57	10.96
Slab 4	0.49	2.53	10.75

Note. Δcr is the cracking deflection, mm; Δy is the yield deflection, mm; Δu is the ultimate deflection, mm.

Figure 9. Figure 10 shows the comparison of top and bottom deflections of each wallboard at the same position.

Considering Table 4 and Figure 9, it can be seen that (1) the load-displacement curves of Slab 1 and Slab 2 before yield loading are similar in shape, and both show linear changes. The increase in the inner and outer panel thickness improves the stiffness of wallboards. When the yield load is reached, the wallboard's stiffness decreases, the increased rate of wallboard deflection exceeds that of the load, and the load slowly increases, but the increase in the inner and outer panel's thickness to the wallboard stiffness still takes place. (2) The overall stiffness of the wallboard of Slab 2 and Slab 3 is significantly improved by setting a concealed rib. After reaching the yield load, Slab 3 can still bear the slowly increasing load, and this indicates that the setting of the concealed rib can effectively improve the mechanical properties of the wallboard. (3) The load-displacement curve trend of Slab 3 and Slab 4 is equivalent before reaching the yield load. The increase in concealed ribs further improves the stiffness of wallboards, when the yield load is reached, and the slope of the Slab 4 curve very slowly declines, therefore indicating the addition of vertical and horizontal concealed ribs at the same time results in better mechanical performance of wallboards.

Figure 10 shows the load-deflection curves of the top and bottom of the test plate at the same position. It can be seen from the figure that when the load is small, the deflection of

the top and bottom of the plate is the same, and the inner and outer panels are subjected to the same stress and deformation. With the increase in load, due to the compression deformation of the core layer material, the deflection of the top of the plate gradually exceeds the bottom of the plate, and the deformation of the inner and outer panels is no longer consistent, which is also the reason for the cracks on the top of the plate. The results show that increasing the thickness of the inner and outer panels or arranging the concealed ribs can lead to inconsistent deformation between the top and bottom, increase the cracking load on the top of the plate, and improve the cooperative performance of the inner and outer panels.

3.3. *Characteristic Value of Bearing Capacity.* The characteristic values of the bearing capacity of the test plate are shown in Table 5.

Table 5 shows the following:

- (1) Cracking load: The increase in the inner and outer thickness of Slab 1 and Slab 2 can increase the cracking load by 58%, reaching 38 kN. Compared with Slab 2 and Slab 3, the cracking load can be increased by 39%, up to 53 kN. From Slab 3 and Slab 4, it is shown that the effect of setting the concealed ribs horizontally and vertically at the same time is better. If the concealed ribs are placed in one direction, the cracking load can be increased by another 15%, reaching 61 kN. With the increase in inner and outer panel thickness, the 8-effect section height of the wallboard participating in the bending work increases. The setting of concealed ribs is like adding trabecula in the plate, reducing the span of the plate and reducing the stress in the plate.
- (2) Yield load: In this experiment, a strain gauge is installed on the stress reinforcement in the plate to monitor the stress change. The plate load

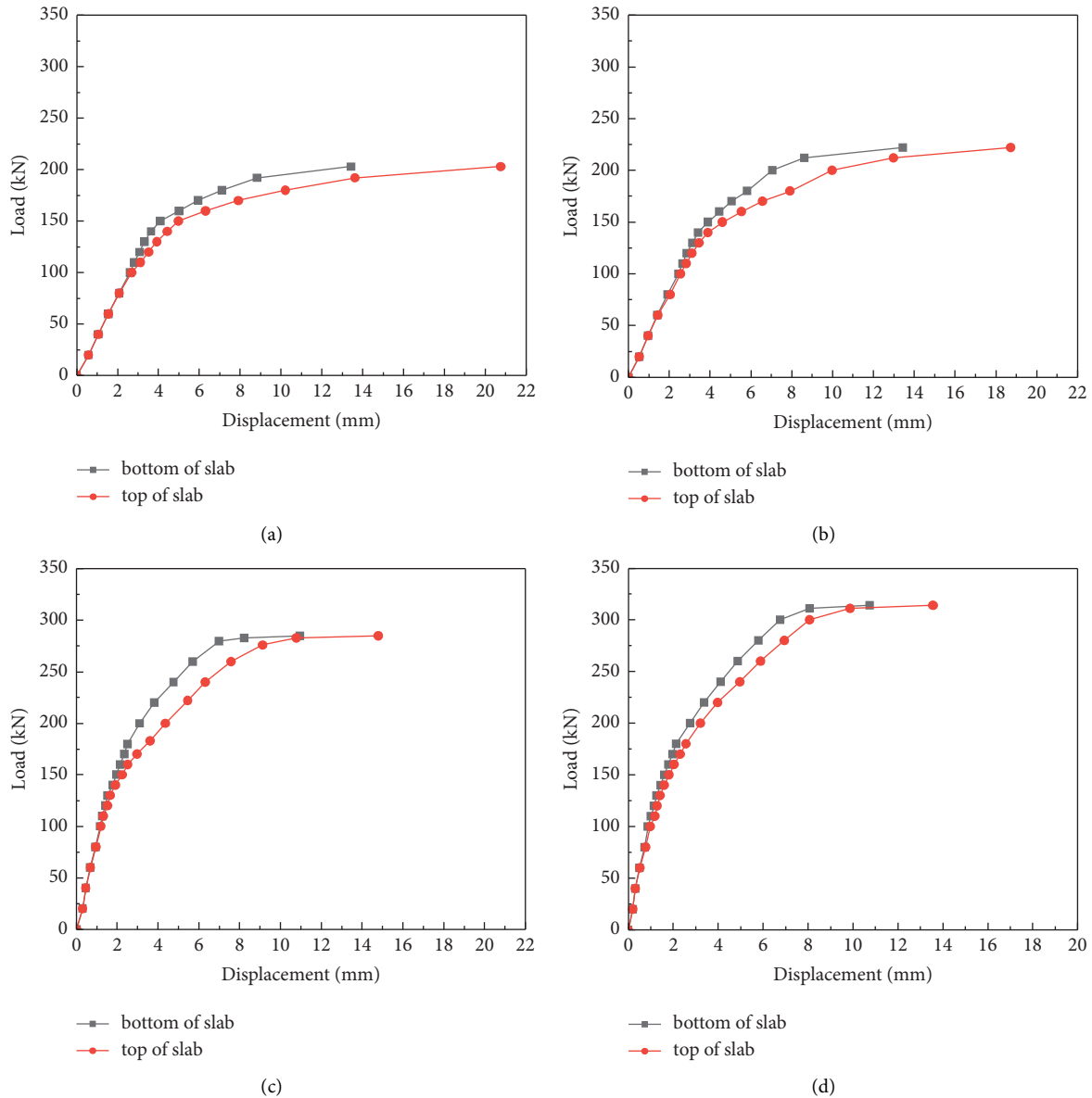


FIGURE 9: Load-deflection curves in the top and bottom of Slab 1-Slab 4: (a) Slab 1; (b) Slab 2; (c) Slab 3; (d) Slab 4.

corresponding to the stress reinforcement in the plate in the yield state is the yield load. The measured results of Slab 1 and Slab 2 show that the increase in inner and outer panels' thickness has little effect on yield load, only increasing by 4%, reaching 143 kN. Compared with Slab 2 and Slab 3, it is found that the setting of concealed rib causes the inner and outer panels to produce tension, restrict the mutual dislocation of the inner and outer panels, and can increase the yield load by 27%. Compared with Slab 3 and Slab 4, the setting concealed ribs in both vertical and horizontal directions in the middle of the wallboard can improve the yield load of the wallboard to a certain extent, but the effect is not significant, because it only increases by 10%.

(3) Ultimate load: Considering Slab 1 and Slab 2, the increase in inner and outer panels' thickness has little contribution to the ultimate bearing capacity, since it only increases by 10%. The Slab 3 test structure shows that the bearing capacity of the wallboard significantly increases after a concealed rib is installed, which is because the concealed rib forms a tie between the inner and outer panels of the wallboard, which effectively improves the cooperative performance of the inner and outer panels of the wallboard and improves the overall stiffness of the wallboard. In the loading process of Slab 1 and Slab 2 wallboards, when the load reaches 70% of the ultimate bearing capacity, the thermal insulation material of the core layer compresses and slips between the inner and outer panels. The interface between the inner

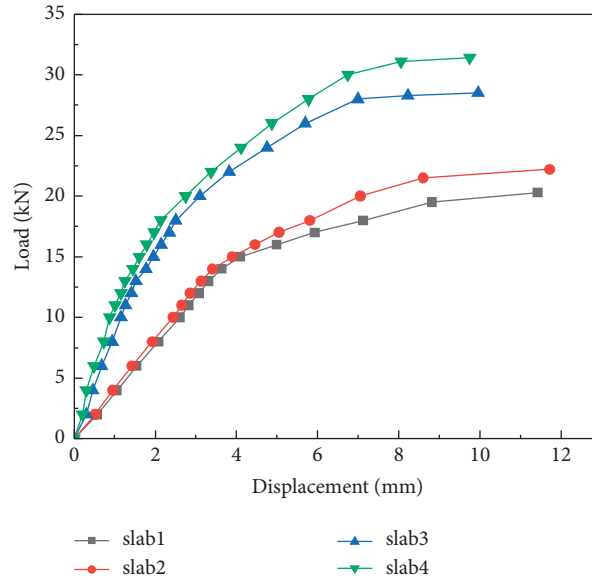


FIGURE 10: Load-deflection curves at the bottom of Slab 1–Slab 4 in the plate across.

TABLE 5: Characteristic value of bearing capacity of the test plate.

Number	F_{cr} (kN)	F_y (kN)	F_u (kN)
Slab 1	24	137	203
Slab 2	38	143	223
Slab 3	53	182	285
Slab 4	61	213	314

Note. F_{cr} is cracking load, kN; F_y is yield load, kN; F_u is the ultimate load, kN.

and outer panels and the thermal insulation layer of the core layer shifts, and the concealed rib can effectively contain the slip. When the load is more than 70% of the ultimate bearing capacity, this phenomenon was not present in Slab 3 and Slab 4 wallboards, and the bearing capacity of Slab 3 is 28% higher than that of Slab 2; however, a concealed rib is added and a plate stiffness of the out plane is improved. The wallboard channel bearing capacity increased by 10% when the concealed ribs are set in the vertical and horizontal direction, which is compared with that in one direction, and this is due to the fact that the concealed rib is like a trabecular, reducing panel plate across both inside and outside, makes the stress distribution more homogeneous in the plate, and improves the mechanical properties of plate, which indicates that concealed ribs could effectively improve the whole performance of the inner and outer panel and cause the wall stress more reasonable.

4. Numerical Simulation

Due to the limited test conditions, the numerical simulation of the flexural performance of prefabricated outer wallboards was carried out to provide a reliable numerical model for the later parameter analysis and further optimization of the plate shape.

4.1. Establishment of the Finite Element Model. ABAQUS finite element software was used to analyze the stress distribution and deformation of the composite wallboard under vertical load. During the modeling process, the concrete composite plate in Figure 11(a) and the steel grid frame and rigid gasket in Figure 11(b) were established, respectively. To simplify the finite element analysis, the bond-slip between the two types of concrete and reinforcement was ignored, and the reinforcement grid was set as a “built-in area” embedded into the whole. The two kinds of concrete and cushion blocks adopted the “C3D8R” type hexahedron element, and the reinforcement grid adopted the “B31” type linear beam element. The established finite element model is shown in Figure 11. The four ends of the finite element model of the composite plate are simply supported and were loaded on four points. To prevent stress concentration, four rigid plates were set on the four sides and four loading points of the composite plate, respectively, and the rigid plates were bound with the concrete surface by using the tie technology.

4.2. Finite Element Model Validation. The stress and deformation of the composite wallboard model after finite element solution are shown in Figure 12.

The top stress of the composite wallboard was distributed along with four loading points, the stress at the bottom of the loading point was the largest, the stress at the bottom of the plate was distributed along the four edges of the bottom of the plate, and the maximum stress was applied to the four edges of the test plate near the edge. The strain on the top of the plate corresponded to the stress, and the maximum strain was located around the four loading points. The strain at the bottom of the plate also formed a ring along the four edges of the plate.

It can be seen from Figure 12(a) that the strain at the circled part was large, which is consistent with the crushing of Slab 1 in the test. In Figure 12(c), the strain increased at

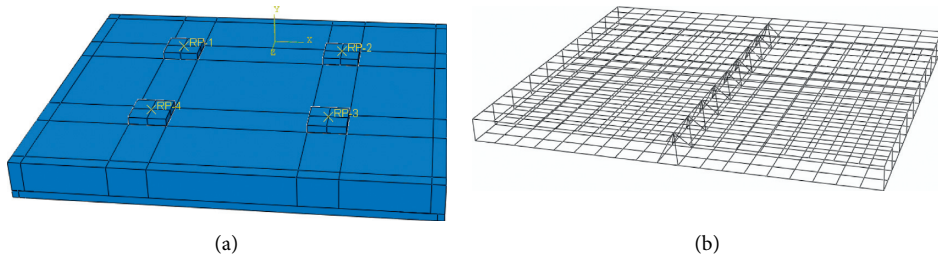


FIGURE 11: Finite element structural model: (a) concrete panel; (b) steel rack.

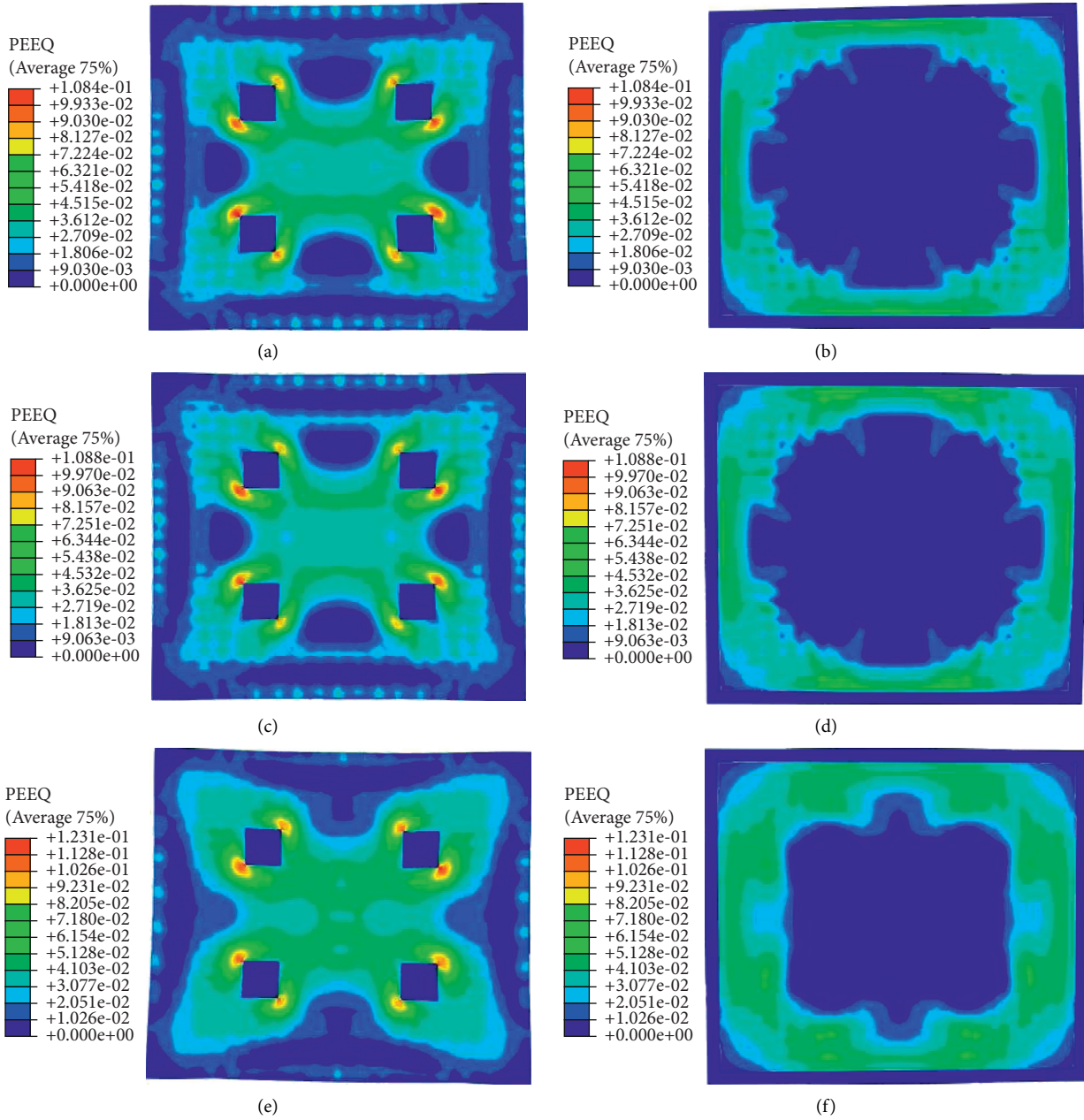


FIGURE 12: Continued.

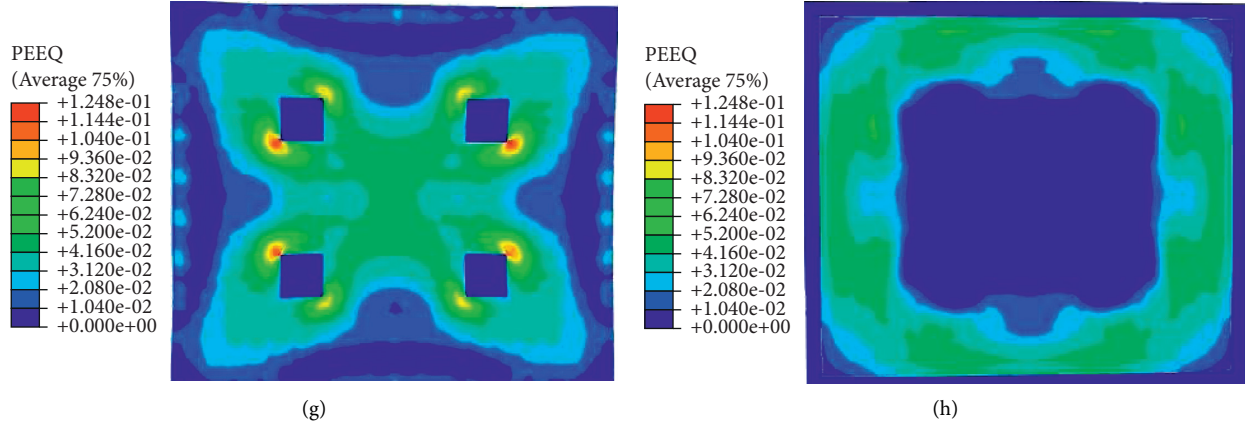


FIGURE 12: Deformation cloud diagram of Slab 1–Slab 4 structural model: (a) top of Slab 1; (b) bottom of Slab 1; (c) top of Slab 2; (d) bottom of Slab 2; (e) top of Slab 3; (f) bottom of Slab 3; (g) top of Slab 4; (h) bottom of Slab 4.

the scribing part, corresponding to the annular crack at the top of the Slab 2 in the test. According to Figures 12(e), the line part was the layout area of the concealed rib, and the strain sharply increased on both sides of this area, which corresponded to the vertical crack along the concealed rib at the top of Slab 3 plate in the test. According to Figure 12(f), the strain at the bottom of Slab 3 corresponded to the strain on the top of Slab 3 and was also affected by the vertical concealed rib. According to Figures 12(g) and 12(h), the strain on both sides of the Slab 4 layout area with concealed ribs sharply increased, and the strain on the top and bottom of the plate was affected by the concealed ribs, which is consistent with the experimental failure phenomenon.

Figure 13 shows the comparison between the load-deflection curves of the mid-span of the structural model and curves of test results. The ultimate load obtained by test and finite element analysis is shown in Table 6.

As seen in Figure 13 and Table 6, the slope of the load simulation value is slightly larger than the test value of the load-displacement curve; however, the variation trend of the two values is the same. Slab 1 has the largest load value difference, and the test load is 88.6% of the simulated load. Slab 2 has the smallest load difference, and the test load is 96.1% of the simulated load. This indicates that ABAQUS finite element model can simulate the bearing capacity and deformation performance of the composite plate in a better way, and has good reliability in design and application. Other working conditions of this type of wallboard can be simulated by using the finite element model, which provides a basis for the shape optimization design of the composite wallboard.

5. Theoretical Analysis

5.1. Cracking Load of the Composite Wallboard. Concrete can be regarded as an elastic material due to its positive ratio of stress to strain before the composite wallboard reaches cracking load. When calculating the cracking load of composite wallboard with uniform material, the equivalent section can be obtained by converting the reinforced section to the concrete sectional area. Equivalent converted sections

of composite wallboard before cracking are shown in Figures 14 and 15. When the cross-sectional area of bidirectional reinforcement is converted into concrete, an additional area is added at the upper and lower ends of concrete as $A_{sx'}$ and $A_{sy'}$, $A_{sx'} = A_{sx} \times n$, and $A_{sy'} = A_{sy} \times n$. Among them, A_{sx} represents the cross-sectional area of reinforcement in the X direction; A_{sy} represents the cross-sectional area of reinforcement in the y direction; $n = E_s/E_c$ represents the ratio of elastic modulus of reinforcement and concrete. The stress on the converted area of the reinforcement is equal to the strain force ($\epsilon_s E_s$) of concrete at the corresponding section height.

5.2. Advice on Equations. According to the literature [13], the bending stiffness reduction coefficients in x and y directions are as follows:

$$\lambda_x = 1 - \frac{3}{16} \times 3.14 \times \frac{(d/h)^3}{1 + (t_w/d)}, \quad (1)$$

$$\lambda_y = 1.036 - 0.784 \times \frac{(d/h)^3}{1 + 0.1333 \times (t_w/d)}.$$

Here, d is the height of the thermal insulation layer; t_w is the spacing of hollow circular tubes, because there is no round pipe in the composite plate, and the value here is 0.

According to the Code for Design of Concrete Structures [14], the formula for calculating cracking moment is as follows:

$$\begin{aligned} M_{crx} &= \gamma_m \lambda_x W_0 f_t^0, \\ M_{cry} &= \gamma_m \lambda_y W_0 f_t^0. \end{aligned} \quad (2)$$

Here, γ_m is the basic value of the influence coefficient of section resistance of concrete member; W_0 is the cross-sectional resistance moment. For a bidirectional hollow plate, the resistance moment of section in both directions is equal to the stiffness reduction factor in that direction multiplied by the resistance moment of section in the corresponding solid section; f_t^0 is tensile strength.

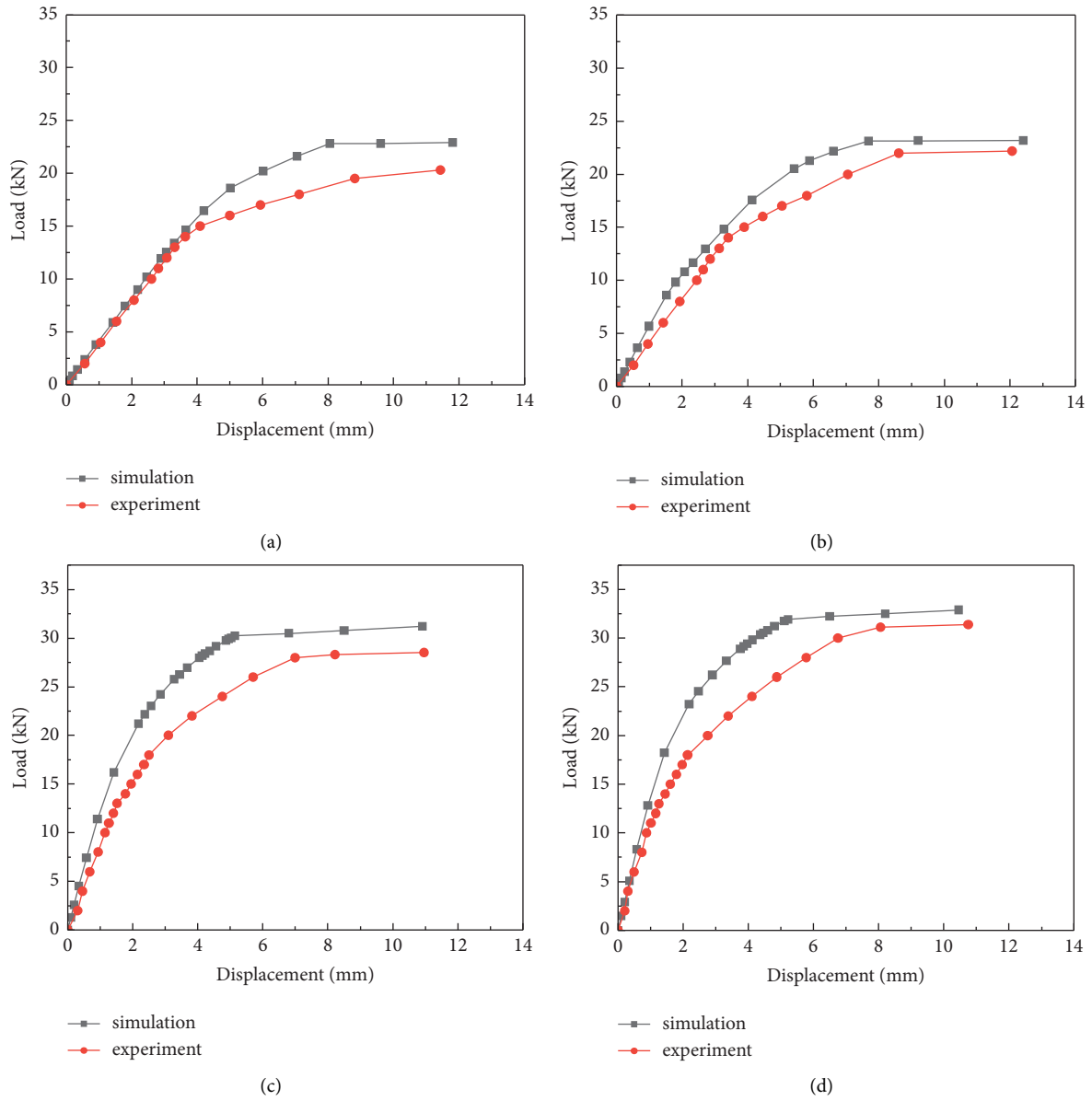


FIGURE 13: Comparison between simulated and experimental values: (a) Slab 1; (b) Slab 2; (c) Slab 3; (d) Slab 4.

TABLE 6: Comparison between simulated and experimental values of ultimate load.

Number	Simulated values (kN)	Experimental values (kN)	Error (%)
Slab 1	203	229	12.8
Slab 2	223	232	4.0
Slab 3	285	312	9.5
Slab 4	314	329	4.8
Average	—	—	7.8

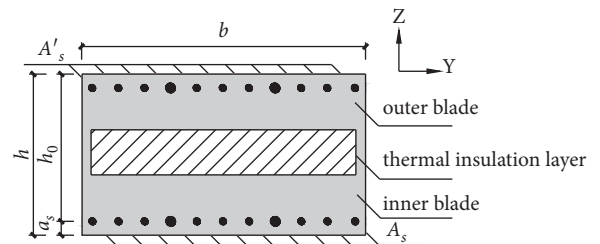


FIGURE 14: Schematic diagram of a normal section of the bidirectional plate.

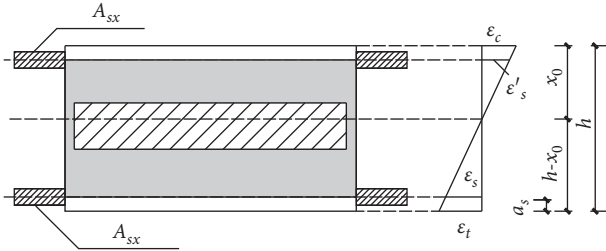


FIGURE 15: Equivalent converted section strain diagram.

The cracking load is as follows:

$$\begin{aligned} F_{\text{crx}} &= \frac{M_{\text{crx}}}{l}, \\ F_{\text{cry}} &= \frac{M_{\text{cry}}}{l}. \end{aligned} \quad (3)$$

The cracking load obtained from test and theoretical analysis is shown in Table 7.

It can be seen from Table 7 that the theoretically calculated value of the cracking load is generally close to the measured value of the test, with an average error of 12.8%, which can be used as the reference value in the test.

5.3. Composite Wallboard Bearing Capacity. The plastic stranding method is used to calculate the bearing capacity of four-side simply supported bidirectional dark ribbed composite wall slabs under uniform load. The longitudinal reinforcement direction span of the composite wallboard is l_x , the vertical longitudinal reinforcement direction span is l_y , and the included angle between the panel bottom oblique plastic hinge line and the long edge is θ . Reinforcement of the composite wallboard is equidistantly arranged, along the longitudinal reinforcement direction named x and vertical longitudinal reinforcement direction named y . The ultimate bending moment m_x and m_y within the width of the unit plate are as follows:

$$\begin{aligned} m_x &= A_{sx} f_{sx} \gamma_{sx} h_{0x}, \\ m_y &= A_{sy} f_{sy} \gamma_{sy} h_{0y}. \end{aligned} \quad (4)$$

Here, A_{sx} , A_{sy} , γ_{sx} , h_{0x} , and γ_{sy} , h_{0y} are the cross-sectional areas and internal couple arm of unit plate width in l_x and l_y directions, respectively. γ_{sx} and γ_{sy} are the coefficients of the internal moment arm and is usually taken as $\gamma_{sx} = \gamma_{sy} = 0.95$. f_{sx} and f_{sy} are the yield strength of the reinforcement in l_x and l_y directions, respectively.

According to the principle of virtual work, when the failure occurs under the action of the ultimate uniform load q , the virtual displacement at the midpoint of the plate is 1, and the virtual displacement at any point is $\omega(x, y)$. The work done by the exterior force (W_e) is equal to the work done by the internal force (the ultimate bending moment on the plastic hinge line) (W_i) [12, 15]. Then,

TABLE 7: Comparison of theoretical and experimental cracking load values.

Number	Calculated value (kN)	Experimental value (kN)	Error (%)
Slab 1	30	24	15.4
Slab 2	34	38	19.0
Slab 3	50	53	12.3
Slab 4	61	61	4.69
Average	—	—	12.8

$$\begin{aligned} W_e &= q \sum_n \int \int_{A_n} \omega(x, y) dA_n, \\ &= q \left[2 \times 2 \times \frac{1}{3} \times \frac{l_x}{2} \times sl_x + \frac{1}{2} \times l_x \times (l_y - 2sl_x) \right], \\ &= \frac{ql_x}{6} (3l_y - 2sl_x). \end{aligned} \quad (5)$$

Here, A_n ($n = 1, 2, 3, 4$) is the area of each plate divided by the plastic hinge line.

When calculating the internal force work, let $l_y = nl_x$ and $m_y = \alpha m_x$; therefore,

$$\begin{aligned} W_i &= - \sum m_i l_i \gamma_i, \\ &= - \left(l_y m_x \cdot \frac{4}{l_x} + l_x m_y \cdot \frac{2}{x} \right), \\ &= -2m_x (2n + \alpha/s). \end{aligned} \quad (6)$$

From $W_e + W_i = 0$, we can get the following:

$$q = \frac{2n + \alpha/s}{3n - 2s} \cdot \frac{12m_x}{l_x l_y}. \quad (7)$$

According to the plasticity theory, the solution obtained by equation (7) is the upper bound. Therefore, the bearing capacity of the bidirectional composite slab should be all the solutions of equation (7).

The minimum value of the derivative of variable S can be obtained as follows:

$$\begin{aligned} \frac{dq}{ds} &= \frac{(3n - 2s) - \alpha/s^2 + 2(2n + \alpha/s)}{(3n - s)^2} = 0, \\ s &= \frac{\alpha}{2n} \left(\sqrt{1 + \frac{3n^2}{\alpha}} - 1 \right), \end{aligned} \quad (8)$$

$$F = q \times A - G.$$

Here, G is the dead weight of the board.

The ultimate load obtained by theoretical analysis based on test and virtual work principle is shown in Table 8.

From Table 8, it can be seen that the theoretical calculated ultimate bearing capacity corresponds to the measured value in the test, with an average error of 6.6%. Therefore, it can be used as a reference value in the test.

TABLE 8: Comparison between theoretical and experimental values of ultimate load.

Number	Calculated value (kN)	Experimental value (kN)	Error (%)
Slab 1	230	203	13.3
Slab 2	231	223	3.6
Slab 3	282	285	1.0
Slab 4	288	314	8.3
Average	–	–	6.6

6. Conclusions

This study presents a type of precast concealed rib Sandwich outer wallboard. The wallboard is composed of lightweight aggregate concrete inner and outer panels, thermal core material, and concealed ribs between the inner and outer panels. The Sandwich structure of the wallboard allows it to have good thermal insulation performance. Meanwhile, the concealed ribs between the inner and outer panels effectively improve the mechanical performance of the wallboard. To fully optimize the Sandwich plate structure of the composite wallboard, the static load test, the finite element simulation, and the theoretical analysis are carried out. This is based on the inner and outer panel wall thickness and the arrangement of the concealed ribs on the Sandwich wallboard. Finally, the following conclusions are made:

- (1) Comprehensive consideration of compressive strength, dry density, and workability. The optimal mixture ratio of LC30 lightweight aggregate concrete with excellent performance is obtained through test verification. The optimal mixing ratio is as follows: total cementitious material 460 kg, water-binder ratio 0.27, sand ratio 34%, fly ash 10%, slag 10%, and polypropylene fiber content 0.05%.
- (2) By increasing the thickness of the inner and outer panels, the effective section of the wallboards participating in the bending work along the thickness direction is increased. Thus, the overall stiffness of the wallboards can be increased, which is conducive for improving the cracking load and ultimate bearing capacity of the wallboards, also improving the failure state of the wallboards.
- (3) By setting concealed ribs between the inner and outer panels of the wallboard, the effective tie can be established, the cooperative performance of the inner and outer panels can be improved, and the overall stiffness, cracking load, and bearing capacity of the wallboard can be improved. At the same time, the relative dislocation slip between the inner and outer panels caused by the compression deformation of the core layer insulation material can be effectively alleviated. It is better to arrange the concealed ribs in both directions.
- (4) The numerical model established can simulate the bearing capacity and deformation performance of the composite plate in a better way. The maximum value of bearing capacity obtained is close to the test

value, which has good reliability and provides technical support for further optimization of the plate shape.

- (5) The cracking load of composite wallboard calculated by the homogeneous elastic material method and the ultimate bearing capacity calculated by plastic stranding theory based on virtual work principle is close to the experimental value, which verifies the feasibility of this type of wallboard calculation method.

Data Availability

All data were obtained from own experiments. The test data are included in the article and can be made freely.

Conflicts of Interest

The authors declare that they have no conflicts of interest.

Acknowledgments

This research was supported by the Science and Technology Program of the Ministry of Housing and Urban-Rural Development, China (2020-K-114), the Construction System Science and Technology Project of Jiangsu, China (2018ZD096), and the Yangzhou Science and Technology Planning Project, China (YZ2020186).

References

- [1] S. Zambelli and B. Zambelli, "Prefabricated concrete panel for industrialized building with high thermal and/or acoustic insulation," *Journal of the Acoustical Society of America*, vol. 116, no. 1, p. 1874, 2000.
- [2] S. D. Zwanzig, *Numerical Simulation of Phase Change Material Composite Wallboard in a Multi-Layered Building Envelope*, University of Louisville, Kentucky, 2012.
- [3] N. Lakshmanan, S. Ganapathi Chitra, J. Annie Peter, and R. I. Nagesh, "Behavior of light weight sandwich panels under out of plane bending loading," *Steel and Composite Structures: International Journal*, vol. 21, no. 4, pp. 775–789, 2016.
- [4] P. L. N. Fernando, M. T. R. Jayasinghe, and C. Jayasinghe, "Structural feasibility of Expanded Polystyrene (EPS) based lightweight concrete sandwich wall panels," *Construction and Building Materials*, vol. 139, no. 15, pp. 45–51, 2017.
- [5] L. Byoung-Jun and S. Pessiki, "Design and analysis of precast, prestressed concrete, three - wythe sandwich wall panels," *PCI Journal*, vol. 52, no. 4, pp. 70–83, 2007.
- [6] S. Arubaye, T. Sorensen, J. Olsen, and M. Maguire, "Evaluating elastic behavior for partially composite precast concrete sandwich wall panels," *PCI Journal*, vol. 63, no. 5, pp. 71–88, 2018.
- [7] J. Daniel Ronald Joseph, J. Prabakar, and P. Alagusundaramoorthy, "Experimental study on the flexural behavior of insulated concrete sandwich panels with wires as shear connectors," *Alexandria Engineering Journal*, vol. 58, no. 3, 2019.
- [8] B. Cox, P. Syndergaard, S. Al-Rubaye, F. F. Pozo-Lora, R. Tawadrous, and M. Maguire, "Lumped GFRP star connector system for partial composite action in insulated precast

- concrete sandwich panels,” *Composite Structures*, vol. 229, Article ID 111465, 2019.
- [9] G. Carbonari, S. H. P. Cavalaro, M. M. Cansario, and A. Aguado, “Flexural behaviour of light-weight sandwich panels composed by concrete and EPS,” *Construction and Building Materials*, vol. 35, no. 5, pp. 792–799, 2012.
- [10] China Academy of Building Research, *Technical Specification For Lightweight Aggregate Concrete, JGJ51-2002*, China Standard Press, Beijing, China, 2002.
- [11] Standardization Administration of China, *Test Method for Building Wallboard, GB/T30100-2013*, China Standard Press, Beijing, China, 2013.
- [12] Ministry of Housing and Urban-Rural Development, PRC, *Standard Test Method for concrete Structures, GB/T50152-2012*, China Standard Press, Beijing, China, 2012.
- [13] X. Y. Han, S. G. Luan, and C. C. Wang, “Flexural stiffness analysis of cast-in-situ concrete hollow slab,” *Industrial architecture*, vol. 39, no. S1, pp. 365–368, 2009.
- [14] Ministry of Housing and Urban-Rural Development, PRC, *Code For Design of concrete Structures, GB50010-2010*, China Architecture and Building Press, Beijing, China, 2010.
- [15] F. B. Wu, L. B. Deng, and B. Liu, “Experimental study on concrete composite floor slab simply supported by four sides with unidirectional pre-stressed and bidirectional reinforcement,” *Building Structure*, vol. 44, no. 5, pp. 6–11, 2014.

Research Article

Field Tests' Study of Deviation Correction of Building near Excavation

Xi Peng ¹, Ningxin Yang ², and Mi Zhou ³

¹State Key Laboratory of Subtropical Building Science, South China University of Technology, 381 Wushan Road, Guangzhou 510640, China

²South China University of Technology, 381 Wushan Road, Guangzhou 510640, China

³State Key Laboratory of Subtropical Building Science, South China Institute of Geotechnical Engineering, South China University of Technology, 381 Wushan Road, Guangzhou 510640, China

Correspondence should be addressed to Mi Zhou; zhoumi@scut.edu.cn

Received 5 July 2021; Revised 13 August 2021; Accepted 22 August 2021; Published 8 September 2021

Academic Editor: Chiara Bedon

Copyright © 2021 Xi Peng et al. This is an open access article distributed under the Creative Commons Attribution License, which permits unrestricted use, distribution, and reproduction in any medium, provided the original work is properly cited.

Deviation correction of building is a big challenge for engineers. Without powerful technique for deviation, no special guidance can be followed to conduct the deviation rectification of buildings, which brings numerous failure cases. In this study, a case study was performed to provide insight into the behavior of a special technique for deviation rectification of building near excavation. The new technique was introduced firstly, and then, the field test data, in terms of lateral displacement of wall of pit, water level deviation, and soil deformation around pile of the building, were addressed to show the performance of the function of each process and the mechanism of it. The results show that this new technique for the deviation rectification of building works very well to uplift the whole building to reach the destination position (maximum uplift = 9.71 cm) and meets the requirement of design demand, without negative effect on the adjacent excavation reported.

1. Introduction

Excavated foundation pits are often close to buildings in urban areas, which make a big challenge for engineers to make the safety of surrounding buildings. The deformation of support structure and surrounding ground subsidence is directly due to dewatering of the foundation pit and then leads to differential settlements of the surrounding buildings. Li et al. [1] found that the maximum settlement around a foundation pit can be 30 mm in their studies. Moreover, the effective stress in soil increases by the lowering groundwater level for well-point dewatering around foundation pit, and the new settlement of surrounding buildings is caused. Numerous cases of buildings on soft foundation with large deformation of buildings were reported. Therefore, the differential settlements of building needed to be rectified. However, the rectification of buildings is a hard task because the plastic deformation of the building foundations is very difficult to recover.

At present, the study of rectifying building deviation mainly includes field tests and numerical simulations. Grouting technique has been widely used to uplift structures, which include grouting fluids into organic grouting fluids and inorganic grouting fluids (Miao et al. [2]). Some previous works have been conducted to utilize the uplift technique through three methods, including grouting, steel pipe pile traction, and Earth hollowing, to rectify the deviation of residential buildings and ancient temple (Jia et al. [3], Zhou et al. [4], Yin et al. [5], and Yin et al. [6]), with very effective performance obtained for these three methods. Grouting uplift has been proven that it cannot only be used in building deviation rectification but also can be applied in reducing differential settlements of railway subgrades and metro tunnel and uplifting of a subway foundation findings (Bian et al. [7], Zheng et al. [8], and Zhou et al. [9]). Numerical simulations were employed to explore the soil movement mechanisms in the deviation correction process, hence access the performance of the deviation technique.

Yin et al. [10] and Wang et al. [11] used the finite element simulation software to simulate the whole process of building deviation rectification, and they found that the FE method was effective, and the simulation results were relatively close to the measured results.

In this study, a case study of a special building deviation technique is conducted through field test monitoring, including groundwater level, horizontal displacement of adjacent soil and support structure, vertical soil displacement, and building relative tilt rate, to access the performance and mechanism of this new technique. It is found that this new technique has a significant effect on the deviation of buildings.

2. Site Condition

2.1. Project Profiles. This project is located in Guangzhou, south of China. The photo of this project is shown in Figure 1, which shows that the building is located in the southeast corner of the pit, at a distance of 12.9 m from the edge of the pit with a depth of 10.35 m. The foundation pit design adopts the support system of rotary bored pile and reinforced concrete, with partially usage of prestressed anchor cable. The water proofing design of the foundation pit uses triaxial cement mixing piles (large diameter) to form a water stopping curtain, which need to penetrate 2~4 m below the bottom of the pit. The layout of the excavation and building is shown in Figure 2. The process of the foundation pit construction contain five steps, including Step 1: locate the position of the foundation pit and mark it on-site; Step 2: construct the main structure piles, triaxial cement mixing piles, supporting piles, columns, and rotary spray piles; Step 3: construct the top beam of the foundation pit supporting piles and reinforced concrete internal support (partial anchor cable); Step 4: excavate the Earth to the bottom of the foundation pit and hang the net between the piles spray concrete protection; Step 5: construction of basement structure and replacement of bracing backfill. The building is a five-storey frame structure residential building, and its foundation is independent foundation, with its foundation size being 1.5 m × 2 m square individual foundation. The design requirement of the foundation bearing capacity is 150 kPa, and the building foundation buried depth is 1.5 m.

Concrete strength grade was tested by drilling cores and four sets of samples were taken, with the axial compressive strength of the concrete ranging from 14.5 MPa to 18.6 MPa. The axial compressive strength of the structural columns was tested by the rebound method, with the axial compressive strength ranging from 16.4 MPa to 20.2 MPa. The aggregate of concrete obtained from the core drilling was well distributed and densely cemented, but the steel reinforcement was corroded by slight rusting.

During the excavation of the foundation pit, the relative tilt rate of the building has been increased to beyond the requirement of the design code, with the relative tilt rate measured at the point s_{fd} in the northeast direction rapidly increasing to 2.296% and the settlement ranging from 58 to 81.3 mm. These large settlements were induced by the water level decrease that was induced by the pumping water during

the construction. Therefore, the large differential settlement of building makes it tilted, and deviation correction is needed.

The sectional drawing of the building is shown in Figure 3. The soil parameters of the soil samples and the parameters of the pit support structure are shown in Table 1. Soil profile around the tower base is divided into five layers according to the drilling depth (see Figure 3). The main bearing layer of the building foundation is soft-plastic silty clay and flow-plastic silt.

2.2. Instrumentation. In this project, the relative tilt rate of the building, the settlement of four corners of the building and the surface of adjacent soil, the deformation of the support structure of the foundation pit, and the horizontal displacement of adjacent soil were measured. Figure 4 shows the planar layout of the measuring points and lists the monitoring items and the corresponding instrumentation, where the triangle symbol denotes placement of the prism of total station, WT denotes the groundwater level measuring point, and LD denotes the embedding point of the inclinometer tube.

2.3. Rectification Process. Rectification involves drill recharge wells, drill slanting steel pipe, and grout mixture of cement slurry and water glass solution, add steel pipe piles, add raft, and carry out the construction of vertical steel pipe piles and grouting at the reserved orifice and the core of the steel pipe piles. Simply following previous results measured for this 5-storey reinforced concrete structure, such as the concrete strength grade and the bearing capacity of the main layer of foundation soil, the rectifying procedure should include six phases, as shown in Figure 5.

The first phase is to drill recharge wells on the ground between the building and the foundation pit. The wells should be filled with almost 200–300 cubic meter of water a day to allow the originally falling water table to rise back up and reduce the settlement of the building foundations. The second phase is to drill slant grouting steel pipes on the ground between the building and the foundation pit, as shown in Figure 3. Mixture of cement slurry and water glass solution should be grouted through the pipes into the foundation soil from the core of the steel pipe pile. Cement slurry water-cement ratio 0.4 to 0.5, water glass diluted at 1 : 2, grouting pressure more than 0.5 to 1.2 MPa, double slurry ratio about 1 : 1 to 1 : 0.8, solidification time control not more than 30 s, and single grouting volume (cement slurry) not the slurry is injected at intervals of 3 to 4 hours, depending on the deformation of the building, intermittently to reinforce the base subsoil. At the same time, in the vicinity of the large settlement, 4 deep grouting holes are designed in the steel pipe piles, and the soil is lifted by grouting the pile bottom with mixture of cement slurry and water glass solution, in order to realize the zonal lifting of the foundation. The third phase is to add vertical steel pipe piles to the foundation of the building to stand part of the vertical load. Mixture of cement slurry and water glass solution should be grouted at the bottom of the steel pipe piles to locally lift the

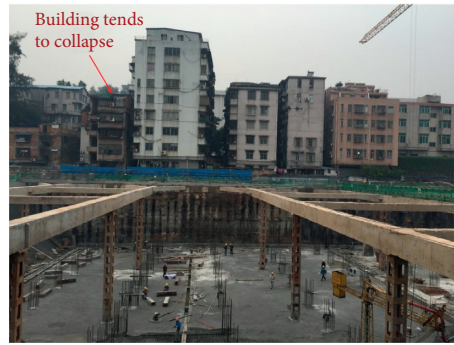


FIGURE 1: Project site photo.

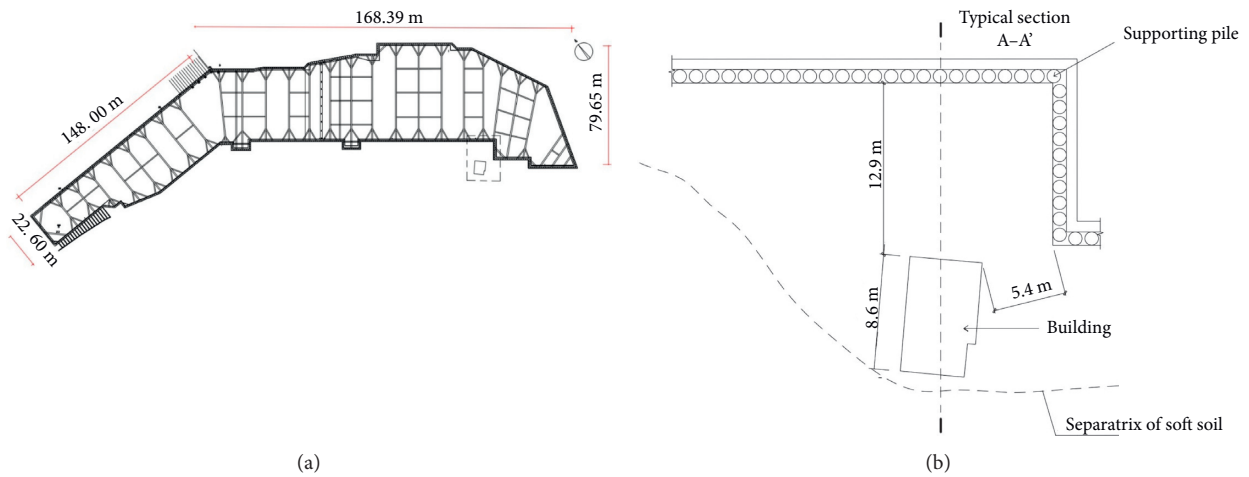


FIGURE 2: (a) Layout of the foundation pit. (b) Layout of the building.

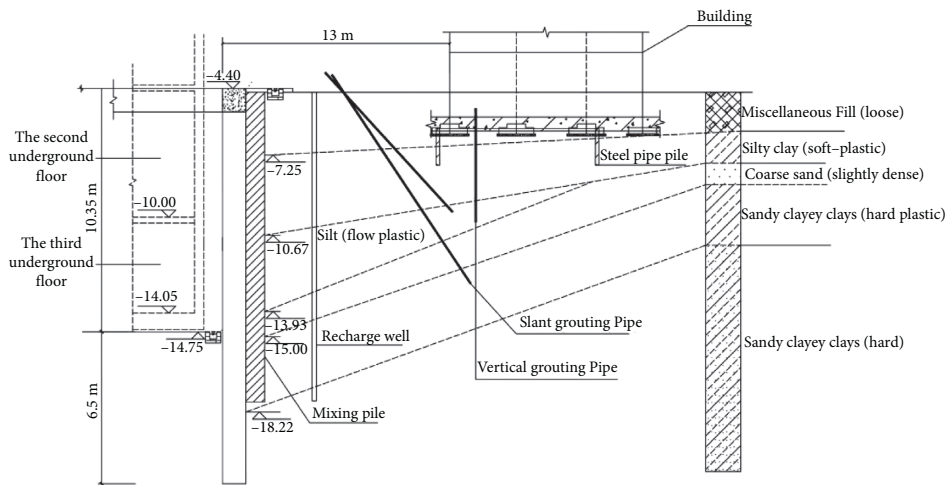


FIGURE 3: Typical section (A-A') drawing.

soil and prevent the collapse of the house. The fourth phase is to strengthen the building's foundation by using 600 mm raft slabs. In this phase, the individual foundations of the building are connected as a whole to furtherly increase the foundation stiffness and preventing the building from keeping settling during the correction process. The fifth

phase is the construction of vertical steel pipe piles with their design capacity being 150 (200) kN and their thickness being of 6 (8) mm. In this phase, piles are formed by means of static anchor pressure. The purpose of this step is to reduce the load on the foundation soil to further reduce the building settlement. The sixth phase is to gradually lift the foundation

TABLE 1: Soil properties and parameters.

Name	E (MPa)	γ (kN/m ³)	ν	c (kPa)	φ (°)	ω (%)	ω_L (%)	ω_p (%)	N	Thickness m	e	a_{1-2} (MPa ⁻¹)	E_s (MPa)
Miscellaneous fill	6	19.5	0.35	8	14	31.4	37.5	26.2	4.7	1.30~1.80	0.876	0.48	4.68
Silty clay	12	19.8	0.32	12	8	39.2	43.2	27.0	3.6	1.20~3.40	1.088	0.49	4.57
Silt	2	19.9	0.40	8	6	58.8	56.0	37.8	1.2	0.50~4.30	1.657	1.08	2.76
Coarse sand	25	20.1	0.28	0	30	8.1	—	—	7.5	0.50~2.40	0.867	0.12	11.42
Sandy clay ^①	150	20.5	0.25	40	33	29.7	37.2	25.3	16.4	1.20~10.00	0.892	0.46	4.26
Sandy clay ^②	180	20.9	0.23	60	35	25.0	34.4	22.0	25.9	0.90~7.90	0.778	0.36	5.10
Granite	300	22.5	0.22	100	38	—	—	—	—	—	—	—	—
Grouting area	50	19.9	0.32	30	28	—	—	—	—	—	—	—	—
Supporting pile	3.0×10^4	24	0.22	—	—	—	—	—	—	—	—	—	—
Horizontal support	3.0×10^4	24	0.22	—	—	—	—	—	—	—	—	—	—

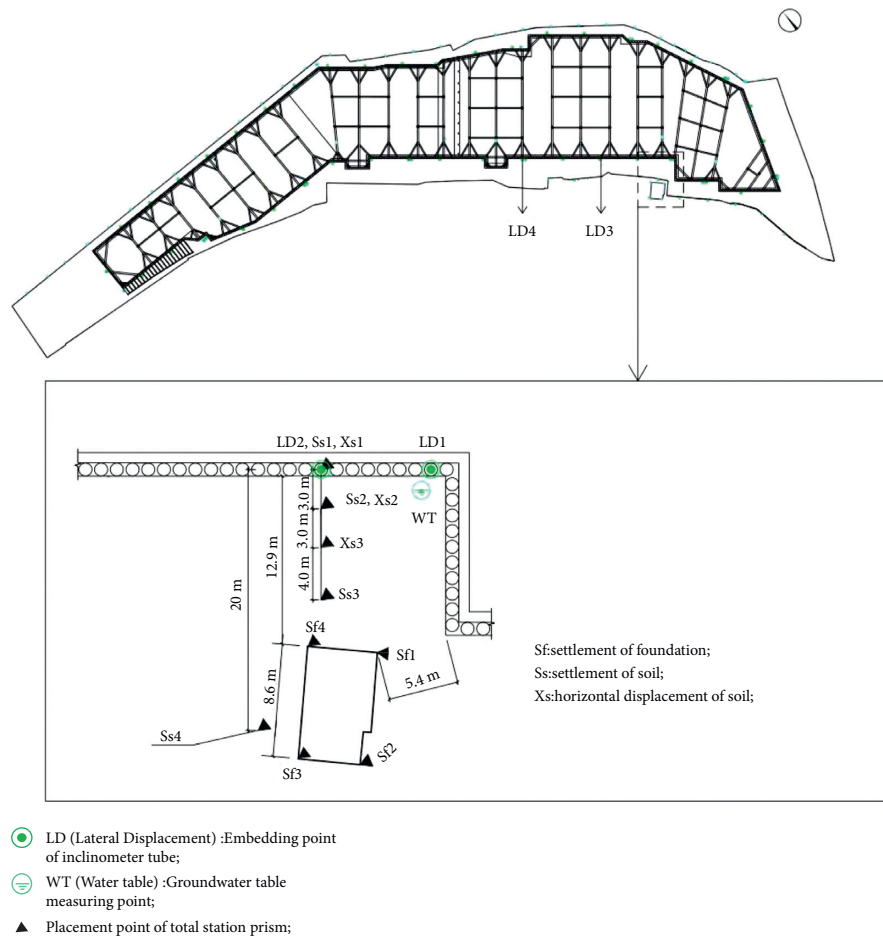


FIGURE 4: Site monitoring layout for rectification works.

soil. In this phase, the mixture of cement slurry and water glass solution should be grouted in small quantities and in sections at the reserved grouting apertures and the base of vertical steel pipe piles. Grouting can only be stopped when the building relative tilt rate is less than 0.8%.

3. Results and Discussion

3.1. The Relative Tilt Rate of the Building. The relative tilt rates of the building at the north-east and north-west were

measured by total station at s_{f1} point and s_{f4} are shown in Figure 6, from which it can be seen that the building was leaning before the pit was constructed. According to the statistic of two monitoring points, the relative tilt rates of the building before the first stage of building deviation rectification are 1.923% and 0.572%, respectively, at the point of s_{f4} in the northeast and northwest directions and 0.59% and 0.762%, respectively, at the point of s_{f4} in the northeast and northwest directions. It also shows that the relative tilt rates increase slowly before reaching the maximum settlement,

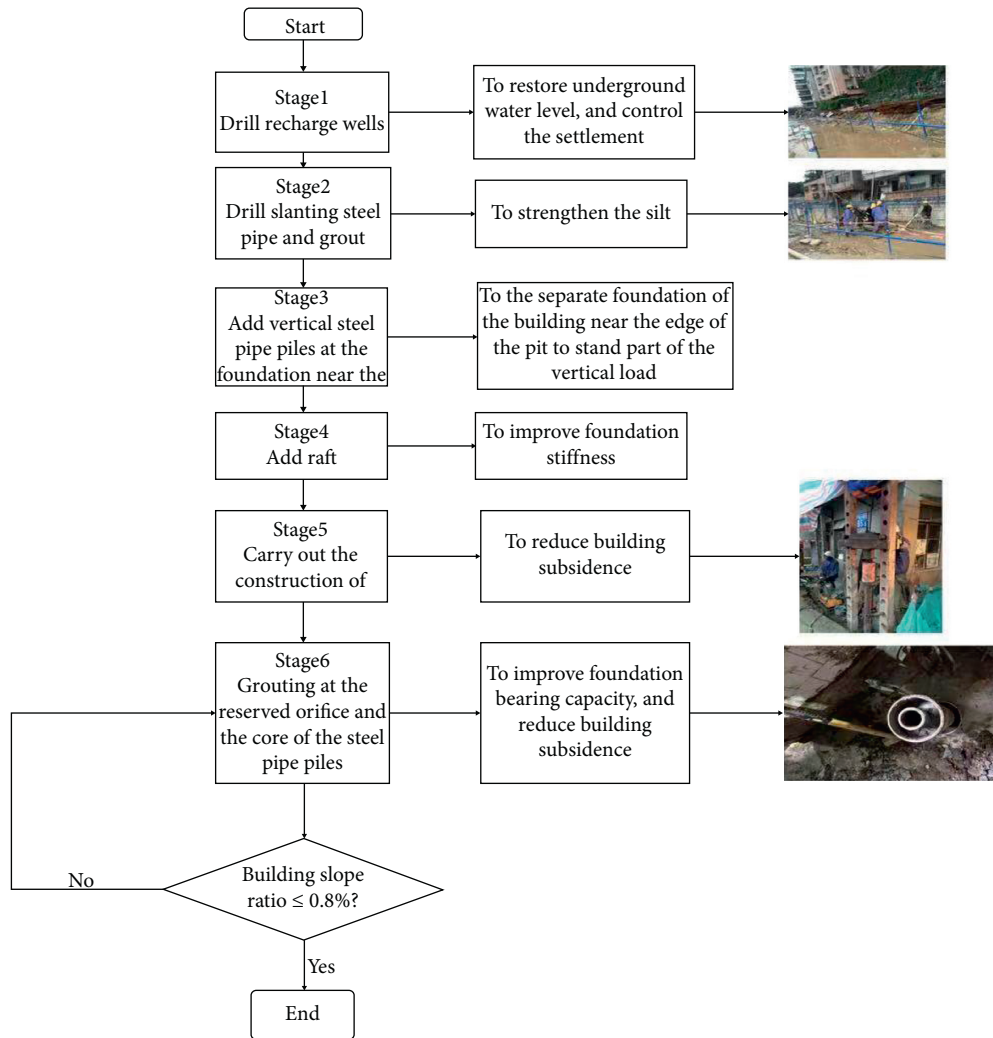


FIGURE 5: Working principal diagram of rectifying engineering.

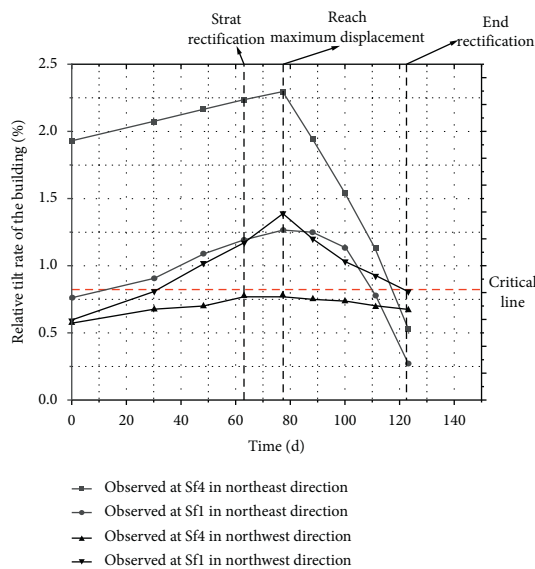


FIGURE 6: The tilt angle of the building in the whole process.

and after reaching the maximum settlement, the relative tilt rates decrease significantly due to the rise of the groundwater level, the support of the steel pipe piles, and the effect of grouting uplifts. After the building deviation rectification, the relative tilt rates at points of s_{f1} and s_{f4} in the NE and NW directions measured at the two points decreased to 0.27%, 0.81%, 0.53%, and 0.67%, respectively, both of which were less than the $\sim 0.8\%$ specified in the standard [12]. Zhou et al. [4] found, for a case on the grout lifting of the leaning pagoda of Dinglin Temple, that the leaning pagoda of Dinglin Temple was rectified, and its tilt angle was reduced from $7^{\circ}59'$ to $5^{\circ}36'$.

3.2. Variation of Water Level of Typical Water Level Holes.

The groundwater level in observation well decreases during the construction of the foundation pit. Figure 7 shows that the settlement of the pile head induced by the water level variation, which is decreased close to 10 m. Due to the sandy clay is under the support layer of the building, the

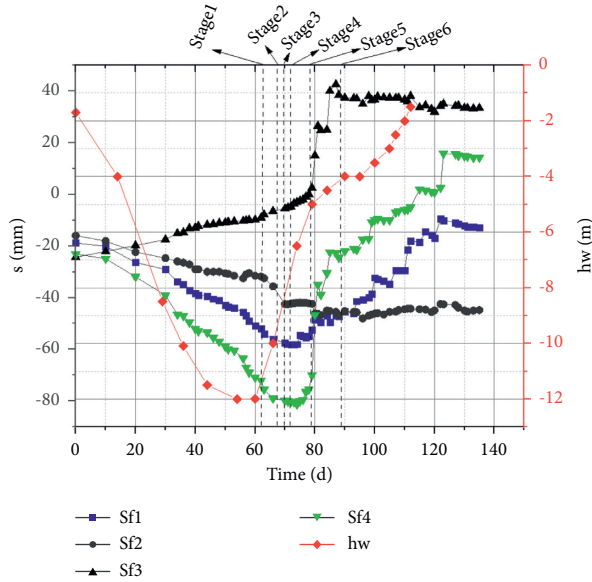


FIGURE 7: Surface settlement of four corners of the building.

permeability coefficient of the sandy clay is greater than that of the supporting layer. Because the water stop curtain only enters 3 m below the bottom of the pit, the groundwater has been bypassing the bottom of the water stop curtain to the foundation pit since the excavation of the foundation pit. Also, nearby residents have drilled and set up a water extraction well of about 40 m to continuously pump out groundwater, which has aggravated the fall of the groundwater level. Eventually, the groundwater level has fallen to a position close to the bottom of the pit.

After the rectification of the building began, the groundwater level began to rise gradually because 200–300 m³ of water was recharged into the recharge well daily, eventually returning to the position before the foundation pit was excavated. Li and Zheng [13] also found that the groundwater leakage occurred during the excavation of the pit due to problems with the water stop structure, but the water level drop was small, with only 3 m in their study of a foundation pit project.

3.3. Settlement of Four Corners of the Building. The settlement development of four corners of the building is shown in Figure 7. Before the construction of building deviation rectification, the monitored settlement curves can be divided into two types:

- (1) At points s_{f1} , s_{f3} , and s_{f4} , the settlement occurs. When the excavation is started, the settlement begins to develop at the monitoring points. The settlement velocity at the point s_{f4} is rapid, and the maximum settlement reaches 58.2 mm. The settlement velocity at the point s_{f2} is relatively slow, and the total settlement is only 10 mm.
- (2) The uplift occurs at point s_{f2} . When the excavation is started, the uplift begins to develop at the monitoring points. The maximum uplift value at point s_{f2} is 14.5 mm.

After the building deviation rectification was carried out, the curves at points s_{f1} , s_{f3} , and s_{f4} indicate that the uplift value of each monitoring point is proportional to time with the progress of the grouting process. The maximum uplift value at points s_{f1} , s_{f3} , and s_{f4} are 56.4 mm, 43.2 mm, and 97.1 mm, respectively. However, settlement still occurs at the point of s_{f2} in order to maintain the level of the whole building floor after the correction. Schweiger et al. [14] also used the grout lifting method when studying the correction of a steel oil tank that had undergone differential settlement, and the grouting points were arranged symmetrically with the center of the steel tank as the axis of symmetry. The measurement results of the field tests showed that the maximum lifting volume was nearly 170 mm (the total grouting volume was about 10,200 m³), so there is a clear difference in the grouting volume between this. Therefore, the maximum lifting volume of the two cases is different.

3.4. Settlement of Surrounding Soil. The settlement of the soil around foundation is shown in Figure 8. Before the construction of building deviation rectification, the monitored settlement curves are founded that the settlement occurs, and the settlements depend on the distance the points to the foundation pit. However, the reason of subsidence of these four points is different. The settlement of the top of the foundation support pile (s_{s1}) increased slowly because the Earth pressure acting on the support pile is increasing slowly as the excavation becomes deeper and deeper. The settlement at s_{s2} point kept increasing after the excavation of the pit because this point was for vehicles passing by and stacking next to the foundation pit. As for the points s_{s3} and s_{s4} , the settlement at s_{s3} and s_{s4} kept increasing because of the influence of the building subsidence.

After building deviation rectification was carried out, the curves at s_{s3} and s_{s4} indicate that the uplift value of each monitoring point is proportional to the time with the progress of the grouting process. However, the curves at s_{s1} and s_{s2} only stay stable because the distance between two points and grouting points is larger than 9 m. When the grouting is stopped, the surface uplift value will stabilize. The point s_{s3} was lifted by 75.3 mm, and the point s_{s4} was lifted by 14.6 mm. Ong et al. [15] found a similar phenomenon when observing soil movement induced by excavation in clay by the centrifuge model test. They found that, after completion of excavation, the soil continues to settle with time while the rate of increase in settlement decreases with time. Yang et al. [16] found that the settlement of the top of the supporting pile could reach a maximum of 6 mm when they studied the displacement of the supporting structure of a deep foundation pit using a pile anchor support structure. Guo et al. [17] summarized a formula for predicting the lift of the soil surface during slurry injection based on previous research and did field tests to compare the predicted and measured values. They found that the surface uplift at a location around 3 m from the grout center point was around 4 mm when the grouting depth was 8 m.

3.5. Horizontal Displacement of Surrounding Foundation Soil. The horizontal displacements of the soil around foundation are shown in Figure 9. It can be seen from Figure 9 that

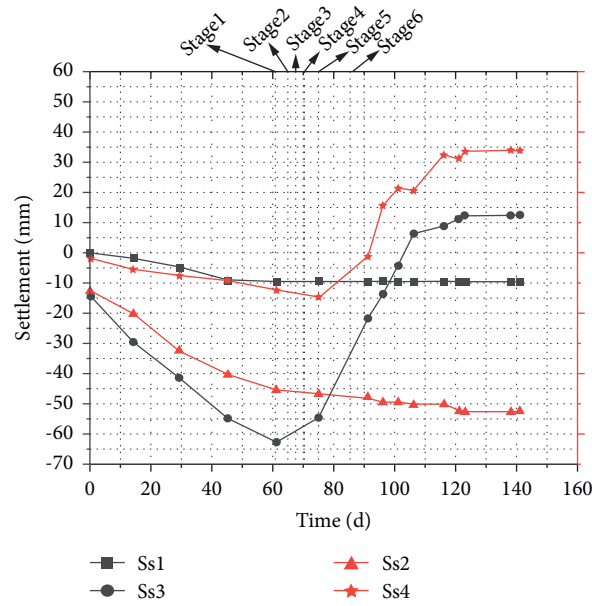


FIGURE 8: Settlement of the soil around foundation.

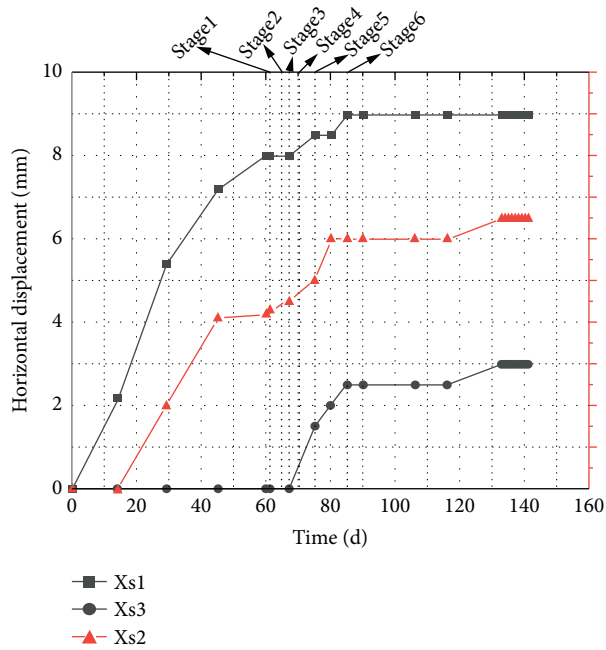


FIGURE 9: Horizontal displacements the soil around foundation.

horizontal displacements with construction are presented as a step-by-step process which are increased at first and then tended to stable. Horizontal displacements tend to increase with excavation, and the growth became slow after building deviation rectification was carried out and then finally tended to stable. The reasons for this phenomenon can be attributed to the increase in Earth pressure acting on the supporting pile and the pressure of trucks and stacks. The maximum horizontal displacement at the top of the supporting pile is 9.5 mm. The maximum horizontal displacements in the two points of x_{s2} and x_{s3} were 6.5 mm and

3 mm, respectively. Yang et al. [16] conducted tests to monitor the data of a foundation pit supported by a pile-anchor structure and excavated to a depth of 8–13 m in their study. It was found that the maximum horizontal displacement of the top of the supporting pile reached 16 mm. Zheng et al. [18] found that the radial stress decreases to 0 mm at distances greater than 1 m from the grouting point in their study on numerical modeling and verification of grouting with mold bag treatment on seepage failure in foundation excavation. From this finding, it can be concluded that the horizontal displacements at the two points

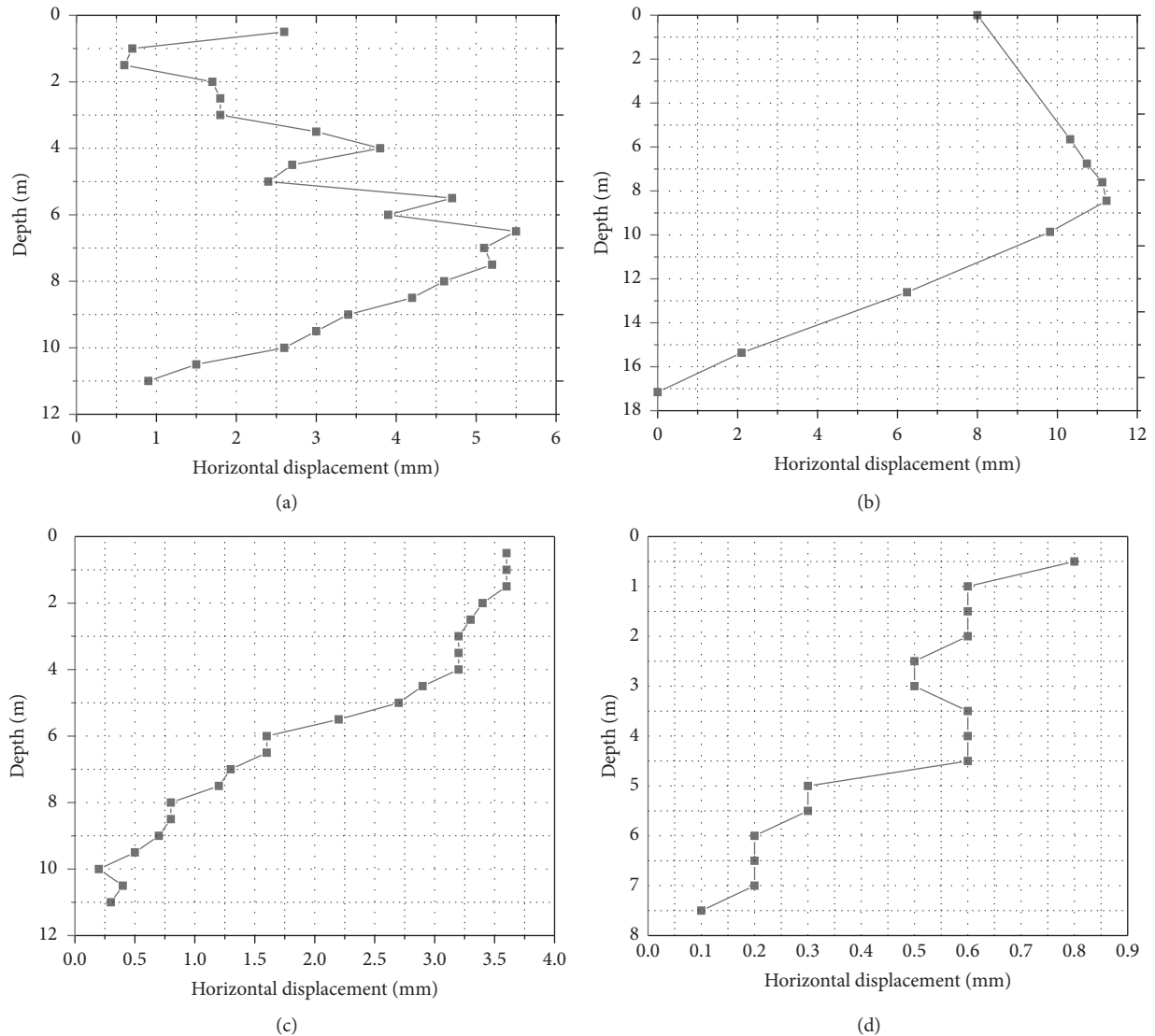


FIGURE 10: Horizontal displacements of wall of the excavation. (a) LD1. (b) LD2. (c) LD3. (d) LD4.

3 m and 6 m from the edge of the foundation excavation are not caused by grouting because their distance to the grouting point is much greater than 1 m.

3.6. Lateral Slope of Supporting Pile. The measured value of lateral slope of supporting pile at points LD1-4 is shown in Figure 10. The horizontal displacement of the supporting pile body has remained unchanged after the excavation of the foundation pit was completed because the Earth pressure acting on the supporting pile body has remained unchanged after the excavation of the foundation pit is completed. Also, the maximum deflection of the supporting pile was 12 mm, which was less than design requirement of 30 mm [19]. Tang et al. [20], Wang et al. [21], and Zhang [22] all measured the variation of the horizontal displacement of the supporting structure of foundation pit with depth due to the effect of Earth pressure in their own field tests or numerical simulations. The horizontal displacement at the midpoint of the

long side of the support structure from the excavation completion of the first layer to the completion of major structure has been increasing, but the curves of the horizontal displacement at the midpoint of the long side of the support structure were measured at each time point. Chong and Ong [23] also studied the deflection of contiguous bored pile wall affected by accidental groundwater drawdown. The largest horizontal wall deflection was 14.3 mm in the final stage of construction, which was similar to the data in this project.

4. Conclusions

Field tests were conducted to study the behavior of a special technique of deviation correction of building. Based on the tests data, some findings can be drawn as follows:

- (1) A new technique for the deviation rectification of building has been described in detail, and it works

very well to uplift the whole building to reach the destination position, which can meet the requirement of design demand.

- (2) The new technique can provide uplift step by step with the reinforcement of ground and can reach 9.71 cm displacement.
- (3) The new technique does not exaggerate deflection of the retaining structure of adjacent excavation, and the deflection of the retaining structure of adjacent excavation can meet the design requirement (maximum deflection = 14.3 mm < 30 mm).

Notations

E :	Elastic modulus
γ :	Weight density
ν :	Poisson ratio
c :	Cohesion force
φ :	Internal friction angle
ω :	Water content
ω_L :	Liquid limit
ω_p :	Plastic limit
N :	Standard penetration number
e :	Void ratio
a_{1-2} :	Compression coefficient
E_s :	Compressive modulus.

Data Availability

All data of the field tests in this study are available from the corresponding author upon request.

Conflicts of Interest

The authors declare that they have no conflicts of interest.

Acknowledgments

This research was supported by the Guangdong Basic and Applied Basic Research Foundation (2021A1515010828 and 2020A1515410001), State Key Laboratory of Hydraulic Engineering Simulation and Safety, and Tianjin University. These supports are appreciated.

References

- [1] Y. Li, Z. Z. He, G. H. Yan, and F. Y. Han, "Foundation pit dewatering and ground subsidence in binary structural stratum of Wuhan," *Advanced Materials Research*, vol. 639-640, pp. 694-699, 2013.
- [2] Q. Q. Miao, Q. Q. Zhu, and S. P. Jiang, "Application of grouting technology in the geotechnical engineering," *Applied Mechanics and Materials*, vol. 744-746, pp. 442-446, 2015.
- [3] G. Jia, "Research on the application of deviation correction technology in building reinforcement," in *Proceedings of the 3rd International Conference on Advances in Materials, Machinery, Electronics (AMME 2019)*, Wuhan, China, January 2019.
- [4] M. Zhou, X. Su, J. Lei, and S. Fang, "Foundation reinforcement and deviation rectification of the leaning pagoda of Dingling Temple, China," *Proceedings of the Institution of Civil Engineers-Geotechnical Engineering*, vol. 173, no. 6, pp. 473-484, 2020.
- [5] H. P. Yin, C. L. Li, and Z. Y. Xie, "Analysis on deviation rectification and reinforcement of buildings," *Advanced Materials Research*, vol. 255-260, pp. 59-64, 2011.
- [6] H. Yin, H. S. Qiu, and X. Q. Zhang, "Study and application of settlement resistance and correction method of a residential building," *Applied Mechanics and Materials*, vol. 621, pp. 89-94, 2014.
- [7] X. Bian, X. Duan, W. Li, and J. Jiang, "Track settlement restoration of ballastless high-speed railway using polyurethane grouting: full-scale model testing," *Transportation Geotechnics*, vol. 26, Article ID 100381, 2021.
- [8] Z. Zheng, R. Liu, S. Li, and H. Yang, "Control of ground uplift based on flow-field regularity during grouting in fracture with flowing groundwater," *International Journal of Geomechanics*, vol. 20, no. 3, Article ID 04020014, 2020.
- [9] S. Zhou, J. Xiao, H. Di, and Y. Zhu, "Differential settlement remediation for new shield metro tunnel in soft soils using corrective grouting method: case study," *Canadian Geotechnical Journal*, vol. 55, no. 12, pp. 1877-1887, 2018.
- [10] H. Yin, L. Chunlin, and X. Zhongyou, "Finite element simulation of building deviation rectification through excavation," in *Proceedings of the 2011 International Conference on Electric Information and Control Engineering*, pp. 5043-5046, Wuhan, China, April 2011.
- [11] Y. Wang, X. H. Wang, and M. Zhang, "Research on mechanisms and ground uplifting effects by grouting taken the grouting-soil-building interaction into account," *Trans Tech Publications*, vol. 163, pp. 3488-3498, 2011.
- [12] China Architecture & Building Press, *GB 50007-2011, Code for Design of Building Foundation*, China Architecture & Building Press, Beijing, China, 2015, <https://www.chinesestandard.net/>.
- [13] X. Li and Y. Zheng, "Monitoring and analysis of soft foundation pit with braced structure of bored cast-in-place pile," in *Proceedings of the 2011 International Conference on Electrical and Control Engineering*, pp. 5342-5345, Yichang, China, September 2011.
- [14] H. F. Schweiger, C. Kummerer, R. Otterbein, and E. Falk, "Numerical modelling of settlement compensation by means of fracture grouting," *Soils and Foundations*, vol. 44, no. 1, pp. 71-86, 2004.
- [15] D. E. Ong, C. E. Leung, and Y. K. Chow, "Pile behavior due to excavation-induced soil movement in clay. i: stable wall," *Journal of Geotechnical and Geoenvironmental Engineering*, vol. 132, no. 1, pp. 36-44, 2006.
- [16] X. H. Yang, F. W. Wu, T. Chen, and X. Liu, "Analysis of monitoring results of a deep foundation pit with pile-anchor retaining structure," *Applied Mechanics and Materials*, vol. 580-583, pp. 28-33, 2014.
- [17] F.-Q. Guo, X.-T. Liu, W.-Q. Tong, and Z. Shan, "Prediction of ground surface displacement caused by grouting," *Journal of Central South University*, vol. 22, no. 9, pp. 3564-3570, 2015.
- [18] Z. Zheng, R. Liu, S. Li, and Q. Zhang, "Numerical modeling and verification of grouting with mold bag treatment on seepage failure in foundation excavation," *Geomatics, Natural Hazards and Risk*, vol. 9, no. 1, pp. 1172-1185, 2018.
- [19] China Architecture & Building Press, *JGJ 120-2012, Technical Specification for Retaining and Protection of Building Foundation Excavations*, China Architecture & Building Press, Beijing, China, 2012, <https://www.chinesestandard.net/>.
- [20] Y.-Q. Tang, J.-J. Yan, Z.-J. Sun, and J. Zhou, "Measurement analysis of bohai bank deep foundation pit project in tianjin

- soft soil area,” *Engineering Geology for Society and Territory–Volume 4*, Springer, Berlin, Germany, pp. 17–24, 2014.
- [21] G. X. Wang, X. L. Sun, and W. P. Zhao, “Influence of excavation of complex foundation pit on surrounding environment,” *IOP Conference Series: Materials Science and Engineering*, IOP Publishing, vol. 423, Article ID 012022, 2018.
- [22] Q. Zhang, “Deformation analysis of deep foundation pit excavation in China under time-space effect,” *Geotechnical Research*, vol. 7, no. 3, pp. 146–152, 2020.
- [23] E. E.-M. Chong and D. E.-L. Ong, “Data-driven field observational method of a contiguous bored pile wall system affected by accidental groundwater drawdown,” *Geosciences*, vol. 10, no. 7, p. 268, 2020.

Research Article

Numerical Study on the Behavior of Square Stiffened Caissons Penetrating into Normally Consolidated Clay

Wei Liu ¹, Zhihuai Huang ², and Mi Zhou ³

¹Guangzhou Urban Planning & Design Survey Research Institute, Guangdong Enterprise Key Laboratory for Urban Sensing, Monitoring and Early Warning, Guangzhou 510060, China

²Key Laboratory of the Pearl River Estuary Regulation and Protection of Ministry of Water Resources, Pearl River Water Resources Research Institute, 80 Tianshou Rd., Guangzhou 510611, China

³School of Civil and Transportation Engineering, South China University of Technology, 381 Wushan Road, Guangzhou 510640, China

Correspondence should be addressed to Mi Zhou; zhoumi@scut.edu.cn

Received 5 July 2021; Accepted 13 August 2021; Published 31 August 2021

Academic Editor: Xihong Zhang

Copyright © 2021 Wei Liu et al. This is an open access article distributed under the Creative Commons Attribution License, which permits unrestricted use, distribution, and reproduction in any medium, provided the original work is properly cited.

Significant difference between predicted and measured installation resistance of stiffened suction caissons was identified due to the existing uncertainty regarding the mobilized soil flow mechanisms. This paper describes an extensive investigation of square stiffened caisson penetration in nonhomogeneous clays undertaken through large deformation FE (LDFE) analysis to identify the soil flow mechanisms around and between lateral ring stiffeners. A detailed parametric study has been carried out, exploring a range of nondimensional parameters related to stiffened caisson geometry, caisson roughness, and soil strength. The LDFE results were compared with centrifuge test data in terms of soil flow mechanisms, with good agreement obtained. Two interesting features of soil flow inside the caisson were observed including soil backflow into the gaps between the embedded stiffeners and soil heaving at the surface. It shows that the cavity depth can reach ~5 m. Finally, simple expressions were proposed for estimating the critical depths of soil backflow and cavity formation.

1. Introduction

To avoid the buckling failure of the thin wall of a long caisson during installation, the skirt is strengthened with internal stiffeners, horizontal rings, and/or vertical flanges (see Figure 1), together with local thickening of the wall in the vicinity of the loading point. The addition of these stiffeners has created significant uncertainties regarding the soil flow mechanisms, side friction, and end bearing and consequently in the prediction of underpressure required for installation [1].

The uncertainties have been shown by the significant differences observed between the predicted caisson resistance, based on the presumed soil flow mechanisms (see Figure 2), and the measured resistance in the field. The field measurements include the stiffened caisson installation at the Laminaria field in the Timor Sea and at the Girassol field,

offshore West Africa [2–4], with a detailed discussion reported by Hossain et al. [5]. Andersen et al. [1] discussed the predictions for two different hypothetical installation cases and six case histories of caissons with stiffeners carried out by four predictors using their normal design method. The predictors produced significantly different results largely due to the assumption of different soil flow mechanisms around and between the stiffeners [1].

Large deformation FE analyses and centrifuge model tests on unstiffened caisson installation were carried out by Andersen et al. [6], Zhou and Randolph [7], Chen and Randolph [8], and Westgate et al. [9], among others. They noticed no discernible difference in the axial capacity between jacked and suction-installed caisson, except Zhou and Randolph [7]. Significant proportion of soil flow was reported to occur inward into the caisson, with little outward flow.



FIGURE 1: Photo of square stiffened caisson.

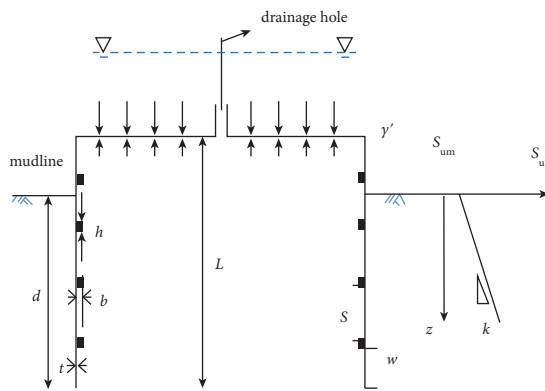


FIGURE 2: Geometry of square stiffened caisson.

This paper reports the results from an extensive investigation carried out through large deformation FE (LDFE) analysis in an attempt to provide insight into the failure mechanism of square stiffened caisson penetration in nonhomogeneous clays. Expressions are developed to estimate the critical depths of soil backflow into the gaps between the embedded stiffeners.

2. Large Deformation Finite Element Analysis

2.1. The RITSS Method. Randolph and Hu proposed a finite element method with small strain calculation based on the remeshing technique for large deformation of solid in 1998. This large deformation finite element method belongs to the arbitrary Lagrangian-Eulerian (ALE) finite element methods can be employed coupling with ABAQUS and AFNEA. This method includes the following main steps: (i) generate an initial mesh consisting of six-node triangular elements with three internal Gauss points; (ii) use the program to perform an specified increment of small strain analysis; (iii) regenerate and optimize the mesh to generate new units and nodes; (iv) interpolate the material stress and properties; and (v) check whether the displacement meets the requirements;

if not, open a new finite element small deformation project and repeat the above steps until it can meet the requirements; then, close the project. The RITSS method has the significant advantage that the mesh will be constantly updated to ensure accuracy and quality, making the calculation process smooth when the project is running.

2.2. Numerical Model and Parameter Setup. A square stiffened caisson penetrating into normally consolidated clay with shear strength of $S_u = S_{um} + kz$ was analyzed in this study, with geometry of square stiffened caisson shown in Figure 2. The friction coefficient of structure-soil interfaces is α ; therefore, the limiting shear force along the interface of structure and soil is αS_u . All the floating bulk densities of the clay are set as $\gamma' = 6 \text{ kN/m}^3$.

Because the width of squared caisson is significantly larger than the sum of the width of stiffener and thickness of skirt, the plane strain model was used to simulate the failure mechanism behavior of the squared caisson piling process. In order to prevent the boundary effects, the model was arranged in the middle of the computational mesh, and the length and width of the plane strain model were set to be $5L$. Hinge constraints were applied along the base, while roller constraints were set at the vertical sides of the soil model. The six-node triangular mesh with three internal Gauss points was employed in this study, and nodal joint elements were used to simulate the interaction of structure and soil, where the limiting shear force is $\alpha S_u \cdot A$. The initial finite element mesh of the numerical model is shown in Figure 3(a). The initial penetration depth is 0.02 m. The calculation parameters selected are shown in Table 1.

In this study, the Mohr-Coulomb constitutive model is used to simulate the clay with very low permeability, and the Tresca yield criterion is also used. Poisson's ratio $\nu = 0.49$, friction and dilation angles $\phi = \psi = 0$, and a uniform stiffness ratio $E/s_u = 500$ which is a common value for clay, where E is Young's modulus. The normally consolidated clay with undrained shear strength of $S_u = S_{um} + kz$ (S_{um} is the shear

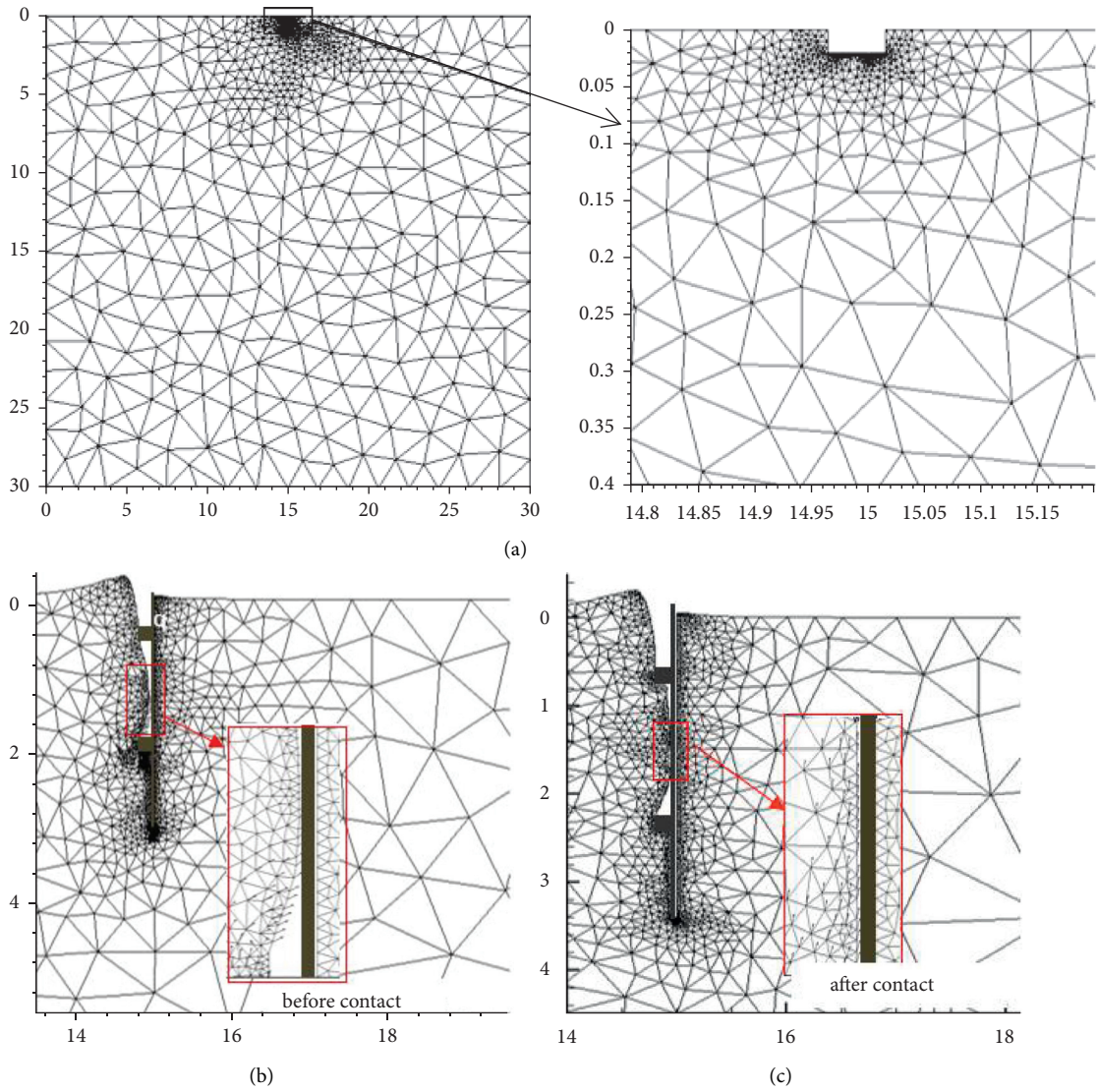


FIGURE 3: Mesh of RITSS code. (a) The initial mesh of LDFE/RITSS. (b) Dynamic mesh demonstration. (c) Established contact mesh.

TABLE 1: Summary of LDFE analyses.

Analysis	s/h	b/t	w/b	α	$S_{um}/(\gamma'(b+t))$	$(k(b+t))/S_{um}$	Notes
Group 1-A	11.0	4.0	8.33	0.2	*0.48	#0.45	Numerical model validation model
Group 1-B	2.0	2.0, 4.0	5.3, 2.7	0.03	—	—	Numerical model validation model
Group 2	10.0	3.0	6.7	0.2	4.2	0.04	Typical failure mechanism
Group 3	10.0	2.0, 3.0, 5.0	4.0, 6.7, 10.0	0.2	5.6, 4.2, 2.8	0.03, 0.04, 0.06	Effect of b
Group 4	10.0	3.0	6.7	0.1, 0.2, 0.4	4.2	0.04	Effect of α
Group 5	6.0, 10.0, 15.0	3.0	6.7	0.2	4.2	0.04	Effect of h
Group 6	6.7, 10.0, 13.3	3.0	6.7	0.2	4.2	0.04	Effect of s
Group 7	10.0	3.0	6.7	0.2	0.42, 4.2, 8.3	0.24, 0.4, 0.8	Effect of S_u

TABLE 1: Continued.

Analysis	s/h	b/t	w/b	α	$S_{um}/(\gamma'(b+t))$	$(k(b+t))/S_{um}$	Notes
Group 8	2.0, 3.0, 5.0	4.0, 6.7, 10.0		0.2	0.28, 0.42, 0.56, 1.4, 1.42, 1.76, 2.48, 2.7, 2.93, 3.53, 3.6, 4.2, 4.68, 6.25, 6.67, 7.56, 8.3, 8.61	—	Cases for preparing formula ($3 \times 3 \times 14 = 126$ cases)

* $S_{um}/\gamma'D=0.48$; * $kD/S_{um}=0.45$ (D is the caisson diameter).

strength at mudline ranging from 0.5 to 10 kPa, k is the gradient of shear strength ranging from 0.6 to 2 kPa/m, and z is the depth below mudline) is considered in this study. The lateral stress coefficient $K_0 = 1 - \sin(\phi) = 1$.

2.3. Validation of FE Model. Bucket foundation with horizontal stiffeners was studied through centrifuge test with 120 g, reported by Randolph et al. [10]. The soil profile is $S_u = 15 + 1.25z$ kPa, and the dimensional parameters of the structure are $b/t = 4$, $s/h = 11$, and $w/b = 8.33$. The project of Group 1-A in Table 1 was executed. The friction coefficient $\alpha = 0.2$ was used in the numerical model, and the normalized penetration resistance P/A_{base} is shown in Figure 4. It can be seen that both the trends and value of the resistance profile show a good agreement with those of the centrifuge test data.

A squared caisson penetrating in the homogeneous clay with aims of exploring the soil flow mechanism was conducted by a centrifuge model test (25 g), reported by Hossain et al. [5]. The test data of the centrifuge are shown in the left part of Figure 5. Group 1-B project in Table 1 was executed for the comparison, in which the related parameters of the homogeneous clay were $S_u = 12$ kPa and $\gamma' = 7.25$ kN/m³ and the geometric parameters were $s/h = 2.0$, $b/t = 2.0$ and 4.0 , $w/b = 5.3$ and 2.7 , and $\alpha = 0.3$, respectively; the results from numerical simulation are shown in the right part of Figure 5. The results from numerical simulation and centrifuge tests were in good agreement in terms of failure mechanism, soil heave, and cavities' locations and shapes. It can be found that gaps exist between stiffeners.

3. Results and Discussion

3.1. Effect of Geometric Dimensions. To identify the soil failure mechanisms of square stiffened caisson installation, a typical case was executed (Group 2 in Table 1) for the case with $S_u = 5 + 1z$ kPa. As shown in Figure 6, the inside and outside soils move upward in the initial penetration. However, with deeper penetration depth, the inside soil starts to flow rotationally and gradually fill the gap between 1st and 2nd row stiffeners. H_r is defined as critical rotational depth, above which soil cannot stand and can rotationally flow into the gaps between stiffeners, and H_c is defined as the limiting cavity depth.

3.2. Effect of Stiffener Width and Interface Friction Coefficient. To identify the influence of the stiffener width on the behavior of squared caisson penetration, cases (Group 3 in Table 1) with various stiffener widths are carried out. Figures 7(a)–7(c) show the failure mechanism of the cases with $b/t = 2.0, 3.0,$ and 5.0 . It can be found that the inside soil

heave height increases with stiffener width increasing. It indicate that, through analysis the data shown in those figures, the inside soil heave height increase the velocity of the soil move to the gap between the stiffeners.

For the cases with various roughness between structure and soil, similar findings are plotted in Figure 6(b), that proves that insignificant effect is induced by the interface friction coefficient has for the soil flow characteristic.

3.3. Effect of Stiffener Height and Stiffener Spacing. To check the influence of stiffener geometry, including spacing and stiffener height, on the soil failure mechanism, cases with various stiffener height and spacing are conducted (two groups (5 and 6) in Table 1). It can be seen that the inside soil stands vertically with piling depth $d/t = 72$ (see Figure 8(a)), and large gaps formed between soil wall sand skirt. However, with deeper penetration ($d/t = 102$, as shown in Figure 8(b)), inside soil starts to move to fill the gaps gradually. Compared with those cases with different stiffener heights and spacings, it is found that the height and spacing of stiffener have insignificant influence on the soil movement. Hence, both stiffener height and stiffener spacing have minimal effect on H_r .

3.4. Effect of Soil Strength. Figure 9 shows the soil flow patterns for the cases with various soil strengths (Group 7 in Table 1). It can be drawn that a cavity was found between 2nd and 3rd row stiffeners, which is because the soil has enough strength to prevent the soil collapsing. Hence, a cavity can exist through the installation process. It is also found that the case with stiff soil is more easy for soil to stand. A similar finding for T-bar penetrometer was reported that earlier soil backflow is induced for the case of soft soil; and on the contrary, the soil harder to flow back for the case of stiff clay [11]. Therefore, it can confirm that the soil strength has significant effect on the behavior of soil flow inside the square stiffened caisson. Compared with the results with different k , it can also be proven that soil strength gradient k has minimal influence on the behavior of soil movement.

The soil strength will affect the soil flow mechanisms; similarly, the soil disturbance will also affect soil strength around driving pile. In this paper, it is found that there existed a large soil disturbance around the caisson in the process of square stiffened caisson penetrating into normally consolidated clay (see Figure 10). The soil disturbance outside the caisson is relatively small, while the stiffeners inside the caisson cause greater disturbance to the inner soil. The disturbance will not only affect the caisson working performance but also reduce the foundation bearing capacity. Figure 9 shows a typical square stiffened caisson penetrating into the normally consolidated clay with undrained shear strength $S_u = 0.5 + 1z$ (kPa); in the

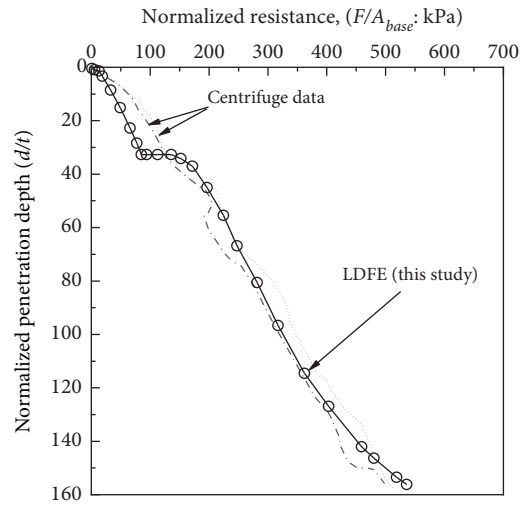


FIGURE 4: Validation in terms of resistance.

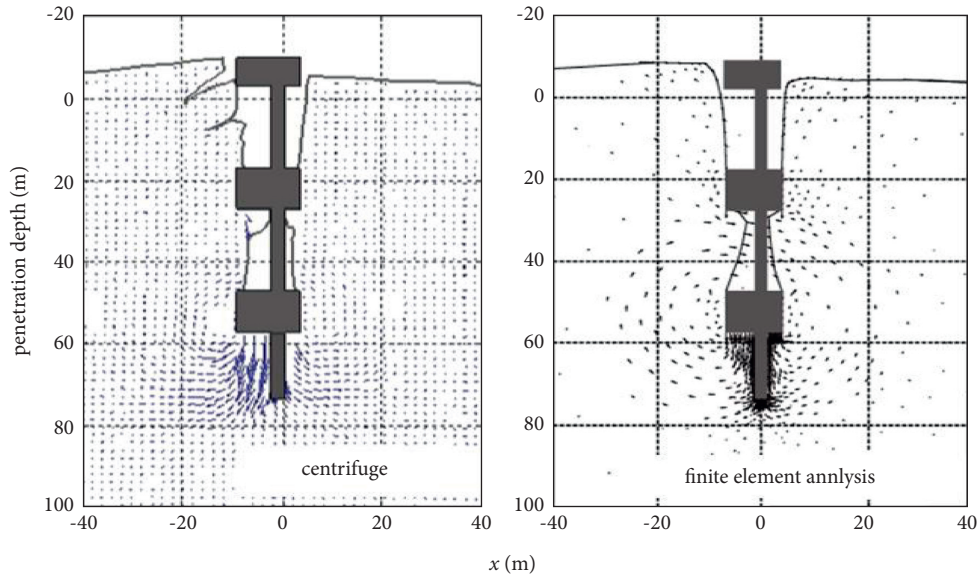


FIGURE 5: Validation in terms of soil movement.

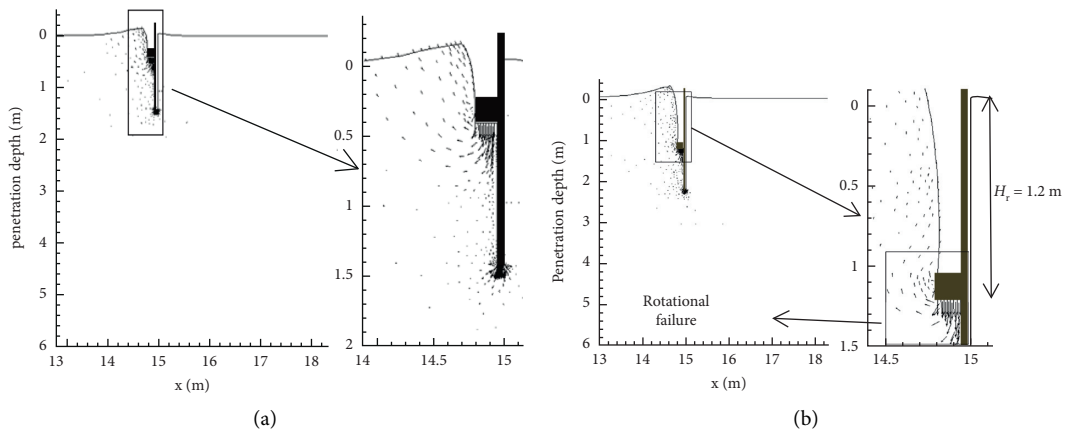


FIGURE 6: Continued.

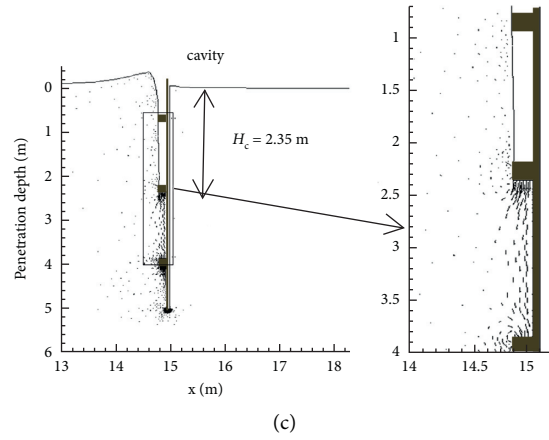


FIGURE 6: Soil movement of square stiffened caisson penetration.

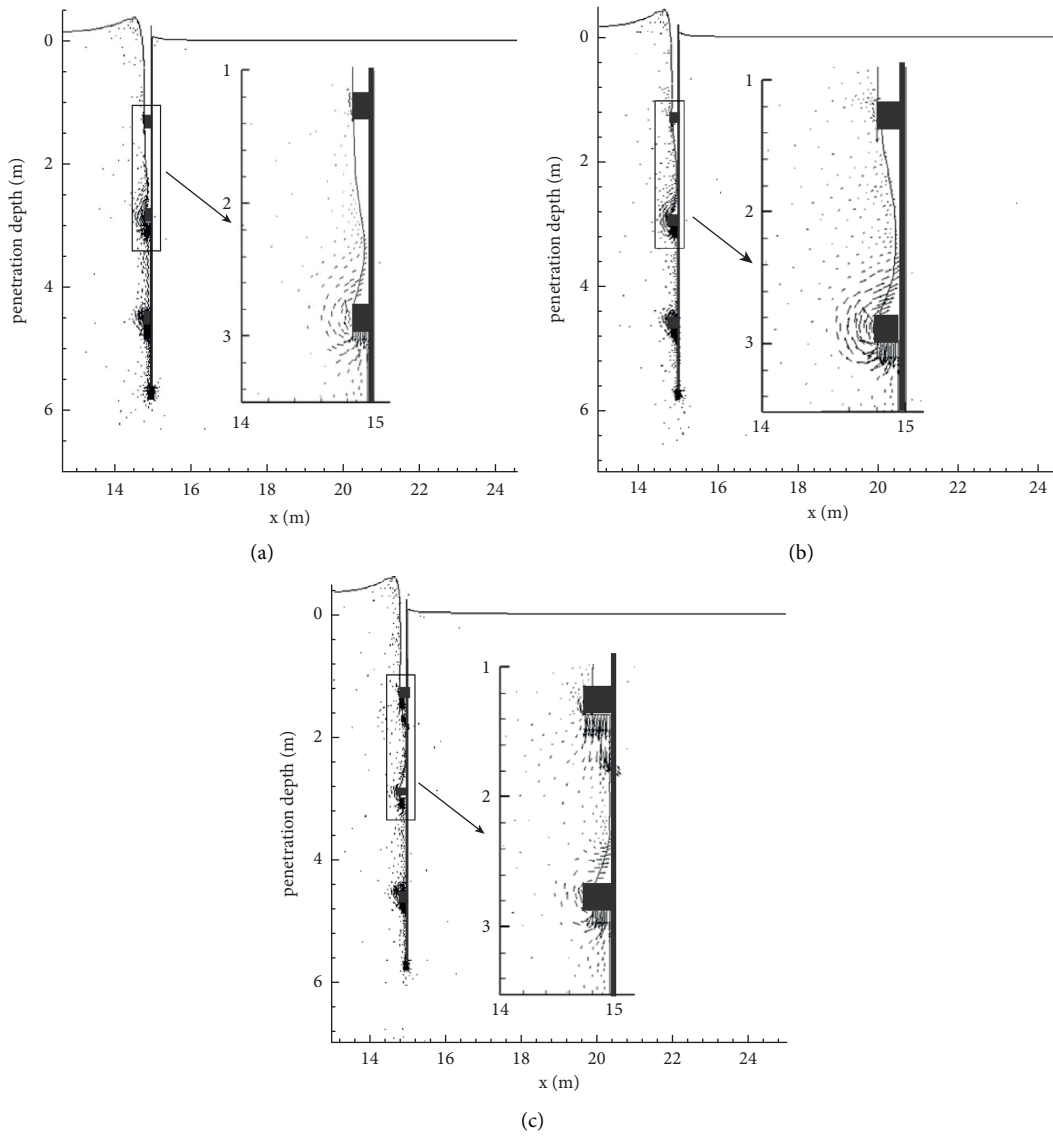


FIGURE 7: Effect of stiffener width on soil movement. (a) $b/t=2.0$. (b) $b/t=3.0$. (c) $b/t=5.0$.

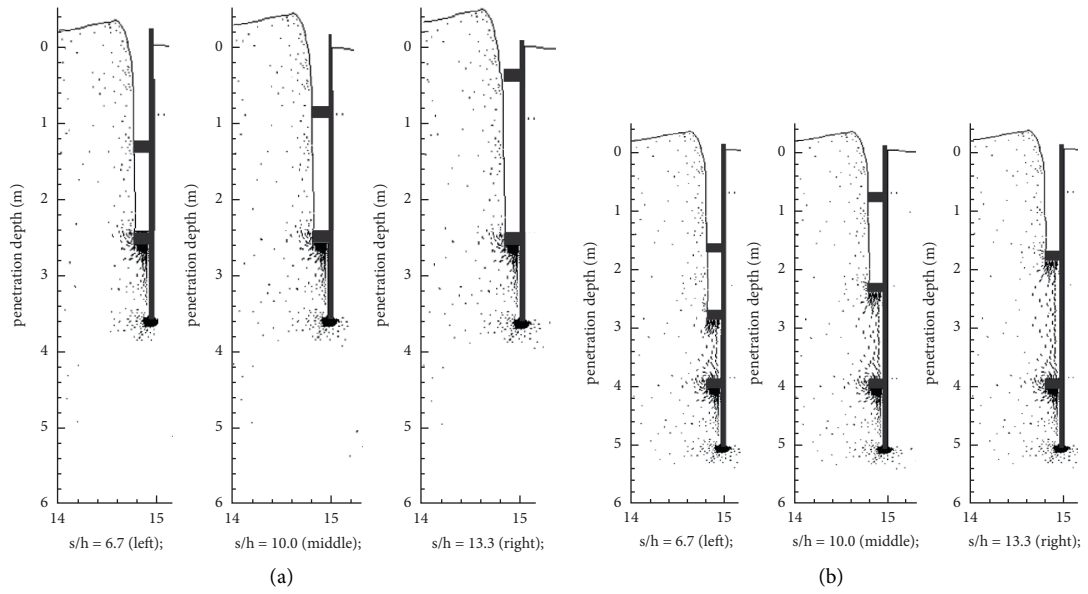


FIGURE 8: Effect of stiffener height and the distance of stiffeners on soil movement.

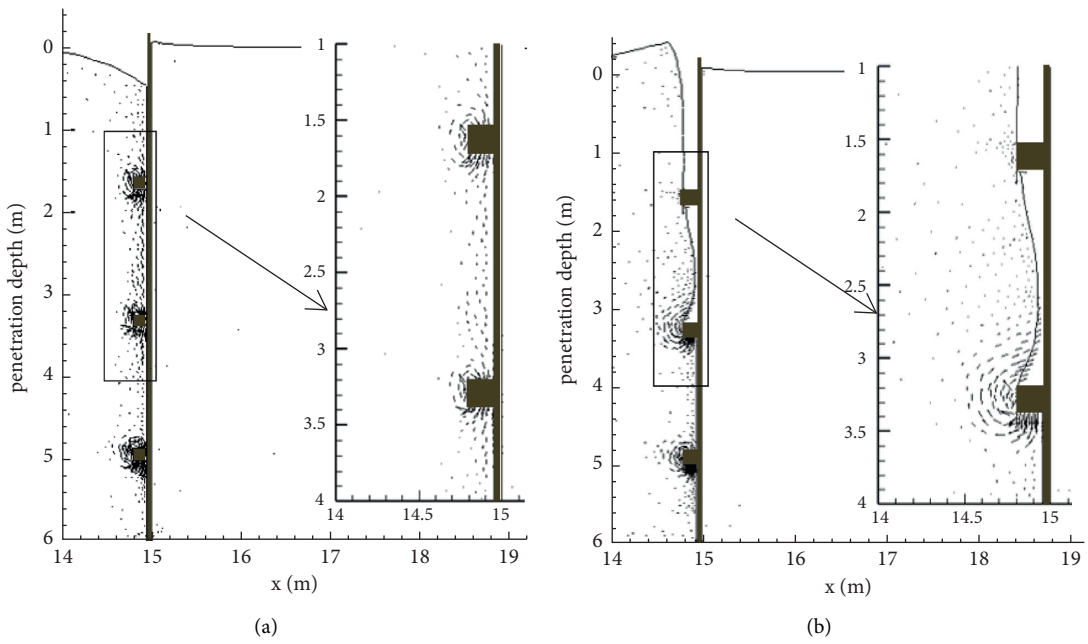


FIGURE 9: Continued.

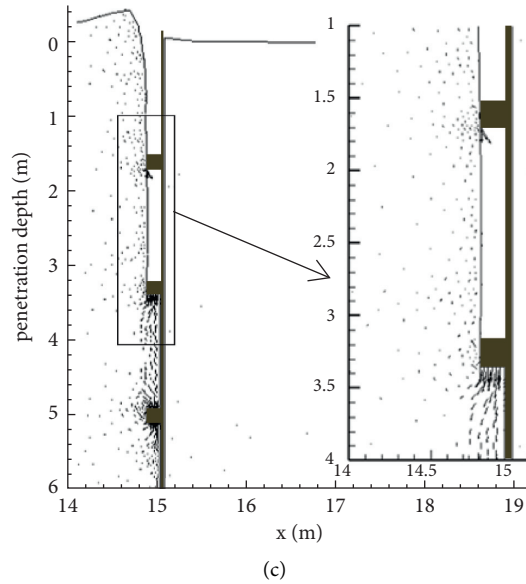


FIGURE 9: Effect of soil strength on soil movement. (a) $S_{um}/(\gamma'(b+t)) = 0.42$. (b) $S_{um}/(\gamma'(b+t)) = 4.2$. (c) $S_{um}/(\gamma'(b+t)) = 8.3$.

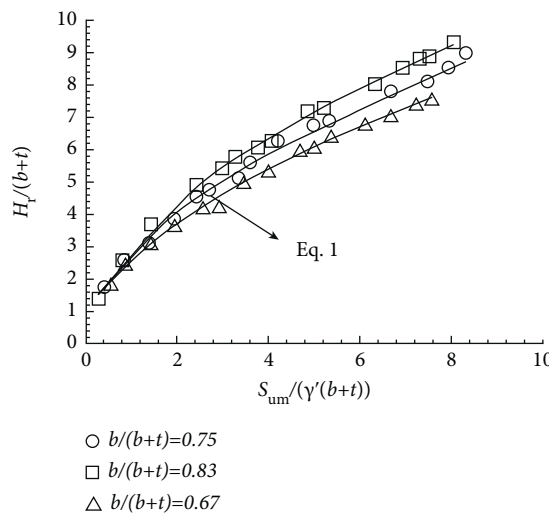


FIGURE 10: Design chart of the critical depth of rotational soil flow.

process of caisson penetration, the stiffener causes soil disturbance inside caisson, and the soft soil is trapped between the stiffeners and enters into the deeper soil layer along with the stiffeners, resulting in the lower soil strength around the caisson inner wall compared with the undisturbed soil at the same depth, which makes the internal and external friction calculations adapting the equivalent strength after the disturbance instead of the undisturbed soil strength when designing the caisson penetration resistance and subsequent bearing capacity.

4. The Critical Depth Calculation

Through the analysis of the effect of different normalized parameters on the soil flow mechanisms, the factors affecting the critical rotational flow depth H_r and the limiting cavity depth H_c include the stiffener width b and the soil undrained

shear strength (the soil surface undrained shear strength plays a main role).

To calculate and analyze a series of parameters in Group 8 in Table 1, fix $w = 1$ m, $s = 1.5$ m, $\alpha = 0.2$, $t = 0.05$ m, and $\gamma' = 6.0$ kN/m³, change S_u and b , the quantification system of the critical rotational flow depth H_r and the limiting cavity depth H_c when the stiffened caisson penetrates in the normally consolidated clay were obtained by a large number of parameter analysis, as shown in Figures 10 and 11. Hossain et al. also put forward the quantitative relationship diagram of the critical depth of spindle foundation for the investigation of spindle foundation penetrating into homogeneous clay. These studies show that the normalized critical depth increases with the increase of S_u , which is consistent with the law obtained in this paper.

According to the above calculation of different parameters, the data relevant to the critical rotational flow depth

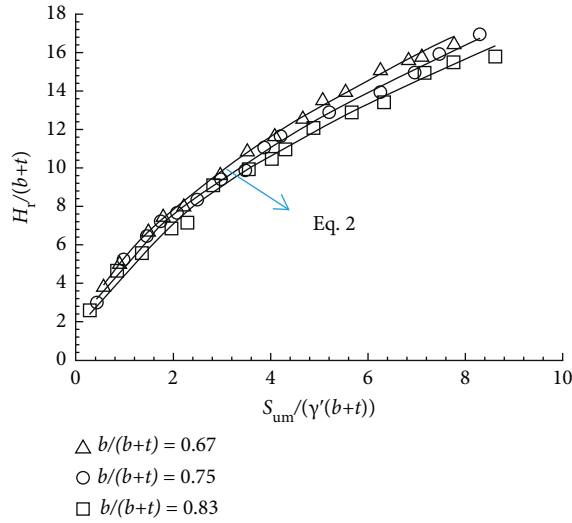


FIGURE 11: Design chart of the limiting cavity depth.

and the limiting cavity depth are obtained; from that, the following formula can be fitted ($R^2 \approx 0.98$):

$$\frac{H_r}{(b+t)} = \left(0.68 + 2.80 \frac{b}{(b+t)} \right) \left(\frac{S_{um}}{(\gamma'(b+t))} \right)^{0.54}, \quad (1)$$

$$\frac{H_c}{(b+t)} = \left(7.24 + 2.83 \frac{b}{(b+t)} \right) \left(\frac{S_{um}}{(\gamma'(b+t))} \right)^{0.56},$$

where $b+t$ usually ranges from 0.10 m to 0.35 m.

5. Concluding Remarks

Soil failure mechanisms of the squared caisson penetrating in the normally consolidated clay has been studied undertaken through the large deformation finite element analysis by using RITSS code in this study. with the aims of examining the effect of stiffeners on the behavior of failure mechanism os square stiffened caisson, and the findings can provide guidance for the design of square stiffened caisson. The following detailed conclusions were drawn:

- (1) The critical depths of rotational flow (H_r) and the limiting cavity depth (H_c) were defined. When the penetration depth of bottom stiffener reaches H_r , the soil starts to flow back into the bottom cavity, and when the soil heave height inside the caisson is higher than H_c , there exist gaps between soil and structure, and soil does not flow back, that is, when the inner soil heave height is less than H_c , the soil flows into the cavity between the stiffeners with rotational soil failure mechanisms and is trapped, moving downwards together with the stiffeners and the skirt at the same velocity, and there is no relative slide between the pile and the soil and no friction. The internal and external friction calculations need to adapt the equivalent strength after the disturbance instead of the undisturbed soil strength.

- (2) The factors affecting H_r and H_c obtained by the study and analysis of different parameters include the stiffener width b and the soil surface undrained shear strength S_{um} ; the corresponding design chart and equation of the critical depth of rotational soil flow and the limiting cavity depth were proposed; at the same time, the equation of predicting the maximum inner soil heave height was obtained. It shows that the cavity depth can be reached to ~ 5 m for the case of stiff clay, which cannot be ignored for design.
- (3) The interface coefficient α , the stiffener width h , the stiffener spacing s , and the soil undrained shear strength gradient k have minimal effect on H_r and H_c , while the soil surface strength S_{um} has the largest effect, followed by the stiffener width.
- (4) The softening and strain rate effects are not considering in this study, and it may conduct further study on it.

Data Availability

All data and FE results in the study are available from the corresponding author upon request.

Conflicts of Interest

The authors declare that there are no conflicts of interest regarding the publication of this article.

Acknowledgments

This study was supported by the Key-Area Research and Development Program of Guangdong Province (no. 2020B0101130009) and Guangdong Enterprise Key Laboratory for Urban Sensing, Monitoring and Early Warning (no. 2020B121202019). The authors also gratefully acknowledge the financial support provided by the Guangdong Basic and Applied Basic Research Foundation (2021A1515010828 and 2020A1515410001) and State Key Laboratory of Hydraulic Engineering Simulation and Safety of Tianjin University.



References

- [1] K. H. Andersen, J. D. Murff, M. F. Randolph et al., "Suction anchors for deepwater applications," in *Proceedings of the 1st International Symposium Frontiers In Offshore Geotechnics*, pp. 3–30, ISFOG, Perth, Australia, September 2005.
- [2] H. Dendani and J.-L. Colliat, "Girassol: design analysis and installation of suction anchors," in *Proceedings of the Offshore Technology Conference*, Houston, TX, USA, May 2002.
- [3] C. Erbrich and P. Hefer, "Installation of the laminaria suction piles—a case history," in *Proceedings of the Offshore Technology Conference*, Houston, TX, USA, May 2002.
- [4] H. Dendani, "Suction anchors: some critical aspects for their design and installation in clayey soils," in *Proceedings of the Offshore Technology Conference*, Article ID 15376, Houston, TX, USA, May 2003.
- [5] M. S. Hossain, B. Lehane, Y. Hu, and Y. Gao, "Soil flow mechanisms around and between stiffeners of caissons during

- installation in clay,” *Canadian Geotechnical Journal*, vol. 49, no. 4, pp. 442–459, 2012.
- [6] K. H. Andersen, P. Jeanjean, D. Luger, and H. P. Jostad, “Centrifuge tests on installation of suction anchors in soft clay,” *Ocean Engineering*, vol. 32, no. 7, pp. 845–863, 2005.
- [7] H. Zhou and M. F. Randolph, “Large deformation analysis of suction caisson installation in clay,” *Canadian Geotechnical Journal*, vol. 12, pp. 1344–1357, 2006.
- [8] W. Chen and M. F. Randolph, “External radial stress changes and axial capacity for suction caissons in soft clay,” *Géotechnique*, vol. 57, no. 6, pp. 499–511, 2007.
- [9] Z. J. Westgate, L. Tapper, B. Lehane, and C. Gaudin, “Modelling the installation of stiffened caissons in over-consolidated clay,” in *Proceedings of the 28th Int. Conf. Ocean, Offshore and Arctic Engineering*, Article ID 79125, Honolulu, HI, USA, January 2009.
- [10] M. F. Randolph, M. P. O’Neil, D. P. Stewart, and C. Erbrich, “Performance of suction anchors in fine-grained calcareous soils,” in *Proceedings of the Offshore Technology Conference*, Houston, TX, USA, May 1998.
- [11] D. J. White, C. Gaudin, and N. Boylan, “Interpretation of T-bar penetrometer tests at shallow embedment and in very soft soils,” *Canadian Geotechnical Journal*, vol. 47, no. 2, pp. 218–229, 2010.
- [12] J. P. Carter and N. P. Balaam, *AFENA Users’ Manual*, Centre for Geotechnical Research, Sydney, Australia, 1995.
- [13] M. S. Hossain, Y. Hu, M. F. Randolph, and D. J. White, “Limiting cavity depth for spudcan foundations penetrating clay,” *Géotechnique*, vol. 55, no. 9, pp. 679–690, 2005.
- [14] H. Ma, M. Zhou, Y. Hu, and M. Shazzad Hossain, “Interpretation of layer boundaries and shear strengths for soft-stiff-soft clays using CPT data: LDFE analyses,” *Journal of Geotechnical and Geoenvironmental Engineering*, vol. 142, no. 1, Article ID 04015055, 2016.
- [15] M. Zhou, M. S. Hossain, Y. Hu, and T. Zhang, “Numerical simulation of plug formation during casing installation of PCC piles,” *Canadian Geotechnical Journal*, vol. 53, no. 7, pp. 1–17, 2016.

Research Article

Optimized Design for Large Geotextile Mats over Soft Soil

Zhihuai Huang ¹, Shuaidong Yang ², Ningxin Yang,³ Mi Zhou ⁴, and Ang Li⁵

¹Key Laboratory of the Pearl River Estuary Regulation and Protection of Ministry of Water Resources, Pearl River Water Resources Research Institute, 80 Tianshou Rd., Guangzhou 510611, China

²Pearl River Water Resources Research Institute, 80 Tianshou Rd., Guangzhou 510611, China

³South China University of Technology, Guangzhou, China

⁴School of Civil and Transportation Engineering, South China University of Technology, 381 Wushan Road, Guangzhou 510640, China

⁵Reserch Fellow, State Key Laboratory of Subtropical Building Science, South China Institute of Geotechnical Engineering, South China University of Technology, 381 Wushan Rd, Guangzhou 510640, China

Correspondence should be addressed to Mi Zhou; zhoumi@scut.edu.cn

Received 5 July 2021; Accepted 6 August 2021; Published 16 August 2021

Academic Editor: Xihong Zhang

Copyright © 2021 Zhihuai Huang et al. This is an open access article distributed under the Creative Commons Attribution License, which permits unrestricted use, distribution, and reproduction in any medium, provided the original work is properly cited.

In this paper, the failure mechanisms of large geotextile mats over soft soil are carried out through finite element analyses. A finite element model is generated and validated against centrifuge testing data and previously published data of numerical simulation. Parametric study is then carried out to investigate the geotextile tension distribution and the arrangement of crashed stone. Based on the parametric study, an optimized design considering the arrangement of rock berm and a special arrangement of large geotextiles was proposed to enhance the performance of the geotextile mats. The findings of this study can provide an engineering guidance for this new technique.

1. Introduction

In the wake of increasing incidents of structure failures at rivers and coastlines, construction of cofferdams has become an important disaster mitigation strategy (see Figures 1(a) and 1(b)) [1]. With the advantages of fast construction, high global stability, and strong adaptability to the environment, geotextile structures have been applied in the construction of dikes, coastal protection, flood control, and land reclamation projects [2].

Failure mechanisms of geotextile tubes or mats over soft clay have been investigated by analytical solution, numerical modeling, and field tests. A few analytical solutions have been derived to investigate the configurations and tensile forces of the geosynthetic containers (Cantré et al. [3], Plaut [4], and Ghavanloo et al. [5]). Yan and Chu [6] carried out a preliminary design method for the geotextile mat cofferdam and assessed the stability of the dike before construction using both numerical simulation and centrifuge test. Guo et al. [7–10] proposed analytical methods to analyze the

behavior of geosynthetic mattresses resting on rigid or deformable foundation. These studies primarily focused on materials and deformations of geosynthetic tubes and mats but ignored the settlement of underlying soils. Zhu et al. [11] carried out the parametric study to evaluate the slope stability of stacked geotextiles. A series of slope stability charts were derived for rapid evaluation of the feasibility of stacked geotextiles (Figure 1(c)).

Numerical analysis was also widely employed to investigate the properties of the geotextile container. Kim et al. [12, 13] investigated the stability of geotextile tube-reinforced reclamation embankments subjected to scouring with and without additional applied ground base modifications by the finite element method (FEM). It was found that riprap protection offered the maximum improvement to the overall performance of the stability of the geotextile tube embankment system. Sun et al. [14] investigated the impact of two types of wedges on the lateral stability of geomembrane tubes with PFC 2d and provided the optimize shape and size of the wedge.

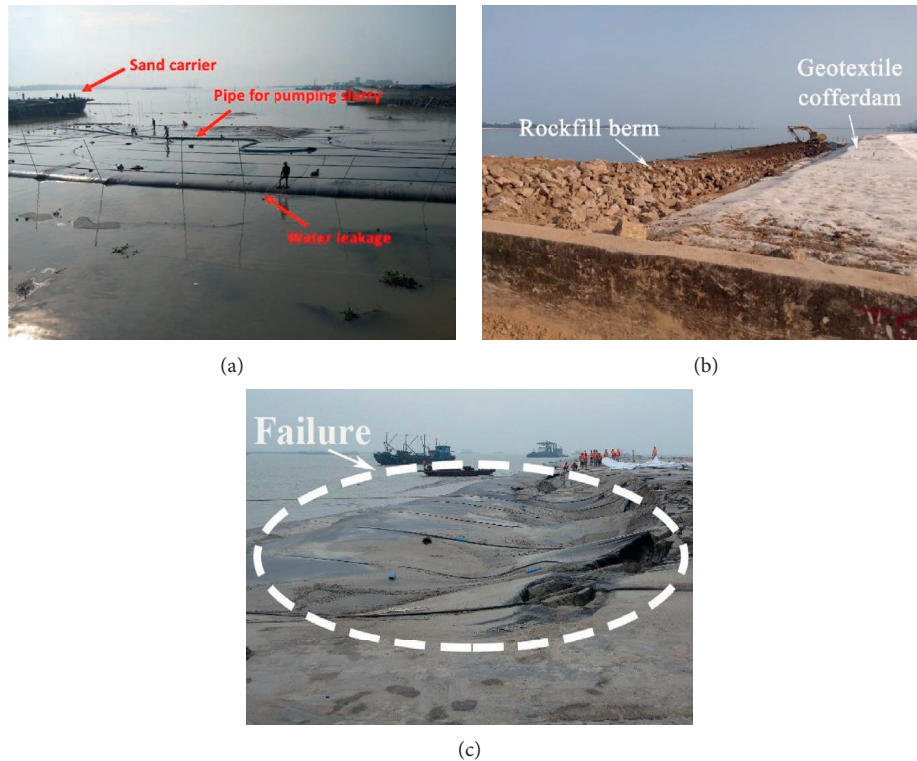


FIGURE 1: Geotextile mat dike: case of practice. (a) Geotextile mat construction. (b) Dike with rockfill berm. (c) Large geotextile mats.

Pavanello et al. [15] studied the tensile stress of stacked geological tubes under immersion conditions by the FE method and analyzed the influence of different factors on the shape and tensile stress of geotextiles. Górnjak[16] utilized the FEM-DEM method to analyze the behavior of geosynthetics when the geotextile tube in the local sinking environment was subjected to applied load and displacement. The loading capacity and the apparent stiffness of the tube were found to increase with the filling rate.

Field tests and model tests have also been carried out. To study the characteristics of failure zones of the underlying soil for flexible foundation, Zhou et al. [17] revealed the deformation form of soft soil foundation during and after the construction of cofferdam. A new failure zone was proposed by Zhou et al. Stability analysis was carried out by Peng et al. [18] on two engineering cases. It was reported that the failure of one project was the sandbags were stacked too fast leaving the soft soil underneath not able to carry out the necessary reinforcement within the timeframe. Vahedifard et al. [19] reported a research on the utilization of geo-tubes filled with stabilized dredged sediments, in which a rock revetment was placed on top of the slope to prevent future damage.

In current engineering practice, almost all geotextile cofferdams are designed with the same thickness [10]. However, due to the large upper load, the tensile stress of the bottom geotextile mat is significantly larger than that of the upper mat which is apparently over designed. It is found that the reinforcement effect of geotextiles depends not only on the performance of geotextiles but also on the number and

spacing of geotextiles [20]. A new optimized design method is proposed in this study. FE analysis is employed to investigate the geotechnical behavior of the geotextile mat cofferdams, where the effect of the crushed stone is rigorously explored. The failure mode of the cofferdam using the existing design method is analyzed, and the failure mechanism is studied.

2. Methodology

2.1. Modeling Details. In this study, the commercial software PLAXIS 2D is employed. A geotextile mat cofferdam with two berms on both sides is considered. The cofferdam and the berms sit on homogeneous soft clay. The dimension is 600 m in the horizontal direction and 150 m in the vertical direction, which eliminates the influence of boundary conditions (see Figure 2). Both the cofferdam and berms have a slope ratio of 1:2, and the widths of the cofferdam and berms are listed in Table 1. Figure 3 presents the FEM meshes used in this study, in which the underlying soil and fill material are modeled using 15-node triangular elements. In the previous studies by Kim et al. [12, 13], it is found that considering the thickness of each geo-mat and step loading of construction mesh size does not significantly influence the behavior of the dam. In this study, the mesh was generated using a fine global coarseness and locally encrypted at the cofferdam and the rockfill toes. Both the vertical and horizontal displacements are restrained at the bottom, and the horizontal displacement from the left to the right boundaries is also fixed.

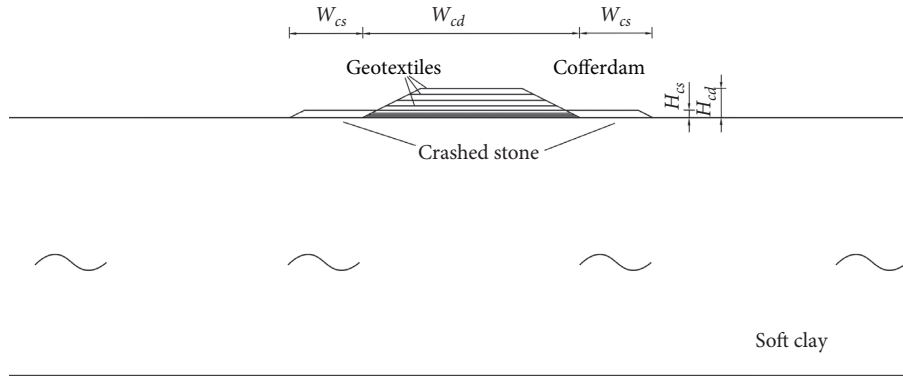


FIGURE 2: Typical embankment section.

TABLE 1: Material properties of the foundation soils, crashed stones, cofferdam fill, and geotextile.

Material	E (MPa)	ν	c_u (kPa)	ϕ ($^\circ$)	γ (kN/m ³)	k (m/day)
Soft clay	3	0.33	6	2	16.1	3×10^{-4}
Cofferdam fill	18	0.30	5	30	17.5	0.25
Crashed stone	350	0.3	0.5	38	21	9.9×10^{-10}
Geotextile	Tensile strength $EA = 140$ kN/m					

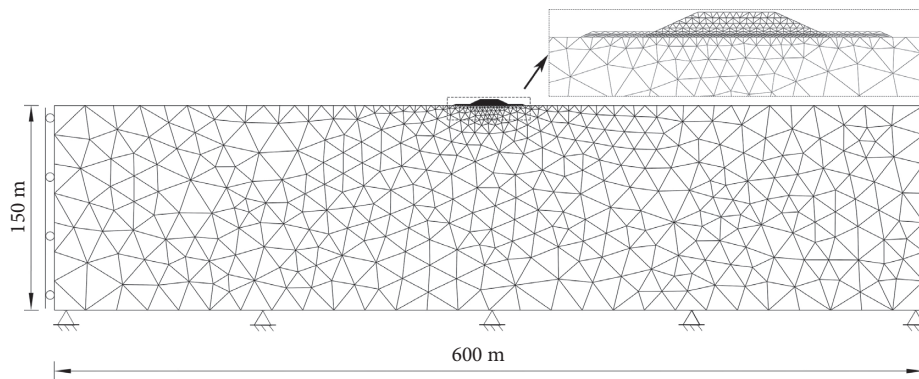


FIGURE 3: Finite element mesh in the analysis.

2.2. Constitutive Model. The linear-elastic-perfect-plastic Mohr–Coulomb model available in PLAXIS 2D is adopted with continuum elements for soil and interface elements. This model follows Hook’s law for the linear-elastic part, and the Mohr–Coulomb failure criterion is considered for the perfectly plastic region [21]. A uniform stiffness ratio of $E/S_u = 500$ is used for the clay. The stiffness ratio is within the range commonly adopted for soft clays, but the precise value has a negligible effect on the results presented. All the analyses simulated the undrained conditions. A Poisson’s ratio $\nu = 0.49$ is used, and the friction and dilation angles are $\phi = \psi = 0$.

The geotextile material is modeled using the geogrid element, which only requires elastic axial stiffness (EA) as the material property. The interaction between soil and geotextile is modeled using the interface element with an interface reduction factor (R_{int}) of 0.6 to simulate the interaction between soil and geotextile [21]. It means that the limiting shear force along the interface equals $s_u * R_{int}$. Table 1 summarizes the parameters of the numerical model. All crashed stones and soil properties are based on results from experimental tests.

2.3. Model Validation. The FE model of this study is validated against Yan and Chu (2010)’s study [6]. The thickness of the three layers of clay from top to bottom is 5 m, 10 m, and 5 m in prototype size, respectively, with corresponding undrain shear strengths are 16 kPa, 16 kPa, and 55 kPa for each layer. The modules of the filled sand are $E_s = 20$ MPa, and the frictional angle of sand is $\phi = 30^\circ$ ($W = 18$ m; $J = 140$ kN/m). Other details can be found in reference [1]. Figure 4(a) compares Yan and Chu’s results and the predicted results using the numerical modeling method of this study, from which good agreements can be found in terms of the maximum displacements of locations.

The current FE model is further validated with Yan and Chu’s centrifuge testing data. A model box of 685 mm \times 400 mm \times 200 mm was constructed to study the failure mechanism of dike on soft soils [1]. Figure 4(b) compares the displacements between the numerical prediction using the current modeling method and the centrifuge testing results, where good agreement can be found.

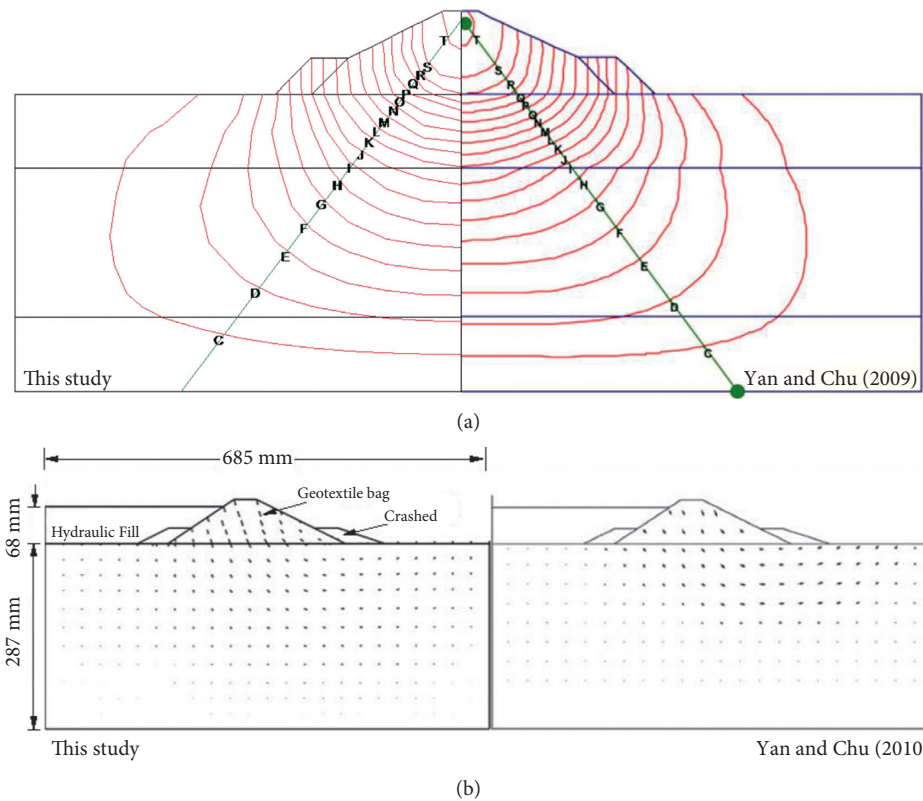


FIGURE 4: Validation of the numerical study against Yan and Chu (2009): (a) validation of settlement for numerical simulation: C~T, Disp = 0.025 m~0.450 m; (b) validation of soil flow mechanism against the centrifuge test.

The above comparisons demonstrate that the FE model of this study can capture the flow mechanisms and the potential sliding failure surface of the geotextile mat dikes over layered soils.

3. Results and Analysis

3.1. Uneven-Thicknesses Reinforcement of Cofferdams. Uneven-thicknesses reinforcement is proposed which uses an interval thickness due to continuous thickening of each layer. The first three layers of geotextile mats have a thickness of 0.2 m. The thickness then gradually increases until 1 m.

To explore the differences between uniform reinforcement and uneven-thicknesses reinforcement, a group of numerical modeling cases are simulated with cofferdam base width varying as $W_{cd} = 30, 50, 60, 80,$ and 100 m and with the homogeneous soil strength $s_u = 6$ kN/m. In these cases, the cofferdam slope is kept constant as $k = 1/2$, and the soil strength of foundation is $s_u = 6$ kPa.

The soil flow patterns are shown in Figures 5(a) and 5(b), where two different failure mechanisms can be observed. It is apparent that with the increase in the width of cofferdam, the soil failure mechanism transits from local failure to global failure, while the local failure mechanism shows up in a larger width of cofferdams with uneven-thicknesses reinforcement.

For flexible foundations, the greater the rigidity of the foundation, the greater the deformation range of the underlying soil caused by the foundation can be found. Due to

the differences in interfacial contact stresses, the settlement of the cofferdam experiences an apparent increase, which leads to the failure of the cofferdam [22]. Compared with the uniform-reinforced cofferdams, the stiffness of bottom layers of the uneven-thicknesses reinforced cofferdam increases owing to the intensive reinforcement. Then, a large plastic zone is developed [23]. This helps to explain the formation of local failure modes with a narrower width of cofferdam.

3.2. Effect of Stiffness of Geotextiles. To further explore the effect of uneven-thicknesses reinforcement on the rigidity of the cofferdam, two groups of cases are modeled by varying the geotextile tensile stiffness of the cofferdams with uneven-thicknesses reinforcement with $J = 140, 500, 1000, 2000, 4000,$ and 8000 kN/m. In these cases, the cofferdam slope is kept constant as $k = 1/2$, the soil strength of the foundation is $s_u = 6$ kPa, the cofferdam base width is $W = 80$ m, and the internal friction angle of the sand fill $\varphi = 30^\circ$.

Figure 6 depicts the variation of the limiting stack height and safety factor with the tensile strength of the geotextiles. The limiting stacked height could be effectively improved when the tensile strength of the geotextile increases. For example, the limiting stacked height of an 80 m wide cofferdam increases from 3.24 m to 3.55 m with the tensile strength of the geotextiles rising from 140 kN/m to 1000 kN/m. When the tensile strength of the geotechnical bag exceeds 1000 kN/m, the limiting stack height of the cofferdams does

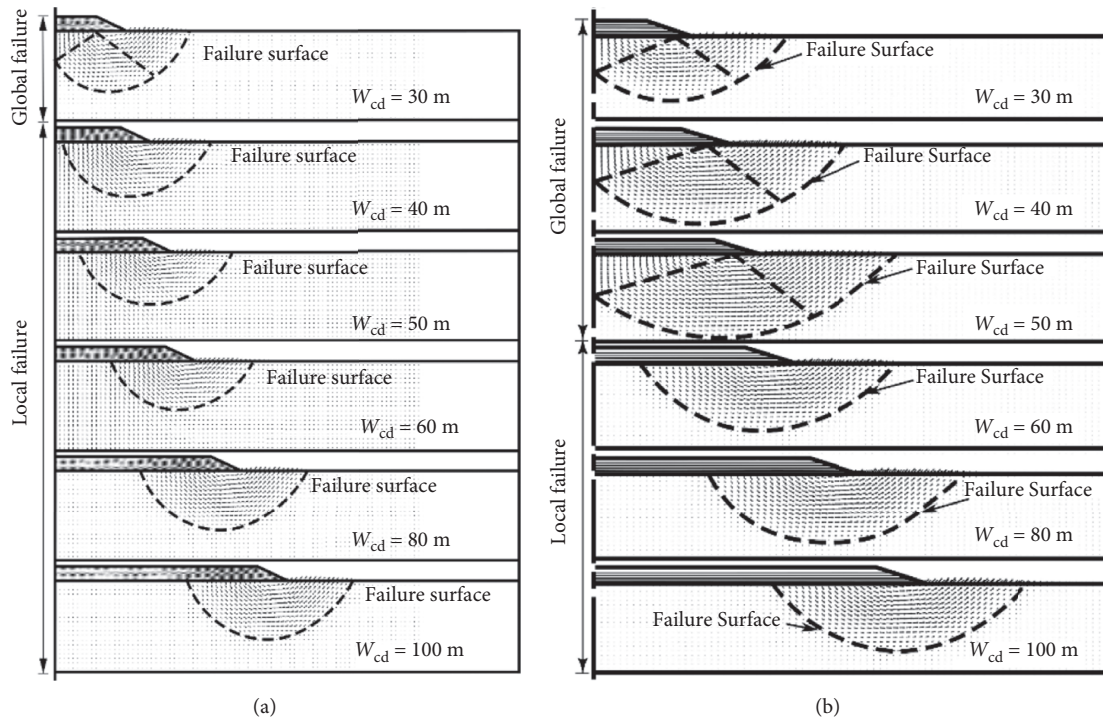


FIGURE 5: Soil heaving mechanism of different widths of large-scale sandbag cofferdams.

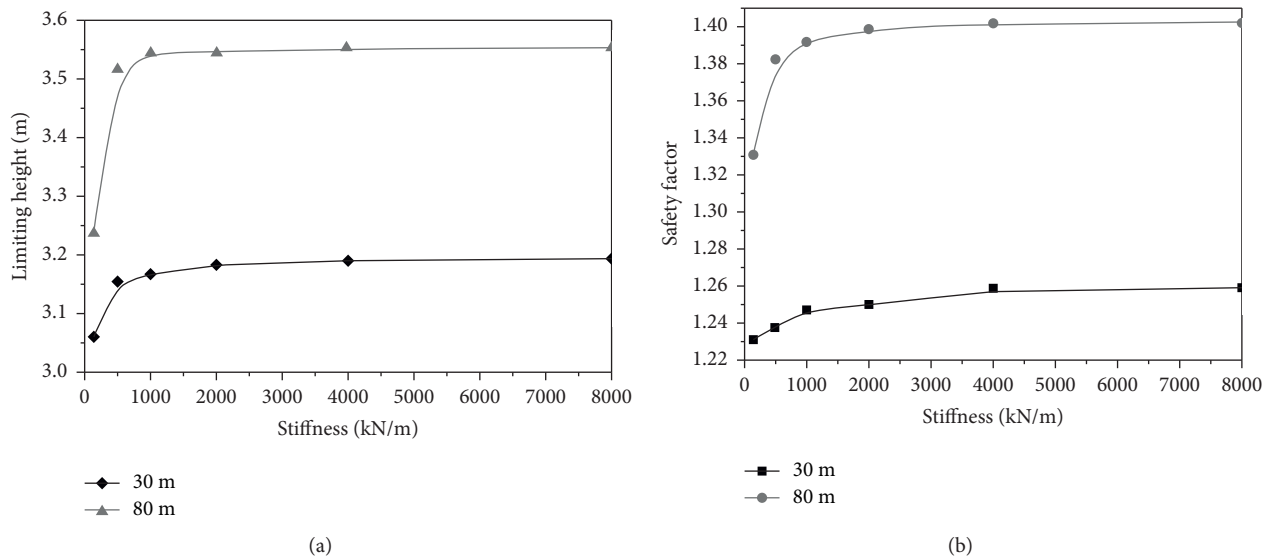


FIGURE 6: Effect of stiffness of geotextiles on limiting stack height of cofferdams.

not increase significantly. Similar phenomenon can be seen from the results of effects on the safety factor, and the only difference is that the inflection point position is different.

As the stiffness of the geotextile increases, the restraining effect on the filler is also enhanced. The increase in the tensile strength of the geotextile is beneficial to resist the vertical deformation of the cofferdam. When the load exceeds the maximum threshold of the contact surface, the shear capability of the contact surface is invalid resulting in the slippage of the fill along the surface of the geotextile. When

the load exceeds the threshold of the contact surface, the shear capacity of the contact surface will be invalid, resulting in the slippage of the fill along the surface of the geotextile. The effect of the geotextile generating the tensile force against deformation is no longer improved. Even if the tensile strength of the geotextile continues to increase, the limit of the cofferdam is not improved. Therefore, there is a threshold for the selection of the tensile strength of large sandbags rather than indefinite increase. Similar results were reported by Noorzad et al. [24].

3.3. Effect of Stabilizing Berms. As mentioned in the introduction, riprap berms are often used in the construction of large sandbag cofferdams to improve the stability of the large sandbag cofferdam and to reduce the risk of instability of the large sandbag slope [12, 19]. In order to analyze the influence of back pressure on the limit height and safety factor of cofferdams with different failure modes, a group of numerical modeling cases with varying cofferdam width $W_{cd} = 30, 50, 60, 80,$ and 100 m with and without rockfill berms are simulated. Figure 7 shows the soil failure mechanism of these two situations. From the numerical simulation, it can be found that for the cofferdams with different foundation failure modes, the limiting stack height and safety factors of the cofferdams with crashed stone are significantly improved. It is proved that the back pressure has obvious effect on the height limit and safety factor of the cofferdam.

3.4. Influence of Berm Size and Form. As can be seen from the above, the stable berm plays a significant role in balancing the cofferdam load and increasing the limiting stack height and safety factor of the cofferdam. However, the influences of berm size and form to the behavior of the cofferdam are not known, which are investigated herein.

3.5. Effect of Width of Crashed Stone. To study the influence of the berm width on the limiting stack height of the cofferdam, five cofferdam widths from 30 m to 100 m with different berm widths (0 m, 1 m, 2.5 m, 5 m, and 10 m) are modeled to analyze its influence to the limiting stack height of the cofferdam. Figures 8(a) and 8(b) illustrate the results of numerical modeling. Within a certain range, as the berm width increases, the limiting stack height and safety factor of the cofferdam increase linearly.

As shown in Figures 8(c) and 8(d), when the berm is constructed at the toe of the cofferdam, the averaged effective force under the toe of the cofferdam increases due to the downward gravity of the berm, which leads to a higher shear strain required for the foundation to yield. Under the same load, the plastic shear strain of foundation decreases, and the range of the plastic zone increases when the critical failure occurs, which makes the cofferdam more stable. Meanwhile, the wider the height of the berm, the lower the plastic shear zone under the toe is developed. This is because the mean effective stress is larger at the toe as well as the shear strain levels at which soil becomes plastic [25].

3.6. Effect of Crashed Stone Height. To illustrate the different failure modes of the soft clay with different heights of crashed stone, a group of numerical modeling cases are performed with the width of crashed stone as a constant of 10 m. The height of the berm is varied at 0.6 m, 0.8 m, 1.0 m, 1.5 m, 2 m, and 2.5 m. The safety factor of the cofferdam, the variation of the ultimate fill height, and the vector diagram of the soil displacement in typical failure modes under different width berms are shown in Figure 9.

With the increase in crashed stone height, the effect of restraining heave and preventing slip becomes more obvious until the effect reaches the optimal value. When the thickness of the berm increases further, the berm will also cause damage to the foundation soil since the berm is also a loose accumulation body built on soft soil. The final safety factor of the cofferdam is reduced. Considering the trends of the maximum height and safety factor of the cofferdam, the optimum thickness of the berm is 1 m within the scope of this study.

3.7. Distance between Cofferdam and Berms. By increasing the area of the plastic zone and limiting the movement of the soil by gravity, the berm increases the limiting stack height and safety factors of the large-scale sandbag cofferdams. Numerical simulation is performed to study the influence of the position of berm on the stability and safety of the cofferdam. Without losing generality, a berm with a thickness of 1 m and a width of 10 m is modeled. The distance between the cofferdam and the berm is gradually increasing to study the effect of the back pressure position on the performance of the cofferdam.

Figure 10 shows the effect of the distance between the cofferdam and the back pressure on the limit height and safety factor of the cofferdam; it can be seen that there is an optimal spacing (around 4 m) resulting in the maximum height and safety factor of the cofferdam. And the failure mechanisms of these cases are shown in Figure 11. It is needed to pointed that the normal method is that the case with one berm.

3.8. Combination of Rockfill Berms. As it is found above, the limiting stack height and safety factor of cofferdam are increased by the effect from the rockfill berms that can prevent the flow of soil and expand the range of plastic zone. It indicates that when the same volume of crashed stones is used to set the berms, it is more helpful to increase the stability of the cofferdam by adopting berm combinations which has a small volume and a large amount rather than only berm.

To investigate the effect of multiberms combination on the stability and safety of cofferdam, numerical analysis is carried out with varying volume ratio (inside: outside) to 4:6, 5:5, 6:4, and 7:3. Figure 12 compares the limiting stack height and the safety factor with different volume ratios. The following observations can be made: (1) as a result of preventing effect from rockfill berms, there is a threshold for the spacing of the two sections of the cofferdam; (2) the larger volume ratio (inside/outside), the stronger the preventing effect from rockfill berms between the cofferdam and the berms exists and the greater the spacing of the limiting stack height and safety factor for the cofferdam.

As illustrated in Figure 12(c) through plotting the instantaneous (resultant) velocity vectors, due to the segmentation and the interval of berms, the soil flow mechanisms are limited by the berms. If the berms closed to the cofferdam are narrower, it is apparent that the movement of the foundation soil presents two different states. The soil movement in the area

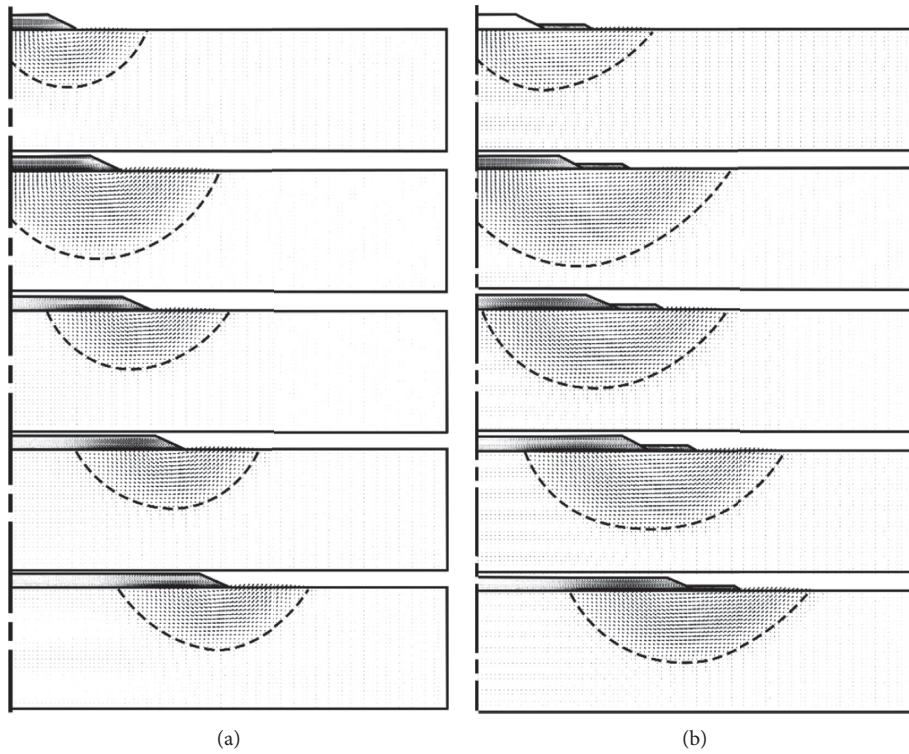


FIGURE 7: Soil heaving mechanism of large-scale sandbag cofferdams (a) without rockfill berms or (b) with rockfill berms.

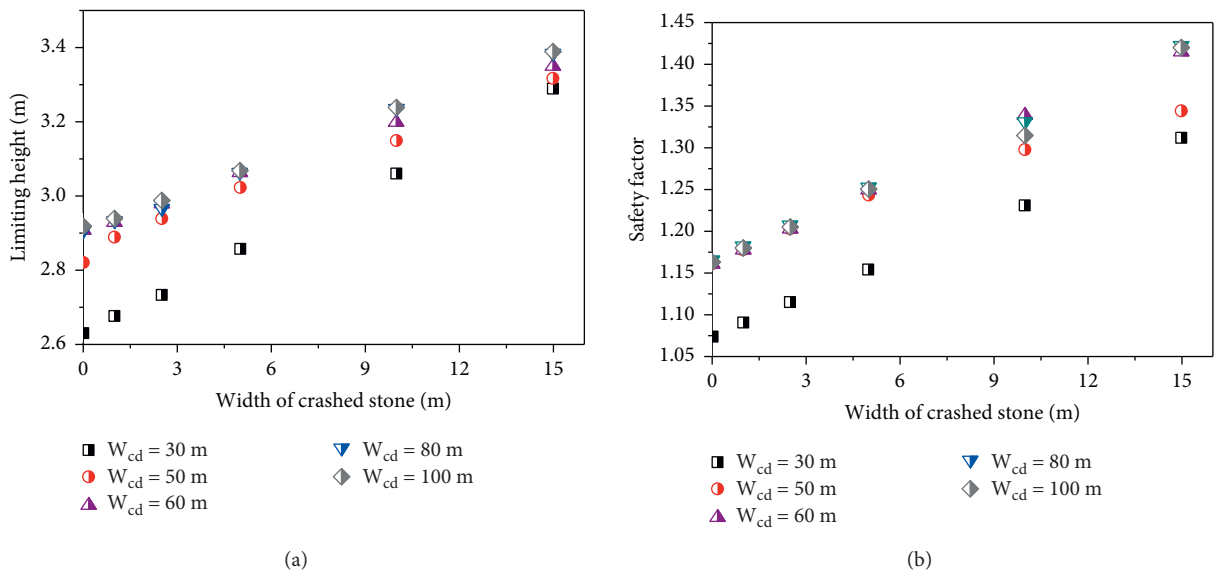


FIGURE 8: Continued.

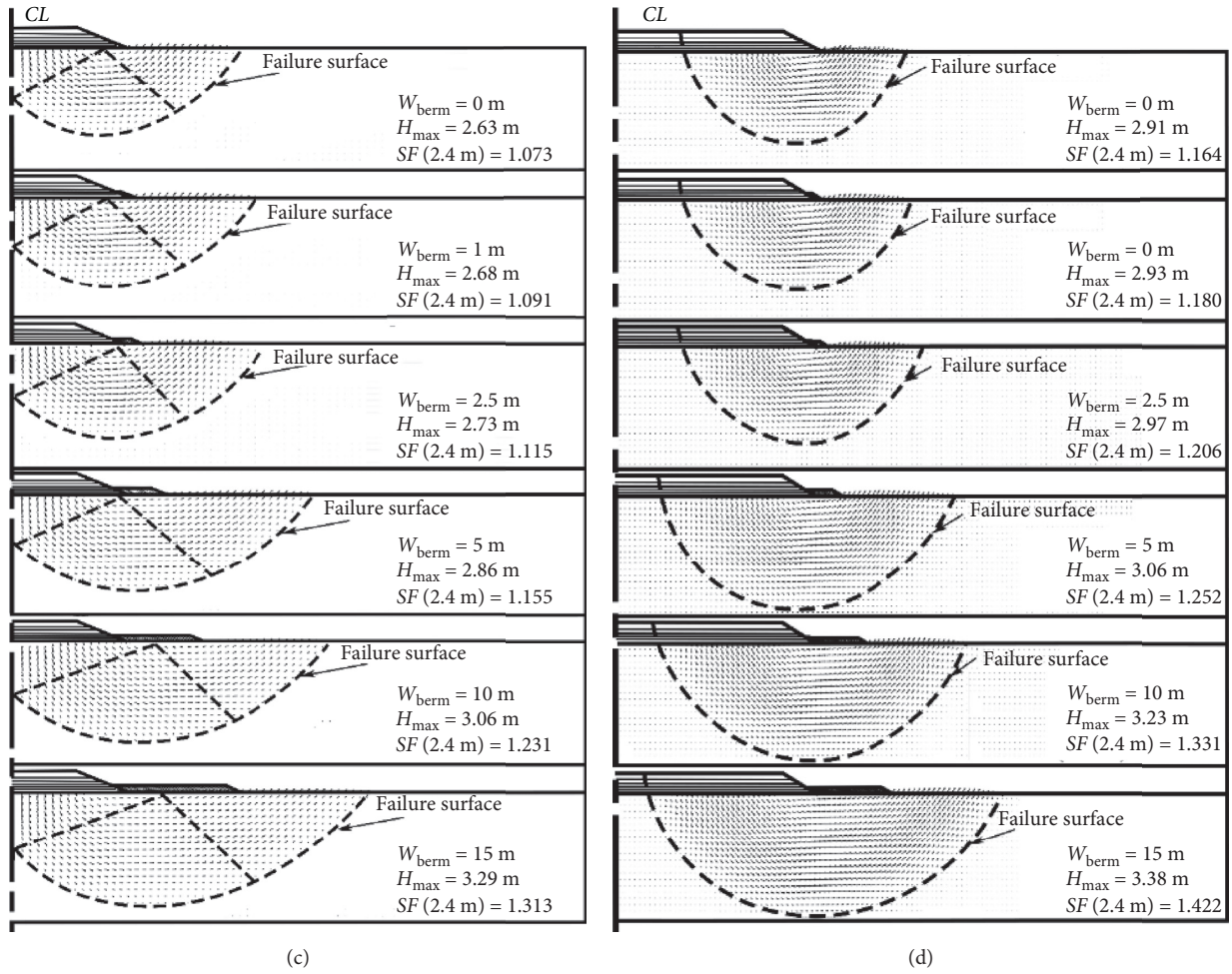


FIGURE 8: Effect of width of berms: (a) effect on limiting stack height; (b) effect on safety factor; (c) soil heaving mechanism with global failure mechanism; (d) soil heaving mechanism with local failure mechanism.

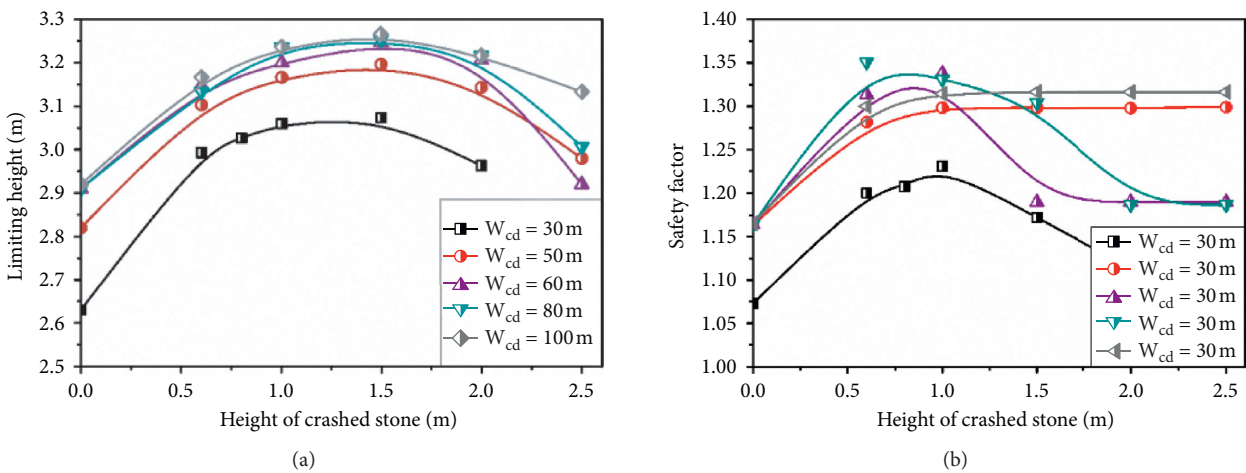


FIGURE 9: Continued.

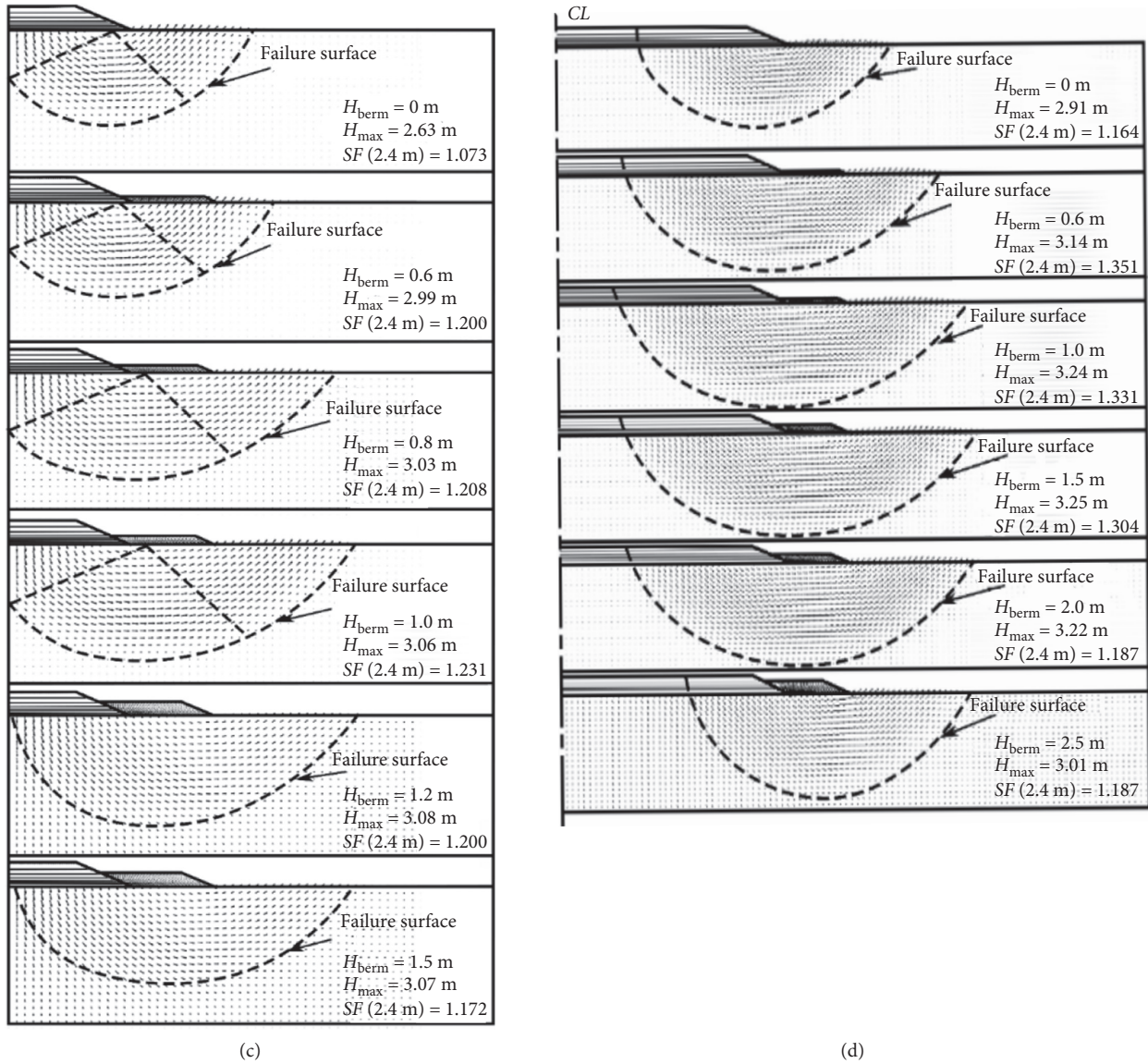


FIGURE 9: Effect of height of berms: (a) effect on limiting stack height; (b) effect on safety factor; (c) soil heaving mechanism with global failure mechanism; (d) soil heaving mechanism with local failure mechanism.

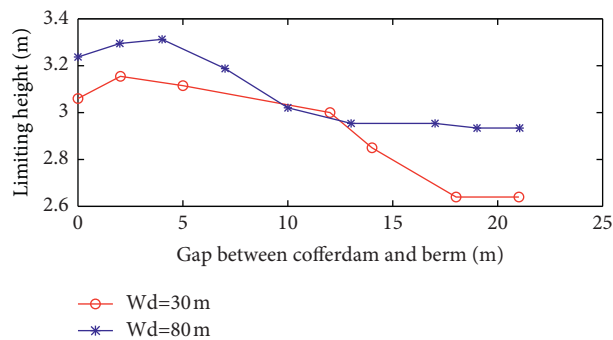


FIGURE 10: Effect of gap between cofferdam and berms on limiting stack height and safety factor of cofferdams.

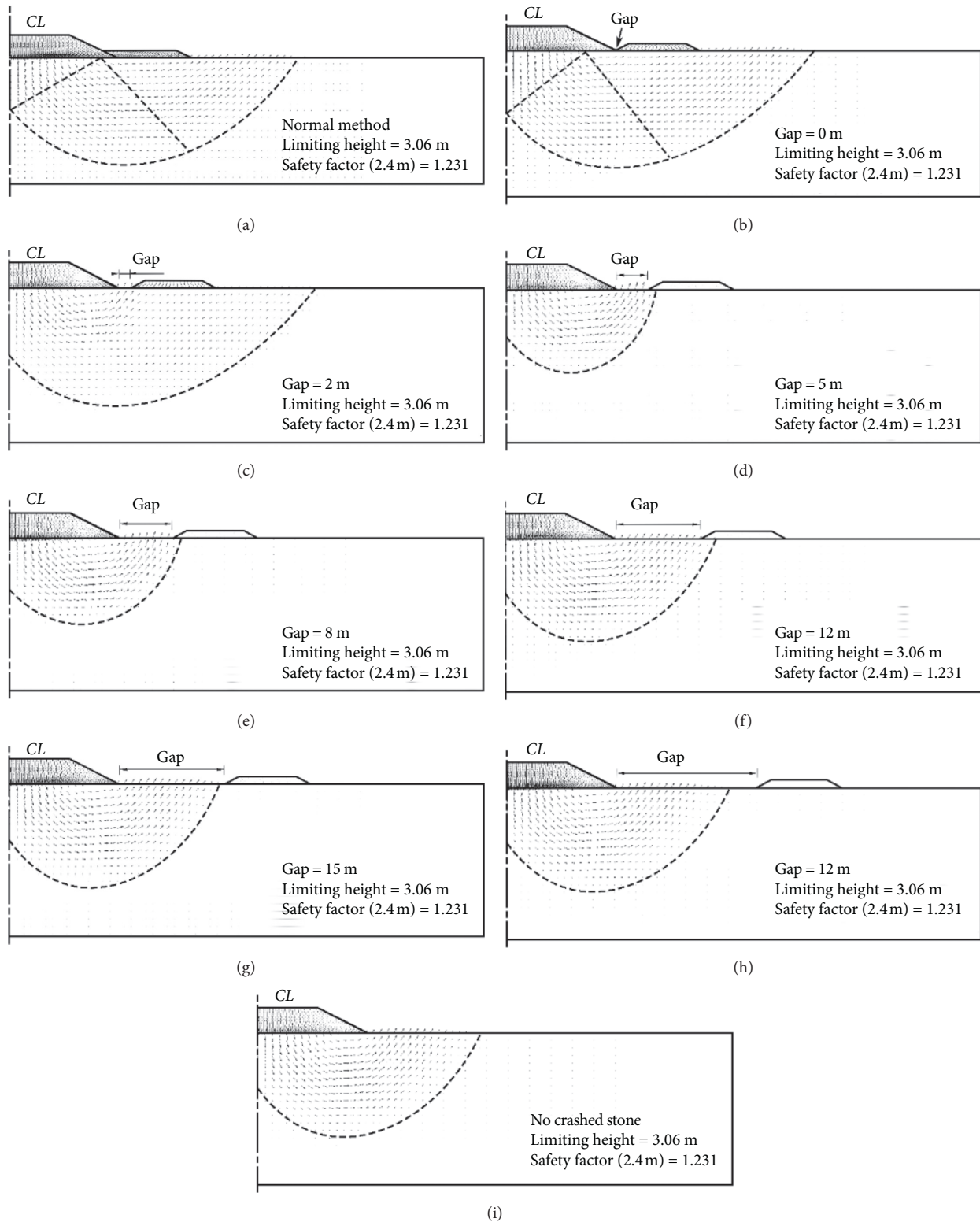


FIGURE 11: Soil heaving mechanism of large-scale soil bag cofferdams with different distances between berm and cofferdam: (a) with normal crashed stone; (b–h) with different gap; (i) with no crashed stone.

affected by the ground and the inner back pressure is obviously larger than that affected by the lateral back pressure. When the total gravel volume is constant and the inner back pressure

width is increased, the occurrence is obvious. The range of the moving soil expands and the foundation exhibits a single slip surface in the critical failure state.

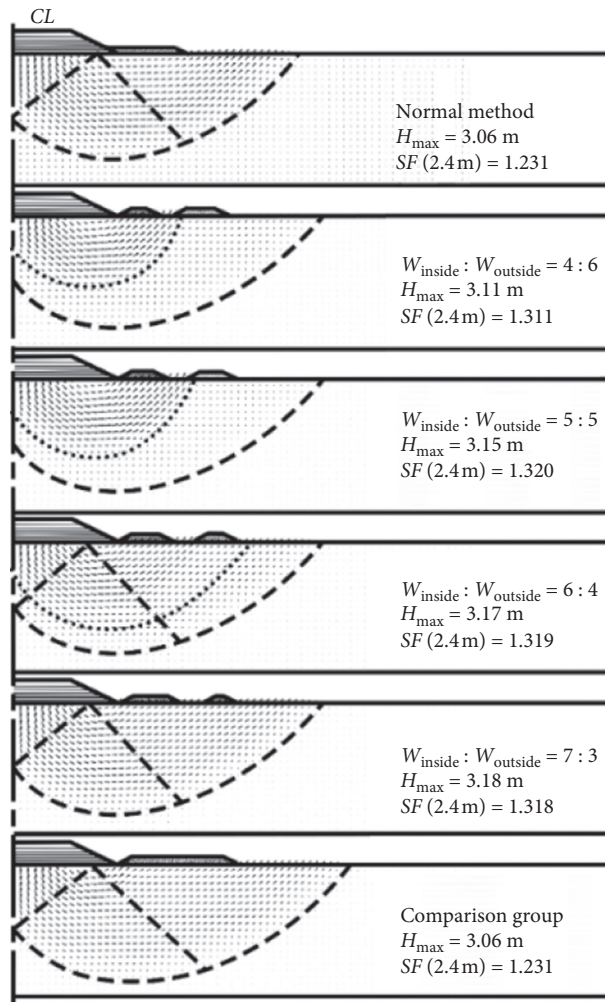
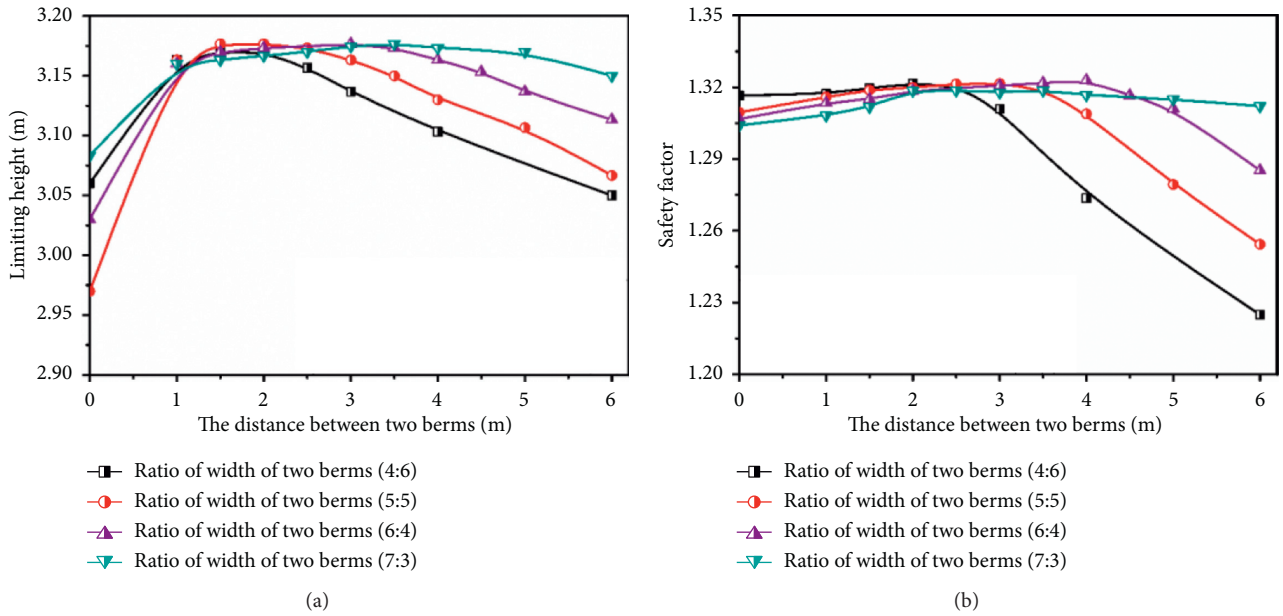


FIGURE 12: Effect of height of berms: (a) effect on limiting stack height; (b) effect on safety factor; (c) soil heaving mechanism of large-scale sandbag cofferdams with different berm combinations.

Numerical simulations are performed to compare the improvement effects of cofferdam performance parameters under different berm modes. It is apparent that the limiting stack height of the cofferdam is only 0.14 m lower than that of the nonsegmented cofferdam of the same influence width, and the safety factor of the same height (2.4 m) is only 0.061 lower. This means the material cost in berms can be saved by 1/3 with the help of the berm-combination method. The same phenomenon happens in cofferdams with local failure mode.

4. Conclusion

Numerical modeling is performed in this study to investigate the effects of geotextile mats and rockfill berm on the behavior of underlying soil and the stability of cofferdams. The following conclusions could be drawn:

- (1) The limiting stack height and safety factor of the large sandbag cofferdam are affected by the width of the cofferdam, the shear strength of the foundation, the tensile strength of geotextile, the arrangement of berms, and the additional counter pressure platform.
- (2) For large-scale geotextile cofferdams with global failure mode and local failure mode, the rockfill berms affect the limit height and safety factor of cofferdams by influencing the stress distribution in the underlying soil and limiting the uplift of foundation.
- (3) An optimized design method for large geotextile mats over soft soil is proposed to enhance the stability with the same volume of berm.

Data Availability

Some data, models, or code generated or used during the study are available from the corresponding author upon request.

Conflicts of Interest

The authors declare that they have no conflicts of interest.

Acknowledgments

This work was supported by the Open Research Fund of Key Laboratory of the Pearl River Estuary Regulation and Protection of Ministry of Water Resources ([2021] KJ01) and the Guangdong Basic and Applied Basic Research Foundation (2021A1515010828 and 2020A1515410001).

References

- [1] J. Chu, S. W. Yan, and W. Li, "Innovative methods for dike construction-an overview," *Geotextiles and Geomembranes*, vol. 30, pp. 35–42, 2012.
- [2] I. L. Howard, F. Vahedifard, J. M. Williams, and C. Timpson, "Geotextile tubes and beneficial reuse of dredged soil: applications near ports and harbours," *Proceedings of the Institution of Civil Engineers-Ground Improvement*, vol. 171, no. 4, pp. 244–257, 2018.
- [3] S. Cantré and F. Saathoff, "Design method for geotextile tubes considering strain-f," *Geotextiles and Geomembranes*, vol. 29, no. 3, pp. 201–210, 2011.
- [4] R. H. Plaut and T. C. Stephens, "Analysis of geotextile tubes containing slurry and consolidated material with frictional interface," *Geotextiles and Geomembranes*, vol. 32, pp. 38–43, 2012.
- [5] E. Ghavanloo and M. A. Maneshi, "Analysis of air-and liquid-filled heavy geomembrane tubes with internal restraint baffles," *Journal of Engineering Mechanics*, vol. 144, no. 5, Article ID 04018019, 2018.
- [6] S. W. Yan and J. Chu, "Construction of an offshore dike using slurry filled geotextile mats," *Geotextiles and Geomembranes*, vol. 28, no. 5, pp. 422–433, 2010.
- [7] W. Guo, H. Kou, B. Zhou, W. Nie, and J. Chu, "Simplified methods to analyze geosynthetic mattress resting on deformable foundation soil," *Marine Georesources & Geotechnology*, vol. 35, no. 3, pp. 339–345, 2017.
- [8] W. Guo, J. Chu, and S. Yan, "Simplified analytical solution for geosynthetic tube resting on deformable foundation soil," *Geotextiles and Geomembranes*, vol. 43, no. 5, pp. 432–439, 2015.
- [9] W. Guo and J. Chu, "Model tests and parametric studies of two-layer geomembrane tubes," *Geosynthetics International*, vol. 23, no. 4, pp. 233–246, 2015.
- [10] W. Guo, J. Chu, S. Yan, and W. Nie, "Geosynthetic mattress: analytical solution and verification," *Geotextiles and Geomembranes*, vol. 37, pp. 74–80, 2013.
- [11] M. Zhu, M. Viswanath, A. Ebrahimi, and J. F. Beech, "Slope-stability charts for stacked geotextile tubes," in *Proceedings of the Geo-Congress 2014: Geo-Characterization and Modeling for Sustainability*, pp. 3082–3091, Atlanta, Georgia, February 2014.
- [12] H.-J. Kim, M.-S. Won, and J. C. Jamin, "Finite-element analysis on the stability of geotextile tube-reinforced embankments under scouring," *International Journal of Geomechanics*, vol. 15, no. 2, Article ID 06014019, 2014.
- [13] H.-J. Kim, J. Jamin, and J. L. Mission, "Finite element analysis of ground modification techniques for improved stability of geotubes reinforced reclamation embankments subjected to scouring," in *Proceedings of the 2013 World Congress in Structural Engineering and Mechanics*, pp. 2970–2979, Korea Advanced Institute of Science and Technology Daejeon, Jeju, Republic of Korea, November 2015.
- [14] L. Sun, C. Yue, W. Guo, and Y. Ren, "Lateral stability analysis of wedged geomembrane tubes using PFC2D," *Marine Georesources & Geotechnology*, vol. 35, no. 5, pp. 730–737, 2017.
- [15] P. Pavanello, D. Tognolo, P. Carrubba, and L. Frigo, "Numerical analysis of stacked geo-tubes," in *Proceedings of the National Conference of the Researchers of Geotechnical Engineering*, pp. 225–234, Springer, Lecco, Italy, July 2019.
- [16] J. Górniak, P. Villard, and P. Delmas, "Coupled discrete and finite-element modelling of geosynthetic tubes filled with granular material," *Geosynthetics International*, vol. 23, no. 5, pp. 362–380, 2016.
- [17] X. Zhou, X. Wang, M. Wang, and I Wang, "Characteristics of failure zones of soft soil foundation under flexible load of sandbag cofferdam," *Chinese Journal of Geotechnical Engineering*, vol. 39, no. z2, pp. 45–48, 2017.
- [18] W. Peng, L. Chen, and X. Zhou, "Application of large-size sandbag cofferdam in land reclamation engineering," in

- Proceedings of the GeoShanghai 2018 International Conference: Ground Improvement and Geosynthetics*, pp. 271–278, Springer, Berlin, Germany, 2018.
- [19] F. Vahedifard, I. L. Howard, M. Bazne, B. T. Smith, and M. A. Barksdale, “Sustainably enhancing intermodal freight operation of ports using geotextile tubes,” 2015.
- [20] H. Ahmadi and M. Hajjalilue-Bonab, “Experimental and analytical investigations on bearing capacity of strip footing in reinforced sand backfills and flexible retaining wall,” *Acta Geotechnica*, vol. 7, no. 4, pp. 357–373, 2012.
- [21] R. Brinkgreve, W. Swolfs, E. Engin et al., *PLAXIS 2D 2010. User Manual*, Plaxis bv, Delft, Netherlands, 2010.
- [22] Z. K. Jahanger, S. Antony, and A. Hirani, “Foundation relative stiffness effects in sand under static loading,” in *AIP Conference Proceedings (IconMEAS 2019)* vol. 2213, AIP Publishing, 2019.
- [23] N. Yapage, D. Liyanapathirana, and C. Leo, “Failure modes for geosynthetic reinforced column supported (GRCS) embankments,” in *Proceedings of the 18th International Conf. Soil Mechanics and Geotechnical Engineering*, pp. 849–852, Paris, France, January 2013.
- [24] R. Noorzad and E. Manavirad, “Bearing capacity of two close strip footings on soft clay reinforced with geotextile,” *Arabian Journal of Geosciences*, vol. 7, no. 2, pp. 623–639, 2014.
- [25] M. Khalilzad, M. A. Gabr, and M. E. Hynes, “Assessment of remedial measures to reduce exceedance probability of performance limit states in embankment dams,” *Computers and Geotechnics*, vol. 67, pp. 213–222, 2015.